The Dissertation Committee for Hongrui Hu Certifies that this is the approved version of the following dissertation:

A Block Model for Submarine Slides involving Hydroplaning

Committee:

Stephen G. Wright, Supervisor

Robert B. Gilbert

Spyros A. Kinnas

Ronald L. Panton

John L. Tassoulas

Ellen M. Rathje

A Block Model for Submarine Slides involving Hydroplaning

by

Hongrui Hu, B.S.; M.S.

Dissertation

Presented to the Faculty of the Graduate School of
The University of Texas at Austin
in Partial Fulfillment
of the Requirements
for the Degree of

Doctor of Philosophy

The University of Texas at Austin
August 2007

Acknowledgements

I express my deepest gratitude to my advisor, Dr. Stephen G. Wright. He is one of the most talented individuals I have ever known, and he has offered me the opportunity to think independently and learn from my own mistakes. Every conversation I had with him has been a humbling and at the same time encouraging experience. Each and every comment Dr. Wright has ever given me are right to the point. I often wonder how he can develop such a comprehensive and deep understanding within seconds about the problems I have been deliberate for weeks. More impressively Dr. Wright does it with a great deal of ease and enthusiasm. I feel challenged and inspired each time I walk out of his office. Dr. Wright's strive for perfection has been the driving force for me to examine and improve my work constantly. His genuine passion for the work we do has highlighted every achievement during the research process, which has been one of the most exciting rewards for me.

I was fortunate to have Dr. John L. Tassoulas, Dr. Ronald L. Panton, Dr. Spyros A. Kinnas, Dr. Robert B. Gilbert and Dr. Ellen M. Rathje serve on my committee. Dr. Tassoulas has offered help and guidance in developing the block model. He has always been extremely patient while discussing my computer program in details. Dr. Panton has provided crucial advice on characterizing the hydrodynamic stresses applied on a slide mass by the surrounding fluid. His insight in fluid mechanics and friendly sense of

humor has shed light on the dark times when I felt lost in “the surrounding fluid”. Dr. Kinnas opened the door to computational fluid mechanics for me. I have spent hours in his office describing the frustrating failure in getting any converged results from Fluent. I thank Dr. Gilbert for asking questions that seemed simple and yet kept me thinking often deep into night. I appreciate the constant remainders Dr. Rathje has given me on maintaining the physical significance of the work I do. I have learned a lot from each of the committee members not only inside the bounds of my dissertation research, but also about the approaches to conduct research.

I also thank the other faculty members at the University of Texas, especially Dr. Olson, Dr. Stokoe and Dr. Rauch. They have welcomed my questions and always pointed to the direction where I can find an answer. There have been many fellow students who have helped me during my study at the University of Texas. I give thanks to Hua Gu, Hong Sun, Yumin Deng, Manal Salem, Christine Weber, Yin-Cheng Lin, Dr. Farn-Yuh Menq, Young Jae Choi, Kenneth Kniss, Kuo-Hsin Yang for the discussions we had about our research topics. I also want to thank Teresa Tice-Boggs and Chris Trevino for their administrative support.

Finally I want to thank my family and several dearest friends of mine. My parents and sister have always supported me and pushed me forward. I am also grateful to Dr. Don Murff for believing in me before I did myself. Without his guidance and help, my education in this foreign country would never be the same. For dearest “Auntie” Ruth Hsu, “Uncle” Phil Chang and Dr. Wenjing Duan, I am forever thankful for your care and love and there is always a special place for you in my heart.

A Block Model for Submarine Slides involving Hydroplaning

Publication No._____________

Hongrui Hu, Ph.D.
The University of Texas at Austin, 2007

Supervisor: Stephen G. Wright

This dissertation details the development of a block model for the movement of submarine slides with emphasis on possible hydroplaning. Unlike previous models, the block model simulated the mechanism of hydroplaning by monitoring the contact condition between the bottom surface of the slide mass and the underlying ground. The effect of hydroplaning on the movement of the slide mass is considered by changing the forces applied on the slide mass by the underlying ground according to the contact condition. The hydrodynamic stresses applied on the slide mass by the surrounding fluid are determined based on the numerical simulations of the flow around a sliding mass. The sliding process of the block is disretisized in a step-by-step manner using a Newmark scheme. A computer program is also written to implement the block model.

The block model is validated by comparisons between the numerical results and data reported by Mohrig, et al (1999) for laboratory experiments on subaqueous slides. An illustrative study is also conducted using the block model for the movement of the sediment slabs during the Storegga Slide. The block model has successfully predicted the occurrence of hydroplaning and run-out distances of subaqueous slides. Numerical results with the block model supports the mechanism of hydroplaning for subaqueous slides with greater run-out distances than comparable subaerial slides.

Table of Contents

List of Tables

List of Figures

Chapter 1: Introduction

Submarine landslides present an important risk to offshore structures and related facilities such as pipelines. Although submarine slides have many similarities to their subaerial counterparts, there are important differences. Hance (2002) conducted a comprehensive survey and developed an extensive database of submarine slope failures. He reported that out of 399 slides examined, 334 occurred on slopes flatter than 10 degrees. He also reported that among a total of 434 slides, 194 slides traveled a distance greater than 10 km; three slides traveled more than 500 km. The reasons for slides on such flat slopes having such large travel ("run-out") distances are only partially understood. One possible explanation for such large run-out distances is that hydroplaning occurs where the slide mass moves on a thin layer of water. The layer of water works as a lubricant between the slide mass and underlying ground and thus reduces the resistance on the base of the slide mass.

Experimental, analytical and numerical studies have been conducted to understand hydroplaning and its effect on submarine landslides. However, currently no tools incorporate the mechanism of hydroplaning and predict the process of a landslide from initiation to cessation of movement. The hydrodynamic forces on the slide mass, and the deformation and movement of a slide mass when hydroplaning occurs are not well understood or explained.

The objective of the research presented in this dissertation is to develop a numerical model for submarine slides, with emphasis on possible hydroplaning. The interaction between a sliding mass and the surrounding fluid is decoupled as two problems: 1) the flow around a sliding mass and 2) the movement of the slide mass under the hydrodynamic stresses applied by the surrounding flow.

The research conducted for this dissertation is presented in seven chapters.

1) In chapter 2, previous research on hydroplaning of subaqueous slides is summarized.
2) In chapter 3, numerical simulations and the results for the hydrodynamic conditions around a slide mass are presented. Particular emphasis is given to the stresses applied on the slide mass by the surrounding fluid before and during hydroplaning.
3) In chapter 4, the development of a block model for subaqueous slides involving possible hydroplaning is presented. The hydrodynamic stresses obtained from the research discussed in chapter 3 are integrated in the block model as stress boundary conditions.
4) In chapter 5, the block model is validated by comparison with experimental results on subaqueous slides reported by Mohrig, et al (1999).
5) In chapter 6, the block model is applied to simulate the movement of sediment slabs during the Second Storegga slide. Numerical results from the block model are compared with observations from site investigations reported by Bugge, et al. (1988).
6) In chapter 7, the conclusions of the dissertation and recommendations for future research are summarized.

Chapter 2: Background

Hydroplaning happens when a thin layer of fluid (air, water, oil, mud or other) is trapped between two objects moving relative to each other. The thin layer of fluid acts as a lubricant and reduces the friction between the two objects.

The term “hydroplaning” was first introduced to the study on submarine landslides by Mohrig, et al. (1998). They suggested hydroplaning as a mechanism to explain why submarine landslides have larger run-out distances than their subaerial counterparts even though the resistance from the surrounding water is greater than that from surrounding air.

In this chapter, the research conducted on hydroplaning in general is summarized first. Experimental, analytical and numerical studies on the hydroplaning of subaqueous slides specifically are then summarized. The limitations of this previous research are also discussed.

2.1 Previous Research on General Hydroplaning

The study and application of hydroplaning starts in the late 19th century. The term hydroplane first appeared as a name for racing boats in the 1870’s. American designer, Clinton Crane, produced one of the earliest large racing hydroplanes according to Ewart (1962). Hydroplanes obtained a high speed because of an air-cushion that formed between the bottom of the boat and the underlying water reducing the resistance on the bottom of the boat.

Harrin (1958) reported the first experimental demonstration for hydroplaning of pneumatic tires. He observed a thin layer of water between the tire surface and the pavement in a tire treadmill test. Further research on hydroplaning of pneumatic tires was conducted by the National Aeronautics and Space Administration in the 1960's. In 1983, Browne and Whicker (1983) developed a model for tire-fluid interaction during steady-state hydroplaning of a tire.

Heim (1882) first suggested that landslides traveled on a thin layer of air (at the early stage of sliding) or mud (at the later stage of sliding). Shreve (1968a, 1968b) concluded that a relatively thin layer of compressed air acted as a lubricant for the Elm and Frank landslides based on the characteristics of the slides and the reports by eyewitnesses. Moriwaki et al. (1985) conducted simple point-mass modeling for the Ontake-san avalanche and recognized that assuming entrainment of water and fluidization of the sliding avalanche boundary resulted in numerical results closest to field conditions. Finally, Mohrig, et al. (1998) pointed out that submarine landslides with long run-out distances might have involved hydroplaning.

2.2 Experimental Study on Hydroplaning of Subaqueous Slides

Laval et al. (1988), Mohrig et al. (1998, 1999) and Marr et al. (2001) have all conducted experimental studies of hydroplaning of subaqueous slides. Details from the experiments are summarized in Tables 2.1 and 2.2. Laval et al. (1988) poured sand suspensions into a channel filled with water. They observed a thin layer of water under the front of the slide mass. Mohrig et al. (1998, 1999) used slurry instead of sand suspensions. They conducted experiments both on subaqueous slides and on subaerial slides. Hydroplaning was observed in eight of ten subaqueous slide experiments. The run-out distances of subaqueous slides that hydroplaned were longer than those of subaerial slides.

Mohrig et al. proposed a densimetric Froude number, Fr_d, to characterize the onset condition of hydroplaning. The densimetric Froude number Fr_d is defined as:

$$Fr_d = \frac{U}{\sqrt{\left(\frac{\rho_s}{\rho_w} - 1\right) gH \cos\theta}} \tag{2.1}$$

where U is the average velocity of sliding, ρ_s and ρ_w are the densities of the slurry and water, g is the acceleration due to gravity, H is the average thickness of debris and θ is the slope angle of the channel bottom. Mohrig et al. reported the minimum value of the Froude number $Fr_{d,crit}$ for hydroplaning to occur was 0.3 based on their experiments. The corresponding minimum sliding velocity U_{crit} for hydroplaning to occur can thus be expressed as:

$$U_{crit} = Fr_{d,crit} \sqrt{\left(\frac{\rho_s}{\rho_w} - 1\right) gH \cos\theta} \tag{2.2}$$

Marr et al. (2001) used premixed slurry and also reported hydroplaning of the slide masses. They reported that hydroplaning resulted in depositional features such as structureless deposits, tension cracks, and compression ridges.

Table 2.1: Properties of sliding mass used in experimental studies of hydroplaning

Tests	Water content	Bulk density $(\times 10^3 kg/m^3)$	D50 (μm)	Mineralogy	Hydraulic conductivity (m/s)	Yield strength (Pa)	Viscosity (Pa-s)
Laval et al. (1988)	Solution or suspension in saline water	1.04-1.32	45-112.5	Quartz only			
Mohrig et al. (1998)	16.5% of tap water	2.08 (±0.03)	57	Quartz only	3×10^{-5}	29	14
Mohrig et al. (1999)	39% of tap water	1.6	1-3 for clay 57 for silt and sand	40% kaolin, 40% silt and 20% sand	1×10^{-4}	49 , 36 and 33	0.035, 0.023 and 0.019
Marr et al. (2001)	25%, 30% and 40% of tap water	1.56-1.93		Clay, silica sand and coal slag		9.9-50.7	

Table 2.2: Setup of experiments and observations

Tests	Equipment	Initiation	Observations
Laval et al. (1988)	Plexiglass channel (4 m long, 0.35 m deep and 0.2 m wide), slope variance from 1 º to 7 º	2l, 4l or 8l of Saline-water solutions or sand suspensions were released from the gate of the tank	A thin layer of ambient water was incorporated by gravitational instability under the overhung surge front.
Mohrig et al. (1998)	Channel (10 m long, 3 m high and 0.2 m wide) suspended in water tank with two segments, slope variance from 0º (horizontal) to 20º	Approximately 0.16 m3 of slurry (debris) was poured at the upper end of the tank in a period of 60 seconds or less.	Debris flow hydroplanes when the densimetric Froude number Fr_d is between 0.3 and 0.4. Necking happens behind the head due to the flow attenuation between the lubricated front and the more bed-attached body. The ratio of the height of head to the height of average debris body increases with Fr_d . The penetration distance of water underneath a hydroplaning debris flow increases with Fr_d and can reach 10 times the average flow depth. The debris underlain by water film ceases to flow internally and moves forward as a block. Hydroplaning also increases the frontal velocity. New head forms after the detachment of the former head.
Mohrig et al. (1999)	Channel (10 m long, 3 m high and 0.2 m wide) suspended in water tank with two segments, slopes are 6º and 1º. Two types of channel bottoms are hard bottom consisting of rough, inerodible rubber matting and soft bottom consisting deposit of an antecedent subaerial flow.	Approximately 30 l of slurry (debris) was released from the head tank through a slot (20 mm high and 170 mm wide).	Hydroplaning causes larger run-out distances on inerodible bed and mutes the role of debris rheology. It also causes head to run out ahead of the body and results in a thickness of deposit well below that associated with the yield strength. Hydroplaning suppress the remobilization of an antecedent debris deposit due to 1) thikness of an antecedent deposit well below that associated with yield strength and 2) overpassing subaqueous debris flow on a film of fluid.
Marr et al. (2001)	Glass-walled flume (10 m long and 0.3 m wide) with three segments, slope variance from 0º (horizontal) to 4.6º	91 kg premixed slurry was released from an aperture (0.3 m wide and 0.03 high)	Hydroplaning was most frequently observed in strongly coherent flows and resulted in structureless deposits, major slope-response changes in thickness, tension cracks, compression ridges, water-escape structures and detached slide-blocks.

2.3 Analytical Solution on Hydroplaning of Subaqueous Slides

Harbitz et al. (2003) developed a one-dimensional analytical solution for a slide under steady-state hydroplaning based on dynamic lubrication theory. In this section, dynamic lubrication theory is first introduced and Harbitz et al. (2003)'s solution is then discussed.

2.3.1 Dynamic lubrication theory

Dynamic lubrication theory addresses the two-dimensional flow between two infinitely long flat plates moving relative to each other as shown in Figure 2.1. The forces applied on an element of fluid by the surrounding fluid are shown in Figure 2.2. Dynamic lubrication theory involves the following assumptions:

1. The distance between the two plates h is small relative to the length of the plates L;
2. The fluid between the plates is a Newtonian liquid;
3. The kinetic pressure in the fluid p is constant in the y direction, i.e. $\frac{\partial p}{\partial y} = 0$;
4. The flow is fully developed along the x direction, i.e. $\frac{\partial u}{\partial x} = \frac{\partial v}{\partial x} = 0$, where u and v are the flow velocities in the x and y directions respectively;
5. The flow is steady, i.e. $\frac{\partial u}{\partial t} = \frac{\partial v}{\partial t} = \frac{\partial p}{\partial t} = \frac{\partial \tau}{\partial t} = 0$, where t is time and τ is the viscous shear stress in the fluid.

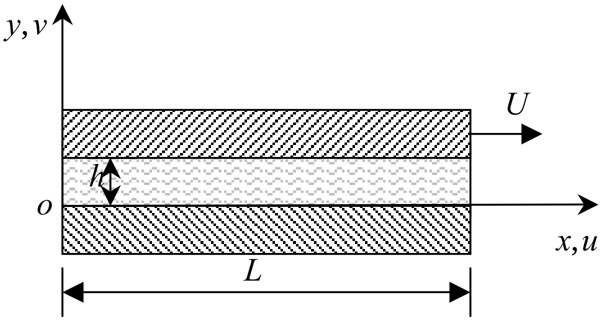

Figure 2.1: 2-D flow between plates

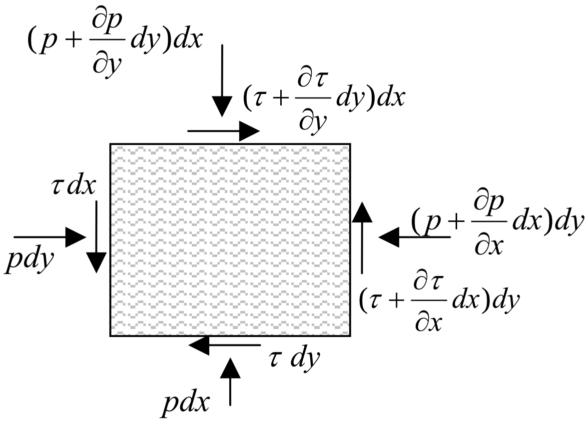

Figure 2.2: Stresses on an element of fluid

In order to determine the velocities u and v, the continuity equation of flow between the plates and the equilibrium conditions for an element of fluid are considered. The continuity equation for 2-D flow is

$$\frac{\partial u}{\partial x} + \frac{\partial v}{\partial y} = 0 \tag{2.3}$$

According to Assumption 4 above, the first term of Equation 2.3 is zero, i.e.

$$\frac{\partial u}{\partial x} = 0 \tag{2.4}$$

Thus Equation 2.3 reduces to:

$$\frac{\partial v}{\partial y} = 0 \tag{2.5}$$

Integrating Equation 2.5 with respect to y gives:

$$v = c(x,t) \tag{2.6}$$

Where $c(x,t)$ is a function of x and t. According to Assumptions 4 and 5 above, the partial derivatives of velocity, v, with respect to x and t are zero, i.e.,

$$\frac{\partial v}{\partial x} = \frac{\partial v}{\partial t} = 0 \tag{2.7}$$

Combining Equations 2.6 and 2.7 gives:

$$\frac{\partial c(x,t)}{\partial x} = \frac{\partial c(x,t)}{\partial t} = 0 \tag{2.8}$$

Equation 2.8 requires that:

$$c(x,t) = constant \tag{2.9}$$

From Equations 2.9 and 2.6, it then follows that,

$$v = constant \tag{2.10}$$

The boundary conditions for velocity v are:

$$\begin{cases} v = 0 \quad at \quad y = 0 \\ v = 0 \quad at \quad y = h \end{cases} \tag{2.11}$$

Thus, from Equations 2.11 and 2.10,

$$v = constant = 0 \tag{2.12}$$

According to Assumptions 3 and 5 above, the partial derivatives of kinetic pressure p with respect to y and t are zero, i.e.:

$$\frac{\partial p}{\partial y} = \frac{\partial p}{\partial t} = 0 \tag{2.13}$$

Equation 2.13 then suggests:

$$p = f(x) \tag{2.14}$$

where $f(x)$ is a function of x only, i.e., the kinetic pressure, p, varies only with x. The partial derivative of kinetic pressure p with respect to x is the same as the derivative of p with respect to x, i.e.:

$$\frac{\partial p}{\partial x} = \frac{dp}{dx} \tag{2.15}$$

Equilibrium of forces on the element in the x direction gives:

$$pdy - \tau dx - \left(p + \frac{\partial p}{\partial x} dx \right) dy + \left((\tau + \frac{\partial \tau}{\partial y} dy) \right) dx = 0 \tag{2.16}$$

or $$\frac{\partial p}{\partial x} - \frac{\partial \tau}{\partial y} = 0$$

Combining Equations 2.15 and 2.16 yields:

$$\frac{dp}{dx} - \frac{\partial \tau}{\partial y} = 0 \tag{2.17}$$

The relationship between shear stress τ and the rate of shear strain $\frac{\partial u}{\partial y}$ for a Newtonian fluid can be expressed as

$$\tau = \mu \frac{\partial u}{\partial y} \tag{2.18}$$

where μ is the dynamic viscosity of the fluid. Substituting (2.18) into (2.17) then gives

$$\frac{dp}{dx} - \mu \frac{\partial^2 u}{\partial y^2} = 0 \text{ or } \frac{\partial^2 u}{\partial y^2} = \frac{1}{\mu}\frac{dp}{dx} \tag{2.19}$$

Integrating Equation 2.19 twice with respect to y yields:

$$u = \frac{1}{\mu}\left[\frac{1}{2}\frac{dp}{dx}y^2 + c_1(x)y + c_2(x)\right] \tag{2.20}$$

Where $c_1(x)$ and $c_2(x)$ are functions of x governed by the boundary conditions for velocity, u. The boundary conditions for velocity, u, are as follows:

$$\begin{cases} u = 0 \quad at \quad y = 0 \\ u = U \quad at \quad y = h \end{cases} \tag{2.21}$$

Where U is the velocity of the upper plate relative to the lower plate as shown in Figure 2.1. From Equations 2.20 and 2.21 we can write:

$$\begin{cases} c_1(x) = \dfrac{\mu U}{h} - \dfrac{1}{2}\dfrac{dp}{dx}h \\ c_2(x) = 0 \end{cases} \tag{2.22}$$

Substituting Equation 2.22 into Equation 2.20 yields:

$$u = \frac{1}{2\mu}\left[\frac{dp}{dx}(y^2 - hy)\right] + \frac{U}{h}y \tag{2.23}$$

Equation 2.23 shows that the velocity u varies quadratically in the y direction.

In summary, according to dynamic lubrication theory, the velocities u and v of the fluid have the following characteristics:

1. The velocity u can be expressed as a quadratic function y;

2. The velocity v is zero.

The above characteristics of velocities u and v are applied in Harbitz et al.'s solution.

2.3.2 Harbitz et al.'s solution

Harbitz et al. (2003) solved the problem of steady-state hydroplaning of a slide mass analytically. They assumed that the slide mass is a rigid block sliding along a film of water as shown in Figure 2.3. The length-to-height ratio (L/H) of the block is assumed to be so large that the forces on the leading and trailing edges of the block are negligible. The coordinate system is considered to move with the lower left corner of the block in the x direction as shown in Figure 2.3. The interface between the block and the underlying slope is assumed to be smooth and the slope angle is constant. The distance between the bottom of the block and the underlying ground h is assumed to vary linearly along the x direction. The distances between the two lower corners of the block and underlying ground are designated as h_f and h_t, respectively. Harbitz et al. applied the conditions from dynamic lubrication theory to the flow between the block and underlying ground. They assumed that the flow velocity in the x direction u is distributed quadratically in the y direction.

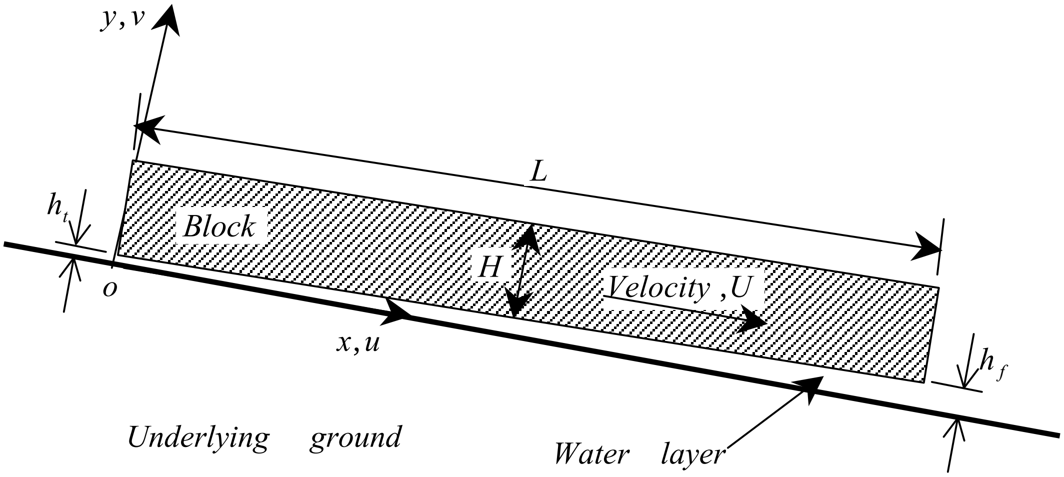

Figure 2.3: Harbitz et al.'s solution for steady-state hydroplaning of a sliding block

In Figure 2.4, the symbol Q represents the total flow rate for flow in the x direction between the block and underlying ground. Harbitz et al. (2003) derived an expression for flow rate, Q, in terms of the length of the block, L, distances h_f and h_t, and the velocity of the block, U. Harbitz et al. assumed that five types of stresses and forces are applied on the block. These stresses and forces are applied by the water and underlying ground as illustrated in Figure 2.5. Hydrostatic pressures on the block are accounted for by using the submerged weight of the block, G'. The kinetic pressure p_b and the viscous shear τ_b along the bottom of the block are functions of the flow rate Q, distances h_f and h_t, and the velocity of the block U. The kinetic pressure on the top surface of the block p_t is assumed to be zero. The viscous shear on the top surface of the block τ_t is estimated using the theory for laminar flow over a flat plate.

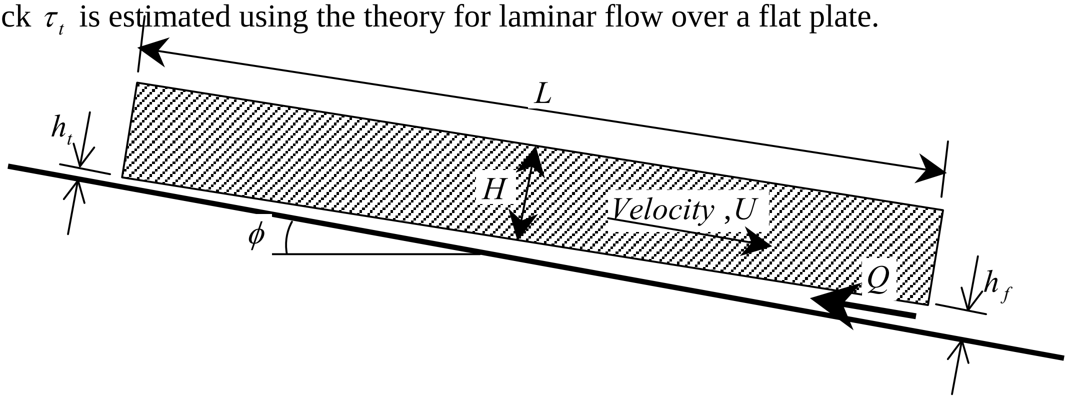

Figure 2.4: Major variables for Harbitz et al.'s solution

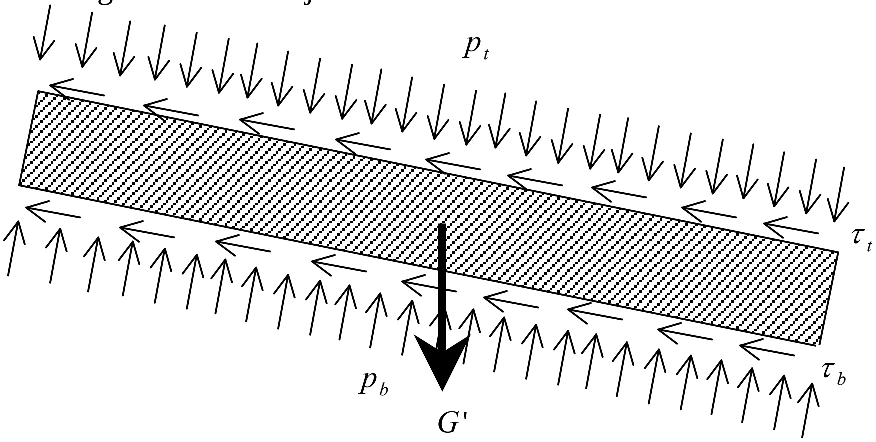

Figure 2.5: Forces and moments on the hydroplaning block in Harbitz et al.'s solution

Equilibrium of the block requires that the total forces and total moments sum to be zero. Equilibrium for the three degrees of freedom and the equation for the flow rate Q provide four simultaneous nonlinear equations as follows:

$$f_1(H, L, U, Q) = 0 \tag{2.24}$$

$$f_2(H, L, U, Q) = 0 \tag{2.25}$$

$$f_3(H, L, U, Q) = 0 \tag{2.26}$$

$$f_4(H, L, U, Q) = 0 \tag{2.27}$$

Here f_1, f_2, f_3 and f_4 are non-linear functions of L, H, U and Q. Details of functions can be found in Harbtz et al. (2003). The four equations above constitute Harbitz et al.'s analytical solution; however the actual scheme for solving the four equations together for the block length L, block height H, velocity U and flow rate Q was never provided by Harbitz et al.

2.4 Numerical Models on Post-Initiation Movement of Subaqueous Slides

De Blasio, et al. (2004) presented a one-dimensional numerical model for subaqueous slides that includes possible hydroplaning. Their model is essentially an extension of a viscous model for non-hydroplaning debris flows first developed by Imran et al. (2001). Below Imran et al's model and other models that do not include hydroplaning are discussed first. De Blasio, et al.'s model is then discussed.

2.4.1 Numerical Models involving No Hydroplaning

A common assumption for models of slide movement that do not involve hydroplaning is that the bottom surface of the slide mass is always in contact with the underlying ground. In such models detachment of the slide mass from the underlying ground or hydroplaning can not occur. Several major models of this type are summarized below.

2.4.1.1 Lumped mass models

Several models idealize the slide mass as a single point (“lumped” mass) and only provide estimates for the movement of the center of the slide mass down slope (Körner 1976; Perla et al., 1980; Hutchinson, 1986 and others). No movement of the slide mass normal to the underlying ground is considered.

2.4.1.2 Miao, et al.’s model

Miao, et al. (2001) modeled the slide mass as a set of deformable blocks. They incorporated mass dynamics into the limit equilibrium analysis of blocks considering interaction and deformation of the blocks. All the blocks are assumed to be in contact with the underlying ground along the bottom surfaces. The forces between the blocks are assumed to be parallel to the underlying slope. To calculate the deformation of the blocks, it is assumed that the blocks remain a rectangular shape. The change of length and height of the blocks are determined by the average normal stresses in the directions parallel and normal to the underlying slope respectively. The blocks are also assumed to be linearly elastic during the sliding process.

Numerical results from Miao, et al's model suggested that the cause of long run-out distance of the slide mass was the significant reduction of the shear stress between the underlying slope and the bottom surface of the slide mass.

2.4.1.3 Continuum models

Tacher, L. et al. (2005) modeled the slide mass as a continuous solid. They applied a Mohr-Coulomb model and the Hujeux elasto-plastic model in a finite element simulation of landslides. Along the interface between the slide mass and underlying ground, the displacements of the slide mass normal to the underlying ground were assumed to be zero.

2.4.1.4 Fluid models

Blight, et al. (2005), Fread (1984), Imran et al. (2001) and others modeled landslides as a viscous fluid. Imran et al. (2001)'s model is a representative example of these viscous flow models and is discussed in detail below.

In Imran et al.'s model, the deformation and movement of the slide mass are simulated as an unsteady, non-uniform, laminar slender flow as illustrated in Figure 2.6. The flow velocity in the z direction is assumed to be zero. The moving mass is assumed to remain continuous. The effect of static pressures applied on the slide mass by the surrounding fluid is accounted for by using the effective weight of the slide mass. Hydrodynamic stresses applied on the slide mass by the surrounding fluid are neglected.

Imran et al. divided the slide mass into a shear layer and plug layer. In the plug layer, the velocity u in the x direction is assumed to be constant along the y direction. Therefore the shear strain in the plug layer is zero. The shear layer is the transition between the underlying slope and the plug layer and shear strain occurs.

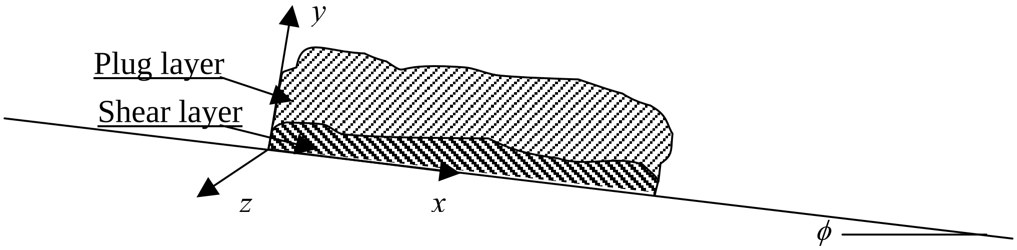

Figure 2.6: Imran et al.'s model of slides

In a coordinate system fixed on the slope as shown in Figure 2.6, the continuity equation is as follows:

$$\frac{\partial u}{\partial x}+\frac{\partial v}{\partial y}=0 \tag{2.28}$$

where u and v are the velocities in the x and y directions. The equilibrium equations in the x and y directions are as follows:

$$\frac{\partial u}{\partial t}+u\frac{\partial u}{\partial x}+v\frac{\partial u}{\partial y}=-\left(1-\frac{\rho_w}{\rho_s}\right)g\frac{\partial H}{\partial x}+\left(1-\frac{\rho_w}{\rho_s}\right)g\sin\theta+\frac{1}{\rho_s}\frac{\partial \tau}{\partial y} \tag{2.29}$$

$$p'=(\rho_s-\rho_w)g(H-y) \tag{2.30}$$

where t is time, ρ_w and ρ_s are the densities of the ambient fluid and slide mass, respectively, g is the acceleration due to gravity, H is the height of the slide mass, τ is the shear stress and p' is the pressure due to the effective weight of the slide mass. Imran et al. used the Herschel-Bulkley rheological model to describe the relationship between the rate of shear strain $\dot{\gamma}$ and the shear stress τ. The rate of shear strain $\dot{\gamma}$ can be expressed in term of shear stress τ as:

$$\frac{\dot{\gamma}}{\dot{\gamma}_r}=\begin{cases}0 & at \quad \tau\le\tau_{yield}\\ \left(\dfrac{\tau}{\tau_{yield}}-1\right)^{1/n} & at \quad \tau>\tau_{yield}\end{cases} \tag{2.31}$$

where τ_{yield} is a yield stress and $\dot{\gamma}_r$ is a reference rate of shear strain. This model reduces to a Bingham model when n is 1.0.

Imran et al. applied the following boundary conditions for the slide mass:

1. There is no slip at the interface between the slide mass and underlying ground, i.e.

$$\begin{cases} u = 0 \quad at \quad y = 0 \\ v = 0 \quad at \quad y = 0 \end{cases} \tag{2.32}$$

2. The top surface of the slide mass is a kinematic boundary, i.e.

$$v = \frac{\partial H}{\partial t} + u\frac{\partial H}{\partial x} \qquad at \quad y = H \tag{2.33}$$

For initial conditions, the slide mass is assumed to be stationary and not moving. The initial shape and dimensions of the slide mass are specified. The sliding process is arbitrarily assumed to stop when the maximum of velocity u within the slide mass is less than 10 cm/s.

Imran et al. solved Equations 2.28 to 2.30 numerically using an explicit finite difference scheme. They simulated numerically the laboratory experiments on subaerial and subaqueous slides conducted by Mohrig, et al. (1998). The numerical results from the simulations on subaerial slides agreed well with the measurements reported by Mohrig, et al. However the run-out distances of subaqueous slides predicted by Imran et al.'s model were much shorter than those reported by Mohrig, et al.

2.4.1.5 Disadvantage of models involving no hydroplaning

None of the numerical models discussed in section 2.4.1 include hydroplaning. In these models, the driving forces on subaqueous slides are considered smaller than those on the subaerial counterparts due to buoyancy. Therefore the predictions of run-out distances for subaqueous slides are smaller than those for their subaerial counterparts. These predictions are inconsistent with the observations by Mohrig, et al. (1998, 1999) discussed earlier.

2.4.2 De Blasio, et al.'s Model

De Blasio, et al. (2004) presented a one-dimensional numerical model for slides that includes possible hydroplaning. They modified Imran et al.'s model by considering the possible detachment of the slide mass from the underlying ground. The geometry and coordinate system of the model are shown in Figure 2.7.

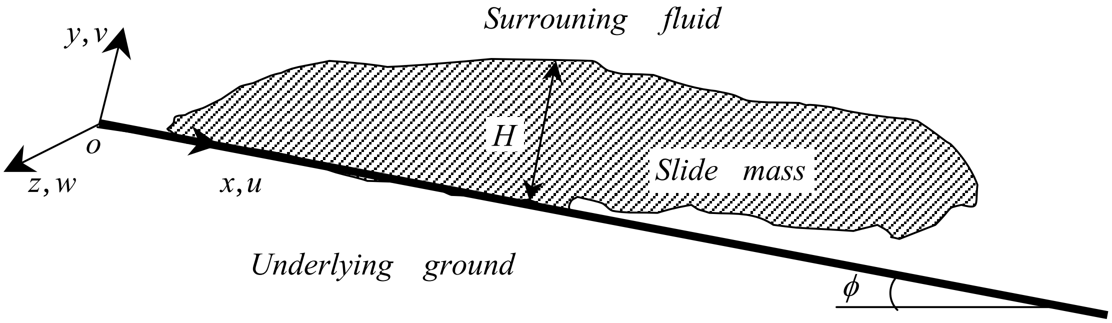

(a) Coordinate system and geometry of the slide mass

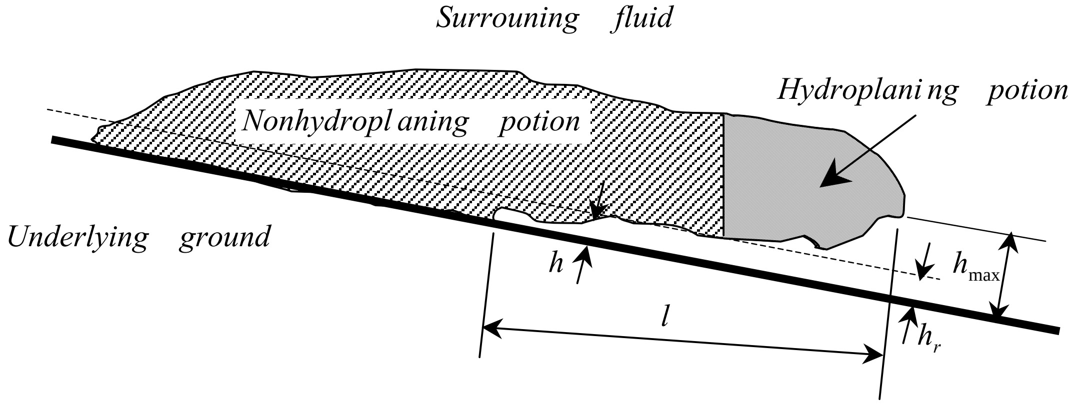

(b) Geometry of the wedge between the slide mass and underlying ground

Figure 2.7: Geometry and coordinate system for De Blasio, et al.'s model

In De Blasio et al.'s model, the slide mass is assumed to be a viscous fluid and the sliding process is divided into four stages. The four stages of sliding are as follows: (1) the slide mass flows directly on the surface of the underlying ground, (2) a wedge of water forms at the interface between the slide mass and underlying ground, but the wedge is not thick enough for the slide mass to hydroplane, (3) the slide mass hydroplanes and (4) hydroplaning stops and the slide mass decelerates. For stages (1), (2) and (4), the viscous shear on the top surface is assumed to be due only to hydrodynamic stresses applied on the top surface of the slide mass. Viscous shear is estimated using the coefficient of viscous drag derived for cylinders by Newman (1977). Along the bottom surface of the slide mass, shear stress is assumed to be applied by the underlying ground. For the first stage, the shear stress on the bottom surface of the slide mass is related to the yield stress of the sliding mass. The second stage starts when the velocity of the slide mass reaches a "critical" value. The critical velocity U_{crit} is determined using Equation (2.2) and the critical Froude number $Fr_{d,crit}$ is assumed to be 1.0. For the second stage, a wedge of water is introduced suddenly at the interface between the slide mass and the underlying ground near the front of the slide mass. As shown in Figure 2.7 (b), the thickness of the wedge h is a function of the coordinate x. Initial values of thickness h and length l of the wedge are assumed arbitrarily. Within the wedge of water, the kinetic pressure p is assumed to vary linearly along the x direction. The velocity u of water within the wedge in the x direction is assumed to vary quadratically in the y direction as discussed earlier in section 2.3.1. The flow of water within the wedge is solved for together with the flow of the sliding material. The changes of the wedge's dimension (h and l) are also computed. The shear stress on the bottom surface of the slide mass is assumed to be applied by the underlying ground despite the existence of the wedge of water. Any influence on the shear stress produced by the wedge of water is neglected.

The third stage starts when the maximum value of thickness $h_{\max}$ is greater than the height of roughness h_r at the interface between the slide mass and the underlying slope. The height of the roughness h_r is assumed to be several millimeters for laboratory tests and several decimeters for cases in the field. In the third stage, the portion of slide mass under which the thickness h of the wedge of water is greater than height h_r is assumed to hydroplane. The shear stress on the bottom of the hydroplaning portion of the slide mass is assumed to be the viscous shear at the top surface of the water wedge. A drag due to kinetic pressure p applied by the surrounding fluid is added on the slide mass. This drag is estimated using the coefficient of pressure-induced drag derived for cylinders by Newman (1977). The fourth stage of sliding is assumed to start when the maximum thickness $h_{\max}$ is smaller than the height of roughness h_r. The fourth stage is similar to the second stage and the slide mass decelerates until it stops.

2.5 Examination of Previous Research on Hydroplaning of Slides

In this section, the previous experimental, analytical and numerical research on hydroplaning of subaqueous slides is examined and limitations are discussed.

2.5.1 Examination of Harbitz et al.'s solution

In order to examine Harbitz et al.'s solution, a numerical method was used to solve Equations 2.24 to 2.27 for the block length L, block height H, velocity U and flow rate Q. A computer program nopressure.cpp was written in the C programming language to implement the numerical method. Details of the program, input and output files of the program are included in Appedix A. The numerical method and results are discussed further below.

2.5.1.1 Numerical method

A Newtonian iterative procedure was used to solve Harbitz et al.'s Equations 2.24 to 2.27. For each iteration the increments of unknowns (L, H, U and Q) are calculated as follows:

$$\begin{bmatrix} dL \\ dH \\ dU \\ dQ \end{bmatrix} = A^{-1} \begin{bmatrix} f_1 \\ f_2 \\ f_3 \\ f_4 \end{bmatrix} \tag{2.34}$$

where dL, dH, dU and dQ are the increments of unknowns L, H, U and Q respectively, f_1, f_2, f_3, and f_4 are the same functions as in Equations 2.24 to 2.27, A is a matrix defined as:

$$A_{i,1} = \frac{f_i(L+dL) - f_i(L-dL)}{2dL} \qquad for \quad i=1 \ \ to \ \ 4 \tag{2.35}$$

$$A_{i,2} = \frac{f_i(H+dH) - f_i(H-dH)}{2dH} \qquad for \quad i=1 \ \ to \ \ 4 \tag{2.36}$$

$$A_{i,3} = \frac{f_i(U+dU) - f_i(U-dU)}{2dU} \qquad for \quad i=1 \ \ to \ \ 4 \tag{2.37}$$

$$A_{i,4} = \frac{f_i(Q+dQ) - f_i(Q-dQ)}{2dQ} \qquad for \quad i=1 \ \ to \ \ 4 \tag{2.38}$$

where $A_{i,1}$ to $A_{i,4}$ are the four terms at the ith row of matrix A. The numerical error for the $(i+1)th$ iteration is defined as:

$$error_{i+1} = \max\left(\left| \frac{L_{i+1} - L_i}{L_i} \right|, \left| \frac{H_{i+1} - H_i}{H_i} \right|, \left| \frac{U_{i+1} - U_i}{U_i} \right|, \left| \frac{Q_{i+1} - Q_i}{Q_i} \right| \right) \tag{2.39}$$

Where L_i, H_i, U_i and Q_i are the variables calculated in the ith iteration and L_{i+1}, H_{i+1}, U_{i+1} and Q_{i+1} are the variables calculated in the $(i+1)th$ iteration. More details on the Newtonian procedure can be found in Ansorge, et al. (1982).

2.5.1.2 Numerical results

Twenty-two cases were analyzed using the computer program for slope angles of the underlying ground ϕ ranging from 0.01 to 10 degrees. The input conditions for the numerical cases are listed in Table 2.3. The tolerance for the numerical error defined by Equation 2.39 was specified as 10^{-3}. Calculated values for the unknowns (L, H, U and Q) are plotted versus the slope angle of the underlying ground ϕ in Figures 2.8 to 2.11. Considerable scatter was observed in the computed values, possibly as a result of the error tolerance being too large. However attempts to reduce the apparent scattering by reducing the error tolerance were generally unsuccessful and the iterations were eventually terminated before convergence was achieved.

Table 2.3: Input conditions for numerical cases

Case No.	$\upsilon_w \quad (m^2/s)$	r	k	ϕ (degree)	R_s	s
1	1.00E-06	4	5.00E-05	0.01	0.8	1.0
2				0.03		
3				0.07		
4				0.10		
5				0.20		
6				0.30		
7				0.40		
8				0.50		
9				0.60		
10				0.70		
11				0.80		
12				0.90		
13				1.00		
14				2.00		
15				3.00		
16				4.00		
17				5.00		
18				6.00		
19				7.00		
20				8.00		
21				9.00		
22				10.00		

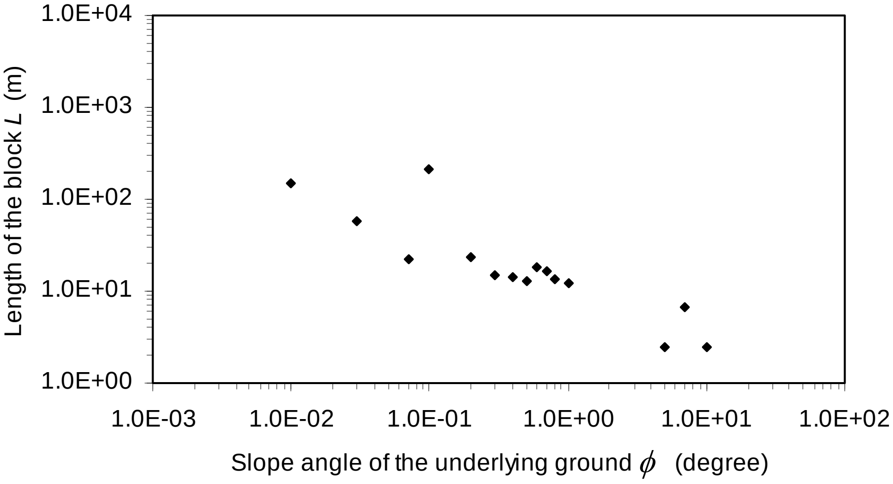

Figure 2.8: Calculated length of the block using Harbitz et al.'s solution

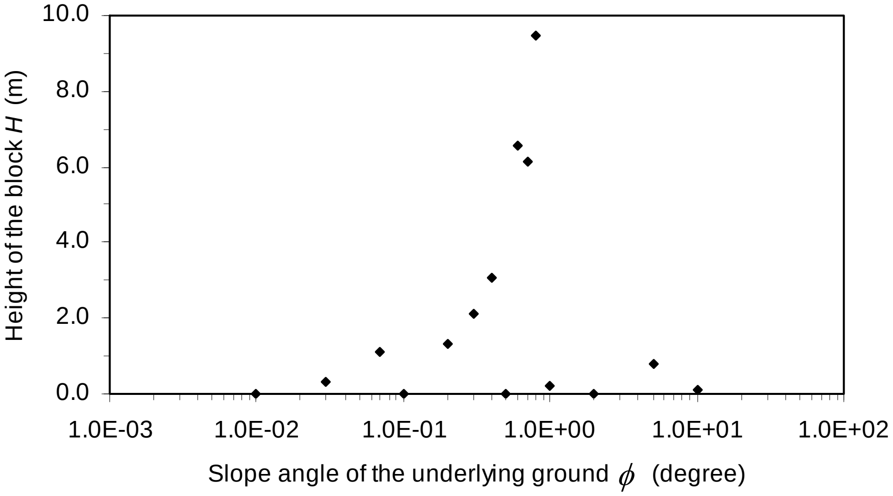

Figure 2.9: Calculated height of the block using Harbitz et al.'s solution

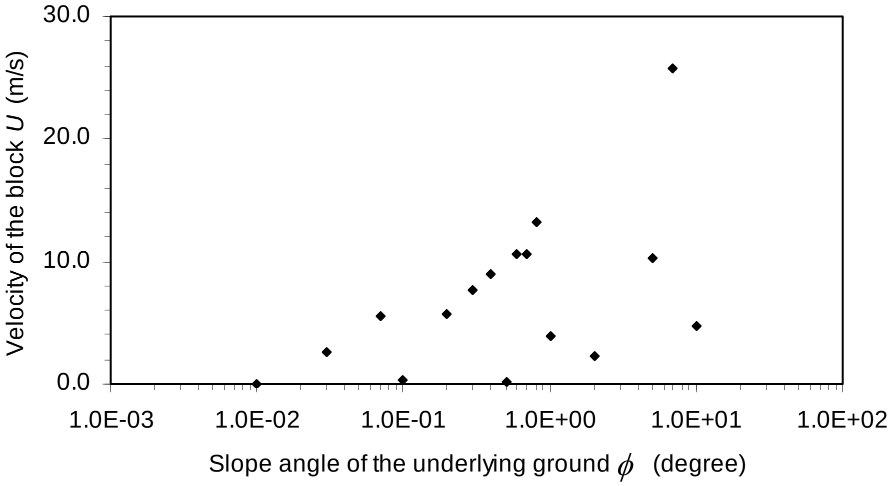

Figure 2.10: Calculated velocity of the block using Harbitz et al.'s solution

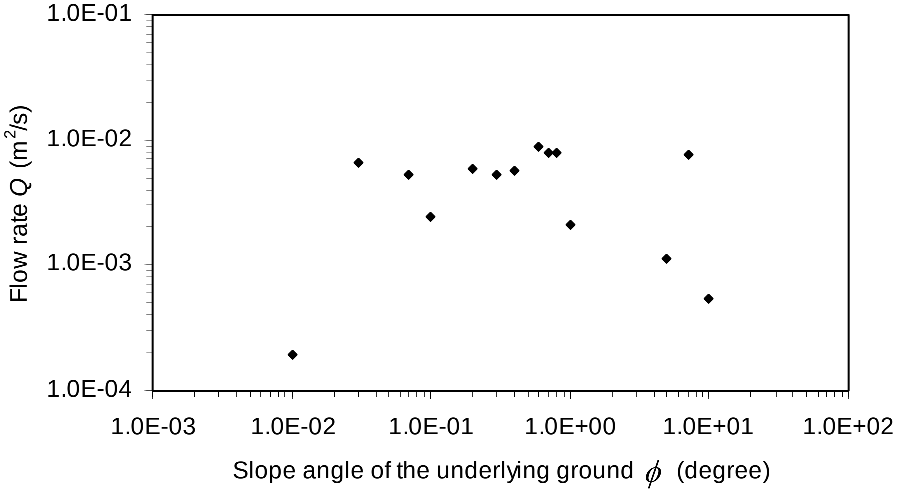

Figure 2.11: Calculated flow rate between the bottom surface of block and underlying ground using Harbitz et al.'s solution

2.5.1.3 Modification of Harbitz et al.'s solution

In an attempt in this study to reduce the problems of numerical stability in Harbitz et al.'s solution, the solution was modified. A force R_{add} was added to the block in the negative x direction. The force R_{add} was assumed to be produced by a kinetic pressure p_u on the leading edge of the block. The pressure p_u was assumed to be uniform and equal to the stagnation pressure, p_{stag}, calculated as:

$$p_{stag} = \frac{1}{2}\rho_w U^2 \tag{2.40}$$

Using the same input conditions as in Table 2.3, the numerical results from the modified solution are shown in Figures 2.12 to 2.15 along with those from the original solution. In all cases stable numerical results were obtained with the modified solution. The component of the effective weight of the block G' in the x direction is the driving force applied on the block down slope. This driving force is balanced by the total resistance R on the block because the block is assumed to be in a steady state of motion. Therefore the total resistance R can be calculated as:

$$R = G' \sin\phi \tag{2.41}$$

The ratio of the added force R_{add} due to the kinetic pressure on the leading edge of the block to the total resistance R is plotted versus the slope angle ϕ for all the cases in Figure 2.16. As shown in Figure 2.16, when the slope becomes steeper, the effect of the added force R_{add} becomes more significant. Therefore Harbitz, et al.'s assumption that the kinetic pressure p_u along the leading edge of the block was negligible does not appear to be reasonable when the slope becomes steep. Neglect of the kinetic pressure p_u along the leading edge of the block is believed to be the cause of numerical instability in Harbitz et al.'s solution.

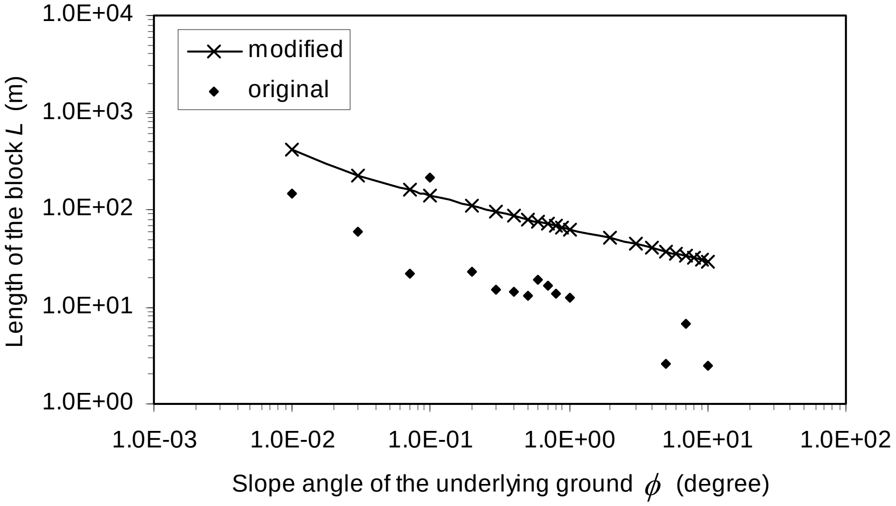

Figure 2.12: Calculated length of the block using Harbitz et al.'s original solution and modified solution

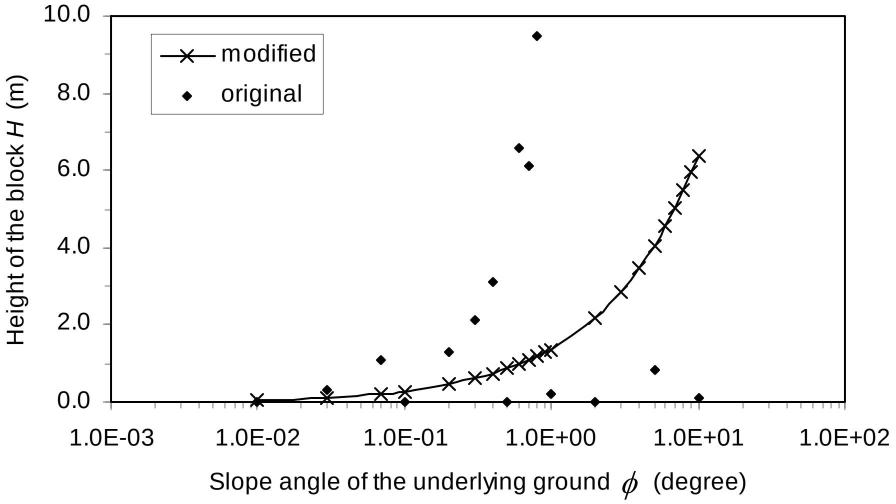

Figure 2.13: Calculated height of the block using Harbitz et al.'s original solution and modified solution

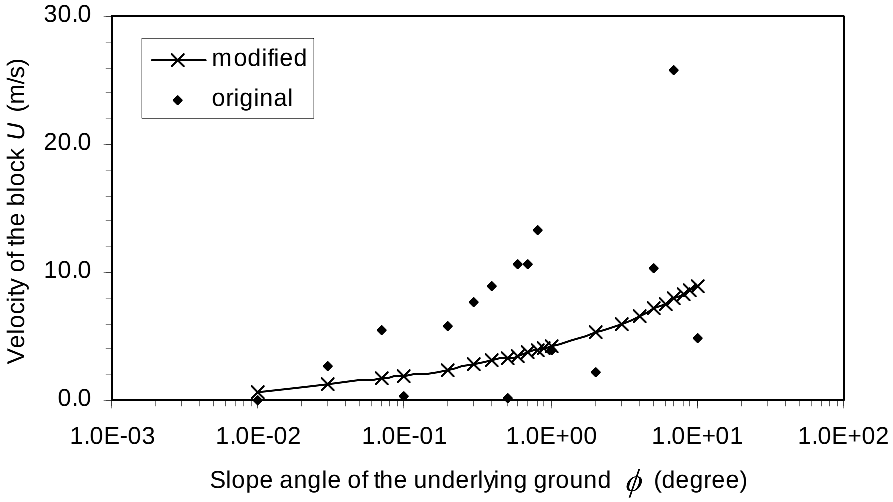

Figure 2.14: Calculated velocity of the block using Harbitz et al.'s original solution and modified solution

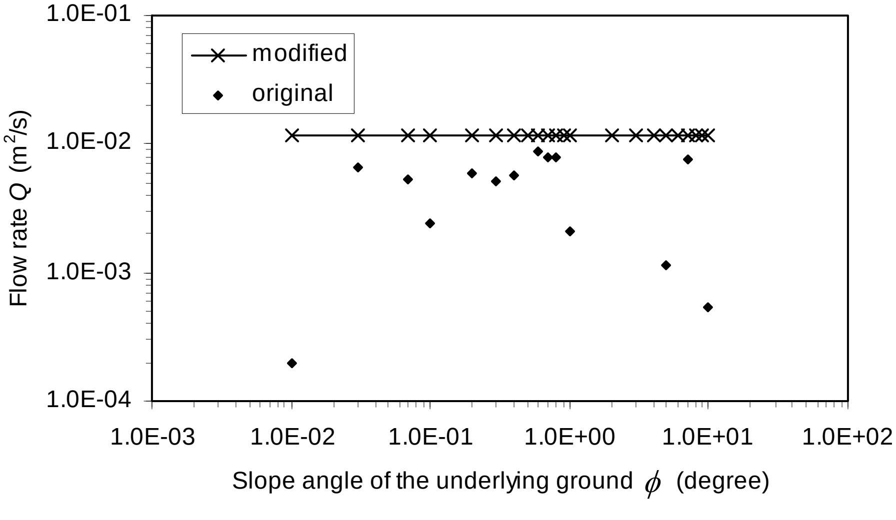

Figure 2.15: Calculated flow rate between the bottom surface of block and underlying ground using Harbitz et al.'s original solution and modified solution

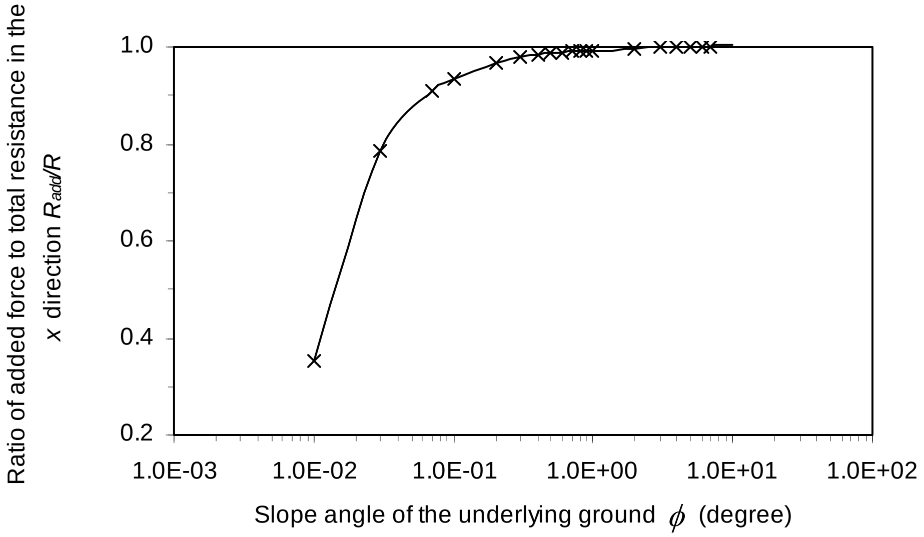

Figure 2.16: Variation of the ratios R_{add}/R with slope angle ϕ

2.5.1.4 Limitations of Harbitz et al.'s solution

Without the modifications described in the previous section, the solution by Harbitz et al. is numerically unstable. The deficiency of Harbitz et al.'s solution is apparently due to neglect of the kinetic pressure p_u along the leading edge of the block. The effect of the pressure p_u can be significant as the ratio of length to height L/H decreases and the slope angle ϕ increases. Therefore the assumption that the pressure, p_u, along the leading edge of the block is negligible is not valid especially as the slope angle ϕ increases.

2.5.2 Examination of on-set condition for hydroplaning

As the on-set condition for hydroplaning, different critical values of Froude number $Fr_{d,crit}$ have been reported by De Blasio et al. (2004) and Mohrig et al. (1998).

De Blasio et al. (2004) assumed that the critical value of Froude number $Fr_{d,crit}$ is 1.0 for the slide mass to start hydroplaning. In contrast, Mohrig et al. (1998) reported that the minimum value of the Froude number Fr_d was 0.3 for a slide mass to hydroplane.

In order to exam the on-set condition for hydroplaning, the physical meaning of Froude number Fr_d is studied as follows. At first, rearrangement of Equation 2.1 gives

$$\frac{1}{2}Fr_d^2 = \frac{\frac{1}{2}\rho_w U^2}{(\rho_d - \rho_w)gH\cos\theta} \tag{2.42}$$

Or in terms of the stagnation pressure given be Equation 2.40

$$\frac{1}{2}Fr_d^2 = \frac{p_{stag}}{(\rho_d - \rho_w)gH\cos\theta} \tag{2.43}$$

The normal stress on the bottom surface σ_w caused by the effective weight of the slide mass can be calculated as

$$\sigma_w = (\rho_s - \rho_w)gH\cos\phi \tag{2.44}$$

Substitute Equation 2.44 into 2.43 gives:

$$\frac{1}{2}Fr_d^2 = \frac{p_{stag}}{\sigma_w} \tag{2.45}$$

Rearrangement of Equation 2.45 gives:

$$Fr_d = \sqrt{\frac{2p_{stag}}{\sigma_w}} \tag{2.46}$$

Thus Froude number Fr_d represents the magnitude of the stagnation pressure p_{stag} relative to the normal stress σ_w and suggests the on-set condition of hydroplaning is related to the stresses and forces applied on the side mass by the surrounding fluid and underlying ground.

Hydroplaning might be expected to occur when the stagnation pressure p_{stag} is equal to the normal stress σ_w and the total force on the slide mass in the direction normal to the underlying slope is zero. In this case, the theoretical critical Froude number for hydroplaning to happen $Fr_{d,crit}$ should be $\sqrt{2}$ according to Equation 2.46. However values of the critical Froude number $Fr_{d,crit}$ were 1.0 and 0.3 according to De Blasio et al. and Mohrig et al, respectively.

The difference among De Blasio et al.'s assumption, Mohrig et al.'s experimental observations and the theoretical value of the critical Froude number $Fr_{d,crit}$ suggests further study is needed for the stresses on the slide mass applied by the surrounding fluid in order to understand hydroplaning of subaqueous slides.

2.6 Future Research on Hydroplaning of Subaqueous Slides

The limitations of existing models for subaqueous slides involving hydroplaning require further study on the mechanism of hydroplaning and its effect on a slide. In order to better understand hydroplaning, the stresses and forces on the slide mass applied by the surrounding fluid were studied numerically. The numerical modeling is described in the next chapter.

Chapter 3: Study of Hydrodynamic Stresses

In order to understand better the motion of subaqueous slides and the occurrence of hydroplaning, the stresses applied on the slide by the surrounding water need to be studied further. In this chapter, numerical analyses performed to study the flow of water around a sliding mass and the hydrodynamic stresses applied on the mass by the surrounding fluid are presented. Commercial software known as, Fluent 6.1, was used for the numerical modeling. The numerical model, its implementation, results of numerical analyses and conclusions are presented in this chapter.

3.1 Numerical Model

A numerical model was constructed to study the forces applied by the surrounding fluid on a slide mass moving through water. For the numerical model, the slide mass was assumed to have a constant shape and velocity. The slide mass was represented by a streamline shaped body as shown in Figure 3.1. The front surface of the slide mass is shown in Figure 3.2 with more detail. The portion from point I to point S is a circular arc. In the local coordinate system $q-o-m$ as shown in Figure 3.3, the arc from point I to point S is expressed as:

$$q^2 + m^2 = r^2 \qquad for \quad 0 \le q \le r \qquad and \qquad 0 \le m \le r) \tag{3.1}$$

Where r is the radius of the arc as shown in Figure 3.1. The curve from point I to point J is part of an ellipse. In the local coordinate system $b-o-a$ as shown in Figure 3.4, the curve from point I to point J is expressed as:

$$\left(\frac{b}{w}\right)^2 + \left(\frac{a}{H-r}\right)^2 = 1 \qquad for \quad 0 \le b \le w \qquad and \qquad 0 \le a \le (H-r) \tag{3.2}$$

where H is the height of the slide mass, and w is the width of the front portion of the slide mass as shown in Figure 3.1. The ratio between the height of the slide mass (H) and the width of the front portion (w) is defined as the "height-to-width ratios" (H/w). The dimension of the slide mass normal to the $x-o-y$ plane in Figure 3.1 is assumed to be infinite. For modeling purposes, the reference for the coordinate system is located on the slide mass, and the surrounding water is assumed to move as steady 2-D flow around a fixed rigid body (the slide mass). The velocities u and v of the surrounding water far away from the slide mass are referred to as "free field velocities". In the following discussion, the free field velocity is represented by the symbol U in the x direction and is assumed to be zero in the y direction. A Reynolds-Stress turbulent model was used to simulate the flow. A gap is assumed between the slide mass and the underlying ground when hydroplaning occurs. The bottom surface of the slide mass is assumed to be parallel to the surface of the underlying ground. The distance between the bottom surface of the slide mass and the underlying ground is designated as h. The boundary conditions for the flow are illustrated in Figure 3.5 and described as follows:

1. along the left edge of the calculation domain ($x=0$), the velocities are equal to the free field velocities, i.e. $u=U$ and $v=0$;
2. at the top edge of the calculation domain, the velocities are equal to the free field velocities, i.e. $u=U$ and $v=0$;
3. along the right edge of the calculation domain, the flow is assumed to be fully developed and, thus, does not change along the horizontal direction, i.e. $\frac{\partial u}{\partial x}=\frac{\partial v}{\partial x}=0$;

4. the bottom edge of the calculation domain is treated as a moving, non-slip wall representing the ground surface moving relative to the slide mass with a constant horizontal velocity, i.e. $u = U$ and $v = 0$;
5. the surfaces of the slide mass are stationary non-slip walls because the slide mass does not move relative to itself, i.e. $u = 0$ and $v = 0$.

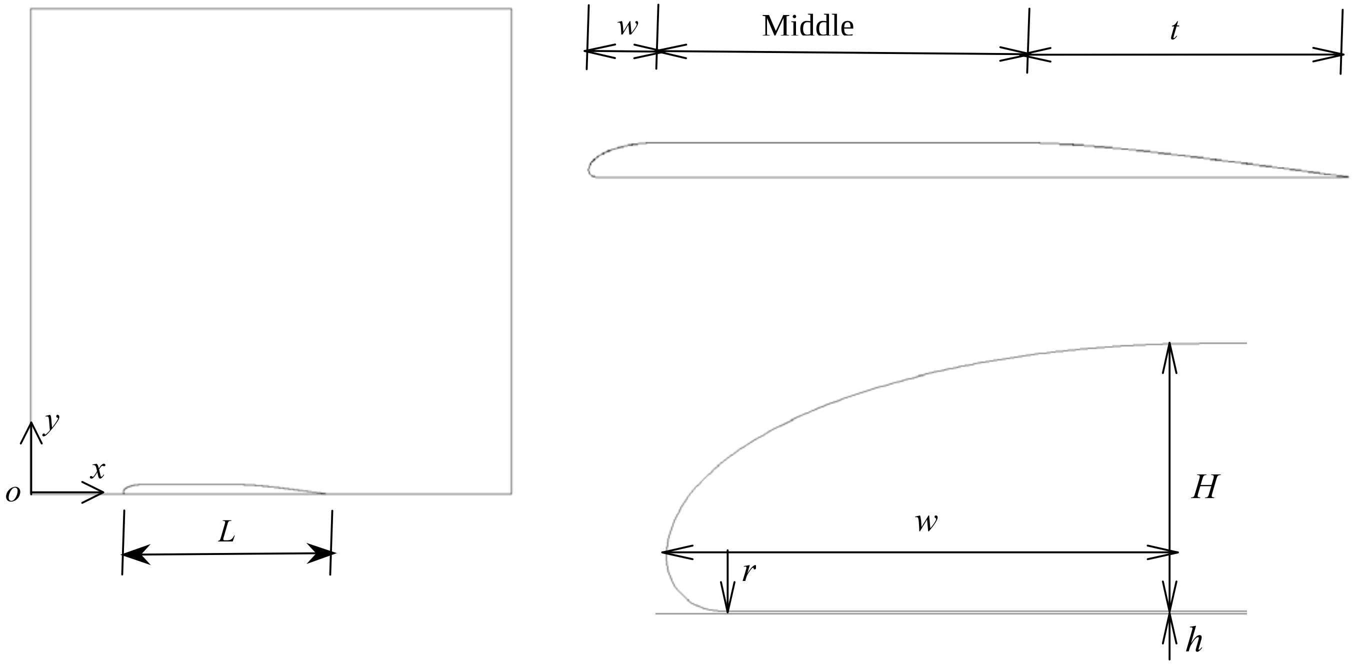

Figure 3.1: Geometry of the numerical model

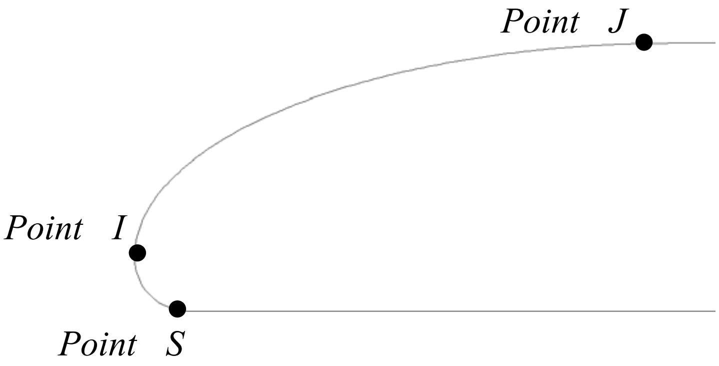

Figure 3.2: Front of the slide mass

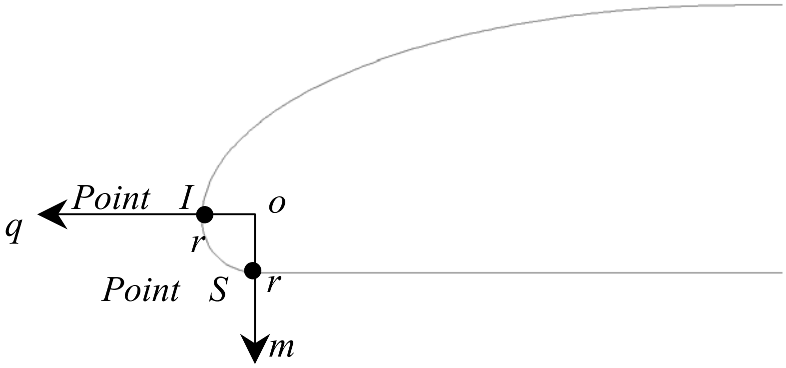

Figure 3.3: Curve from point I to point S

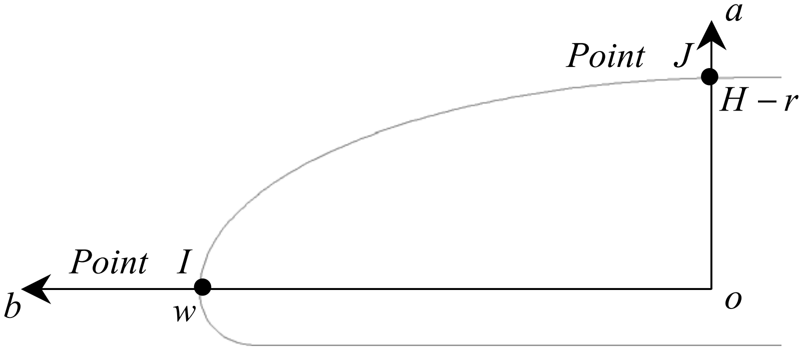

Figure 3.4: Curve from point I to point J

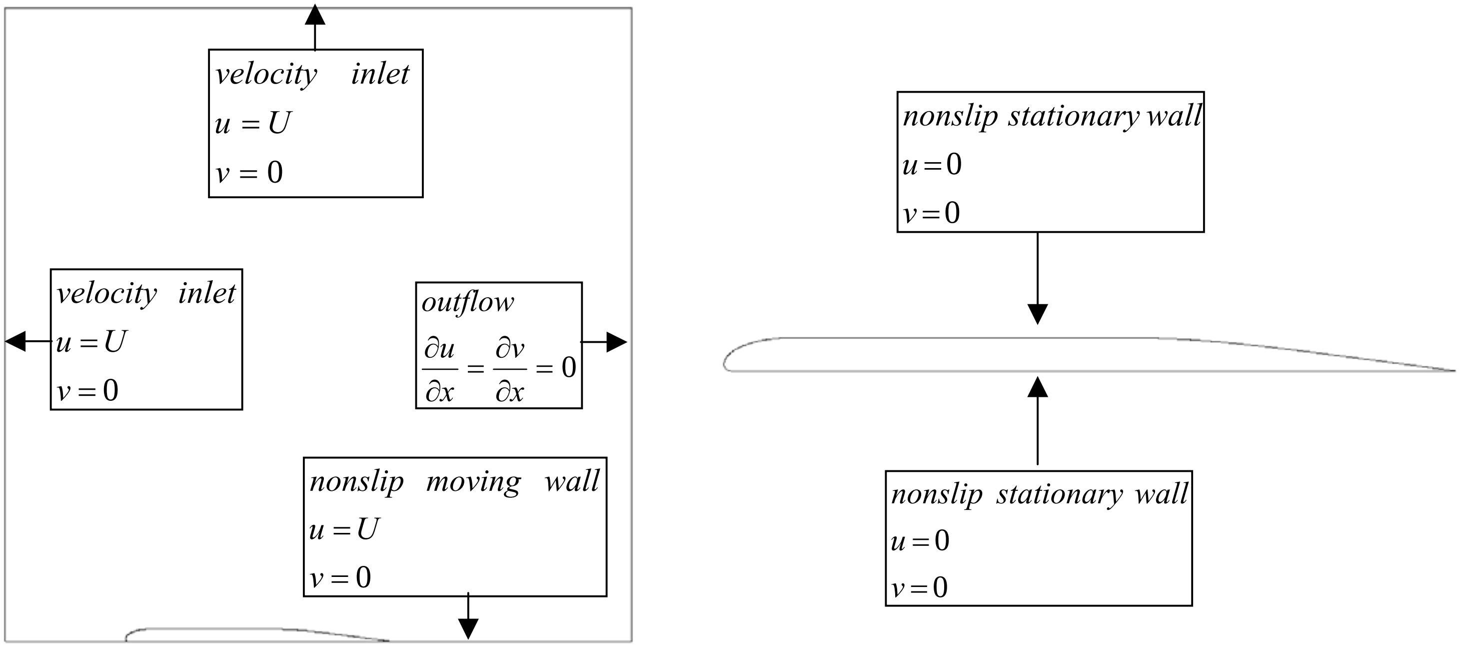

Figure 3.5: Boundary conditions for the numerical model

Fluent uses an iterative scheme to solve the governing equations of flow. Convergence is determined based on the values of scaled residuals defined as the ratios of the corrections to the primitive variables divided by the values of the primitive variables themselves for any given iteration. The primitive variables include horizontal velocity, vertical velocity and mass flow rate of the fluid. For example, the scaled residual for the horizontal velocity at the $i+1$ iteration is calculated as

$$e_u(i+1) = \frac{|u(i+1) - u(i)|}{|u(i+1)|} \tag{3.3}$$

where $u(i+1)$ is the value of horizontal velocity calculated in the $(i+1)th$ iteration, $u(i)$ is the value of horizontal velocity calculated in the $(i)th$ iteration and i is the number of iterations. Scaled residuals were required to be smaller than 10^{-5} for convergence.

The commercial software known as Gambit 2.1 was used as the preprocessor for Fluent. Gambit was used to model the geometry of the calculation domain and to generate meshes.

3.2 Numerical Cases

Ten cases were analyzed with Fluent. The flow conditions and objective of the ten cases are summarized in Table 3.1.

Table 3.1: Flow conditions and functions for numerical cases

Case No.	Free field velocity U (m/s)	Distance between the bottom surface of the slide mass and underlying ground h (m)	Height-to-width ratio of front (H/w)	Objective
1	$u = 1 \quad v = 0$	0.01	0.5	Base case compared with Cases 2 to 10
2	$u = 10 \quad v = 0$	0.01	0.5	Compared with Case 1 to study the effect of slide velocity
3	$u = 1 \quad v = 0$	0.02	0.5	Compared with Case 1 to study the effect of gap thickness
4	$u = 1 \quad v = 0$	0.05	0.5	
5	$u = 1 \quad v = 0$	0.1	0.5	
6	$u = 1 \quad v = 0$	1	0.5	
7	$u = 1 \quad v = 0$	10	0.5	
8	$u = 1 \quad v = 0$	50	0.5	
9	$u = 1 \quad v = 0$	0	0.5	
10	$u = 1 \quad v = 0$	0	2.0	Compared with Case 9 to study the effect of frontal shape

3.3 Numerical Results

The various flow conditions and numerical results for the ten cases are discussed in this section. The results for selected cases are also compared to examine the effects of flow conditions on the hydrodynamic stresses. For presentation purposes, the hydrodynamic stresses including kinetic pressure and viscous shear are normalized by dividing the values by the corresponding stagnation pressure p_{stag} defined in Equation 2.38. The stagnation pressure p_{stag} is computed from Equation 2.38 using the free field velocity, U.

3.3.1 Hydrodynamic stresses

For Case 1, the geometry of the flow domain and boundary conditions are as shown in Figures 3.6 and 3.7. The free field velocity, U, in the x direction is 1 m/s. The distance between the bottom surface of the slide mass and underlying ground h is 0.01 m. The height-to-width ratio, H/w, for the front portion of the slide mass is 0.5. The mesh is shown in Figure 3.8 and consists of 594812 rectangular and triangular elements.

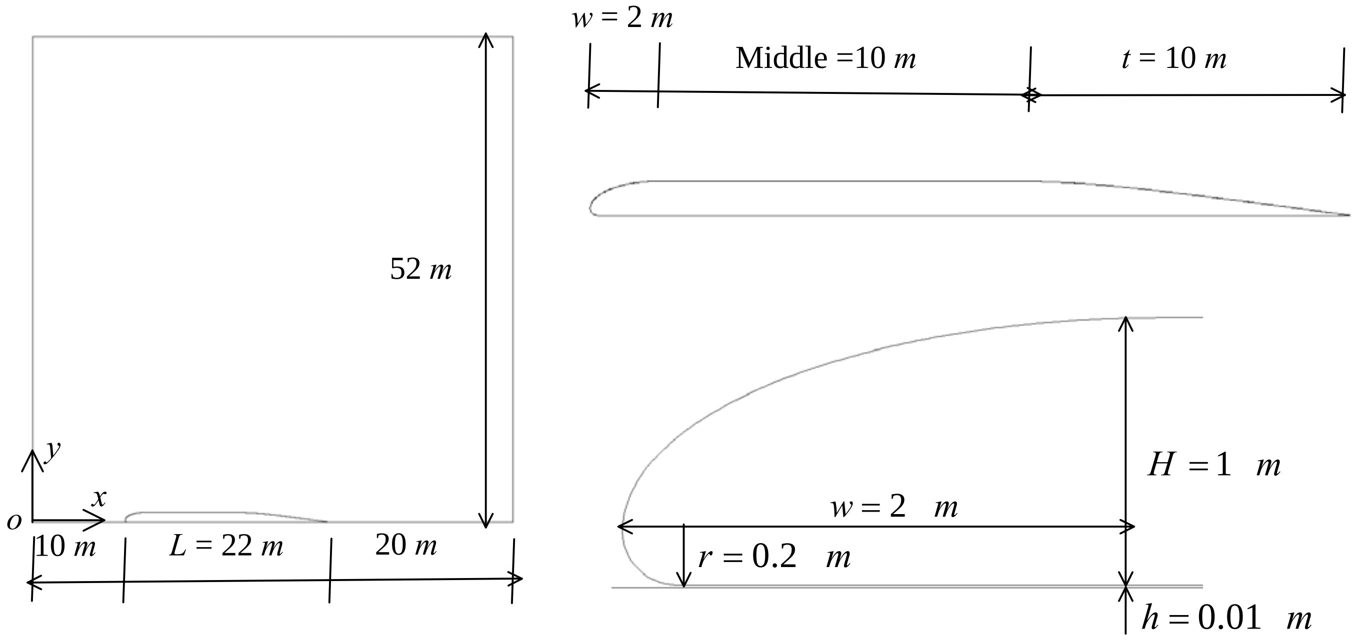

Figure 3.6: Geometry for Case 1 ($U = 1 \ m/s$; $h = 0.01 \ m$; $H/w = 0.5$)

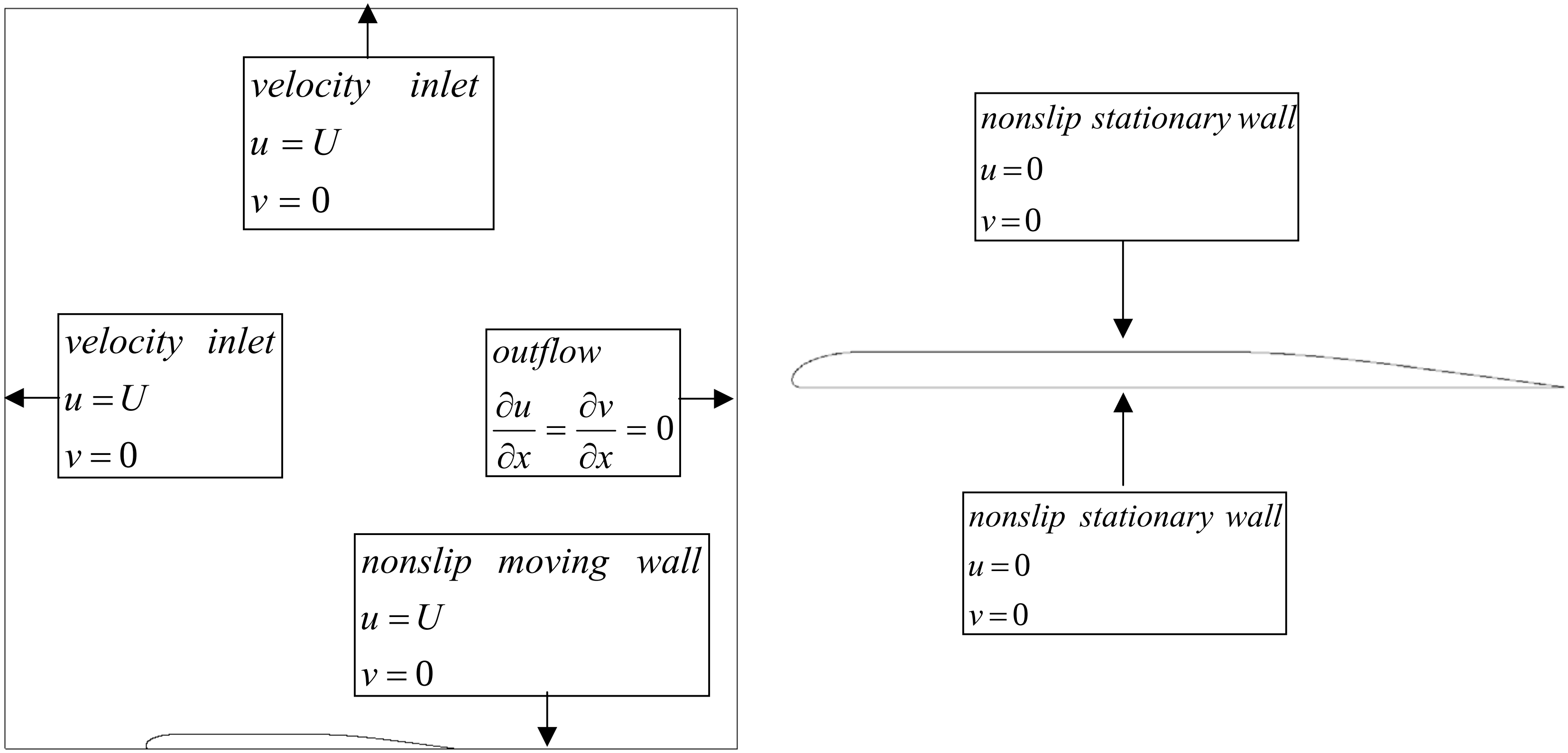

Figure 3.7: Boundary conditions for Case 1 ($U = 1\ m/s$; $h = 0.01\ m$; $H/w = 0.5$)

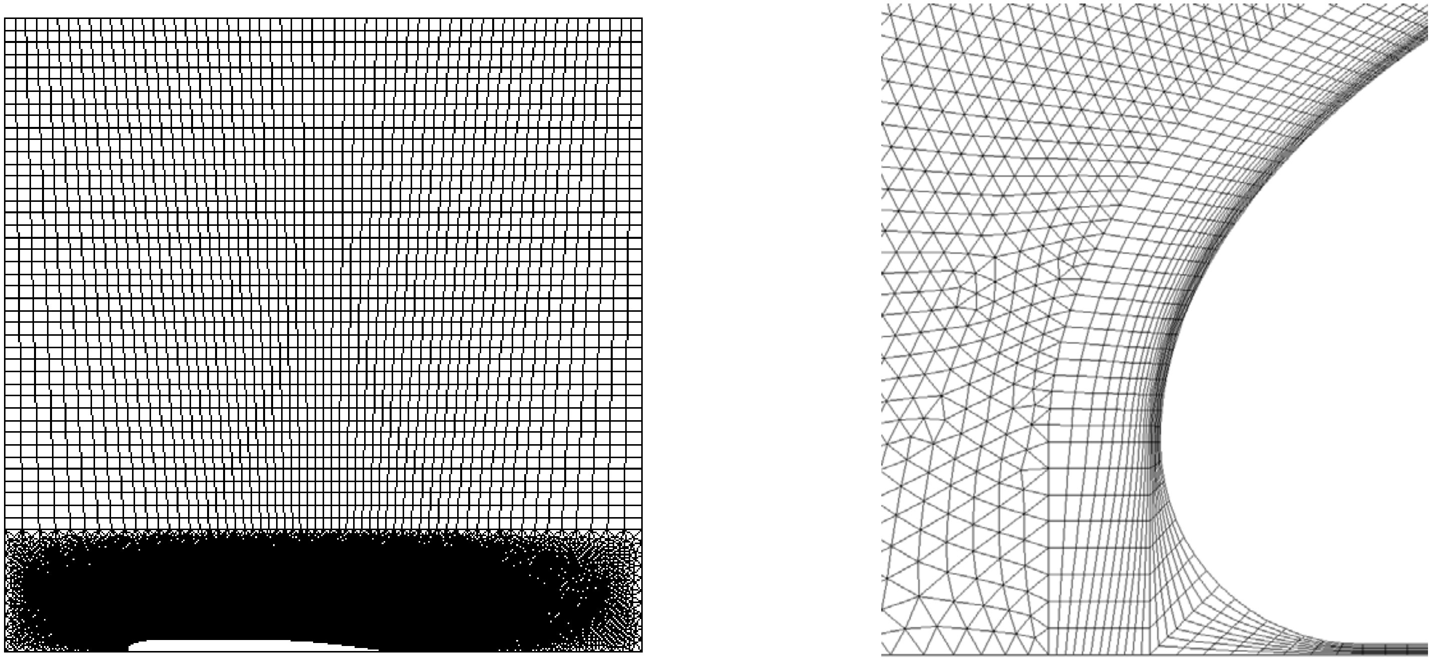

Figure 3.8: Mesh for Case 1 ($U = 1\ m/s$; $h = 0.01\ m$; $H/w = 0.5$)

3.3.1.1 Kinetic pressures

The variation in computed non-dimensional kinetic pressures along the top and bottom surfaces of the slide mass with the horizontal position is shown in Figure 3.9. As shown in Figure 3.9, the non-dimensional kinetic pressure is about 1.0 at the front nose of the slide mass. For discussion of the pressure p_b / p_{stag} along the bottom surface, the bottom surface of the slide mass is divided into two portions. The first portion is the curved portion of the bottom surface from point I to point S as shown previously in Figure 3.2. The second portion is the remaining planar portion of the bottom surface. The length of first curved portion is much smaller than that of the second portion. Therefore, it seems reasonable to neglect the kinetic pressure over the first portion. Along the second portion of the bottom surface, the non-dimensional pressure, p_b / p_{stag} varies linearly. The pressure p_b / p_{stag} at the beginning of the second portion of the bottom surface of the slide mass is about 0.88 and marked by an inverted triangle in Figure 3.9. The pressure p_b / p_{stag} decreases to about 0.3 at the tail of the side mass.

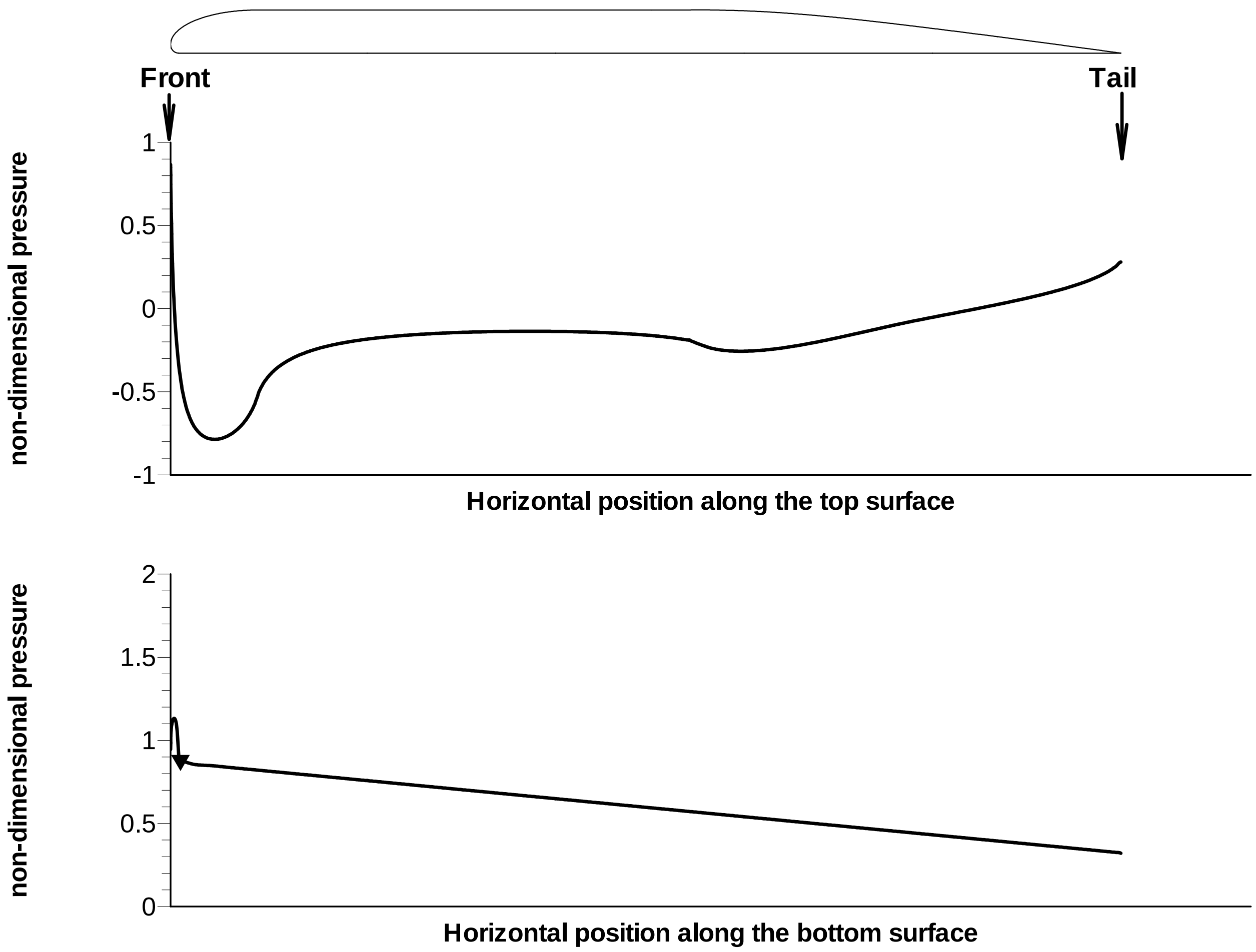

Figure 3.9: Non-dimensional kinetic pressures for Case 1($U = 1 \ \ m/s$; $h = 0.01 \ \ m$; $H/w = 0.5$)

For discussion of the normalized pressure p_t / p_{stag} along the top surface of the slide mass, the top surface is divided into three portions. The first portion is the curved portion from point I to point J shown previously in Figure 3.2. The pressure p_t / p_{stag} along this portion is negative and provides lift on the slide mass. The second portion is the middle portion of the top surface as shown in Figure 3.1. The normalized pressure p_t / p_{stag} along this portion is approximately constant at -0.1. The third portion is the remainder of the top surface. The normalized pressure p_t / p_{stag} in this portion varies linearly from about -0.1 to 0.3 at the tail end of the slide mass. The negative normalized pressure, p_t / p_{stag}, along the middle portion of the top surface is believed to be a reflection of limitations of the numerical model. As shown in Figure 3.6, the total height of the calculation domain (slide mass and surrounding fluid) is 52 m, which is only about 2.4 times the length of the slide mass (22 m). For natural submarine slides, the slide mass moves along the bottom of the ocean and the depth of the sea water is probably more than 10 times the length of the slide mass. Thus for actual submarine slides, it is reasonable to assume that the top edge of the flow domain is essentially infinitely far from the slide mass. The flow above the middle portion of the slide mass can then be approximated as flow above an infinitesimally thin plate. According to the boundary layer theory (Crowe, and et al. 2000), the kinetic pressure above an infinitesimally thin plate is zero. Therefore, the non-dimensional pressure p_t / p_{stag} on the middle portion of the top surface of an actual submarine slide is probably zero. The non-dimensional pressure p_t / p_{stag} on the tail portion of the top surface increases linearly from zero at the start of tail portion to 0.3 at the end of the tail portion.

3.3.1.2 Re-examination of the on-set condition of hydroplaning

As discussed in section 2.5.2, hydroplaning was expected to occur when the Froude number Fr_d was $\sqrt{2}$ according to Equation 2.46. This expectation was based on a common assumption adopted by Harbitz et al. (2003) and De Blasio et al. (2004) that the kinetic pressure, p_b, along the bottom surface of the slide mass was the only stress applied by the surrounding fluid in the direction normal to the underlying slope. This assumption is clearly unrealistic because the pressure p_t / p_{stag} along the front portion of the slide mass, i.e. the curved portion from point I to point J shown in Figure 3.2, is negative. Taking this negative pressure, p_t / p_{stag}, into consideration, hydroplaning should occur for a stagnation pressure p_{stag} that is smaller than the normal stress σ_w along the bottom surface of the slide mass. Therefore the critical Froude number $Fr_{d,crit}$ for hydroplaning to happen should be smaller than $\sqrt{2}$.

3.3.1.3 Viscous shear stresses

The distributions of the normalized shear stresses along the top and bottom surfaces of the slide mass τ_t / p_{stag}, τ_b / p_{stag} are shown in Figure 3.10. The normalized shear stresses shown in Figure 3.10 are much smaller than the normalized pressures shown in Figure 3.9.

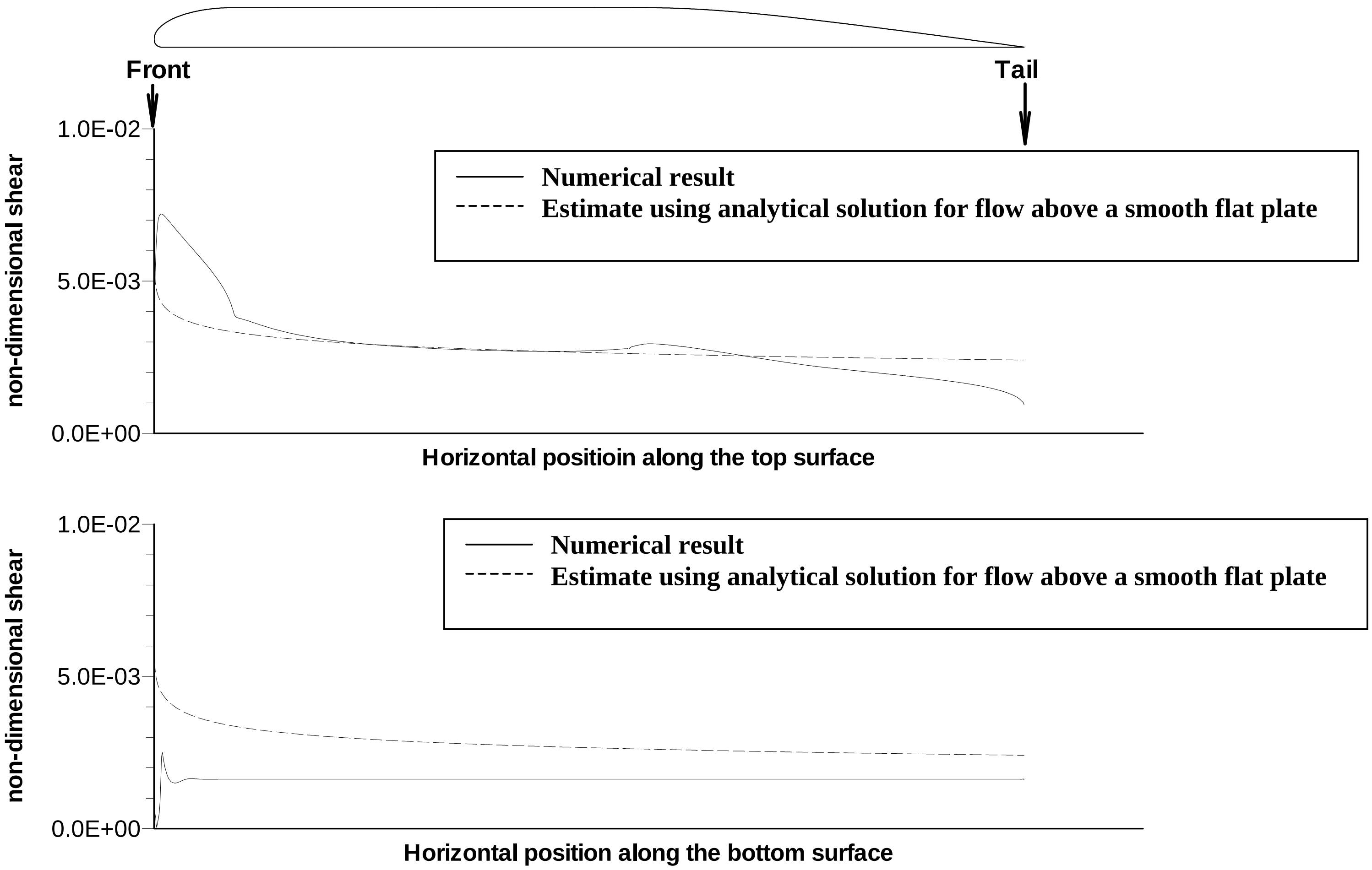

Figure 3.10: Non-dimensional shear stress for Case 1($U = 1\ m/s$; $h = 0.01\ m$; $H/w = 0.5$)

For comparison with the numerical results, the shear stresses along the top and bottom surfaces of the slide mass were also calculated using the analytical solution developed for flow above a smooth flat plate as:

$$\tau_x = \frac{1}{2}\rho_w U^2 \left(\frac{0.027}{\left(\frac{Ux}{\upsilon} \right)^{1/7}} \right) \tag{3.4}$$

where x is the distance from the upstream end of the plate or slide mass to the location of concern , τ_x is the shear stress at a location x , ρ_w is the density of water, U is the free field velocity in the x direction, and υ is the kinematic viscosity of water. Further details regarding the analytical solution can be found in Crowe, Roberson and Elger (2000). The shear stresses calculated using Equation 3.4 were also normalized by the stagnation pressure p_{stag} and plotted in Figure 3.10. Since viscous shear stresses are much smaller than the kinetic pressures on the slide mass, using the analytical solution developed for flow above a smooth flat plate to approximate the viscous shear stresses will not have a significant influence on the estimates about the motion of the slide mass. Therefore, the viscous shear stresses on the slide mass will be approximated using Equation 3.4 in the block model as discussed in Chapter 4.

3.3.2 Effect of free field velocity

In order to study the effect of the free field velocity on the hydrodynamic stresses on a slide mass, Case 2 was analyzed with an free field velocity U of 10 m/s. The geometry for Case 2 is the same as that for Case 1. The distance between the bottom surface of the slide mass and underlying ground h is also 0.01 m, and the height-to-width ratio H / w is 0.5. The same mesh used for Case 1 was used for Case 2.

3.3.2.1 Effect of free field velocity on kinetic pressures

The normalized kinetic pressures for Cases 1 and 2 are shown together in Figure 3.11. The non-dimensional pressures for these two cases are nearly identical. Therefore the influence of free field velocity on the non-dimensional kinetic pressure is negligible.

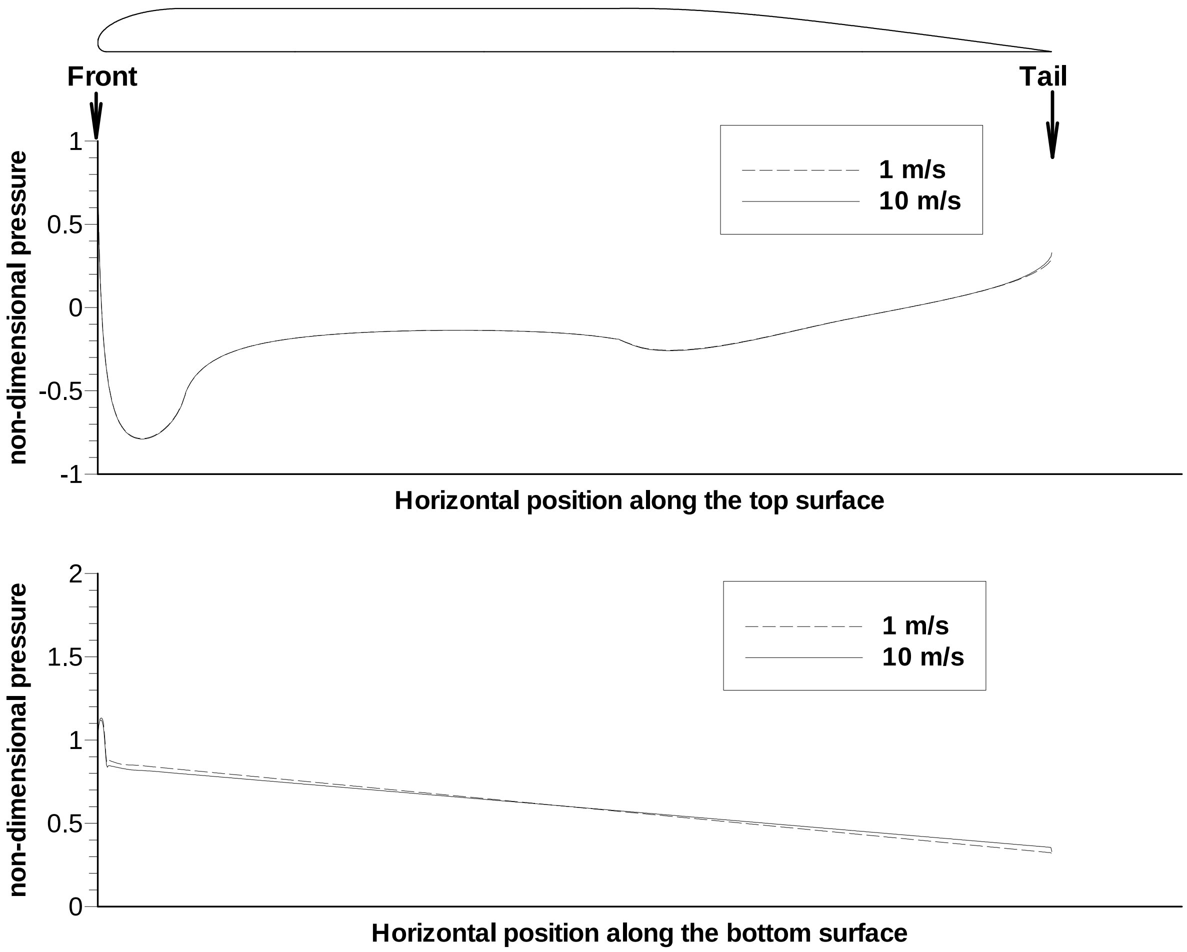

Figure 3.11: Non-dimensional shear stress for Cases 1 and 2($U = 1 \quad m/s$, and $U = 10 \quad m/s$; $h = 0.01 \quad m$; $H/w = 0.5$)

3.3.2.2 Effect of free field velocity on viscous shear stresses

The non-dimensional shear stresses on the surface of the slide mass for Case 2 are shown in Figure 3.12. The shear stresses are also computed using the analytical solution developed for flow above a smooth flat plate (Equation 3.4). For similar reasons discussed in Section 3.3.1.3, the viscous shear stresses on the slide mass will be approximated using the analytical solution developed for flow above a smooth flat plate (Equation 3.4) in the block model (as discussed in Chapter 4) regardless of the free field velocity.

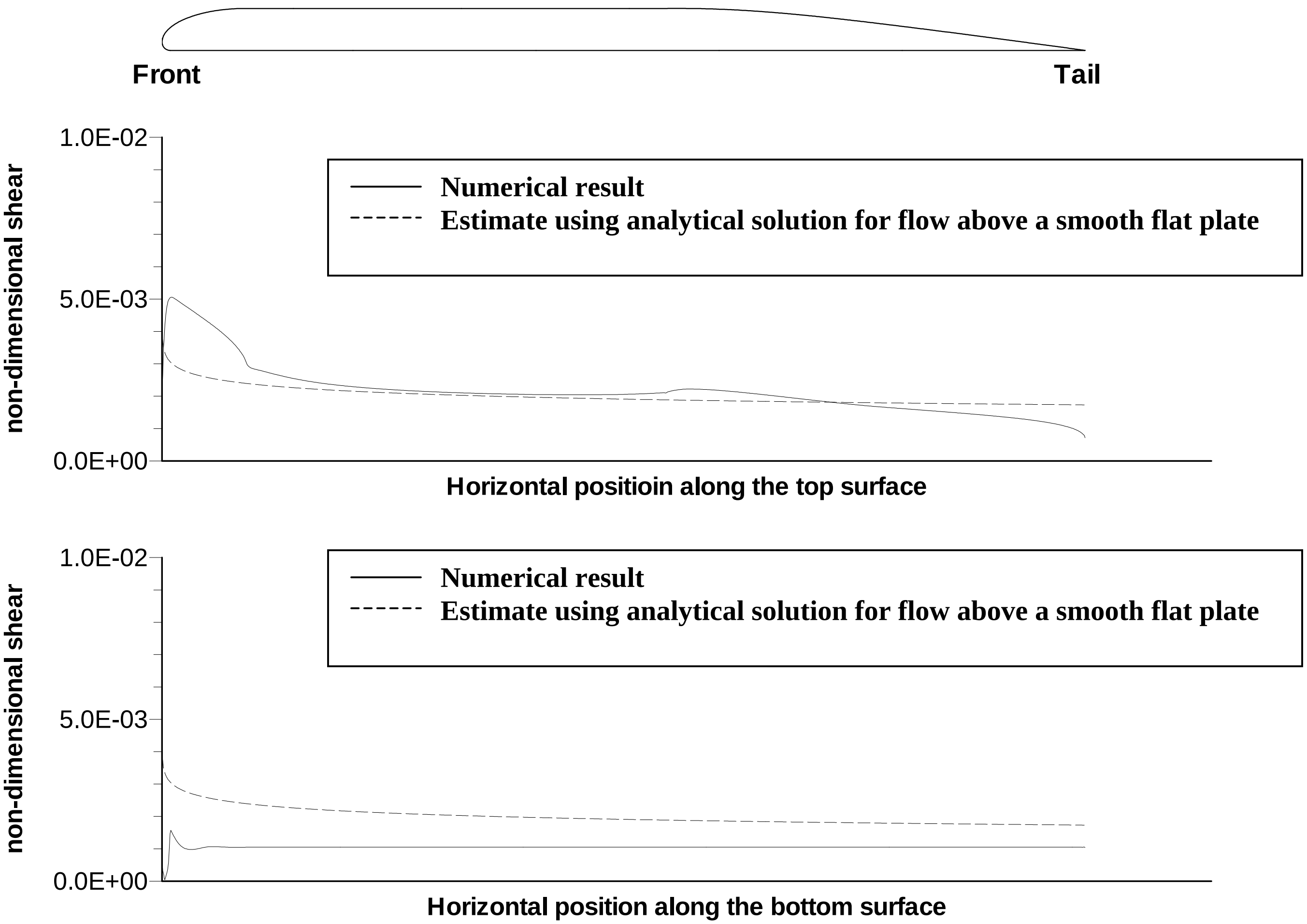

Figure 3.12: Non-dimensional shear stress for Case 2($U = 10$ m/s; $h = 0.01$ m; $H/w = 0.5$)

3.3.3 Effect of distance between the bottom surface of the slide mass and underlying ground

To study the influence of distance between the bottom surface of the slide mass and underlying ground h on the hydrodynamic forces applied to the surfaces of the slide mass, Cases 3 to 8 were analyzed with distances h of 0.02m, 0.05m, 0.1m, 1m, 10m, and 50m respectively.

3.3.3.1 Effect of distance h on kinetic pressures

The non-dimensional kinetic pressures along the surfaces of the slide mass for Cases 3 to 8 are shown in Figures 3.13 through 3.18, respectively. For comparison, the non-dimensional kinetic pressures along the top surface of the slide mass for all six cases are plotted together in Figure 3.19. It can be seen that the change of pressures along the top surface of the slide mass (p_t / p_{stag}) is insignificant as the distance, h, changes.

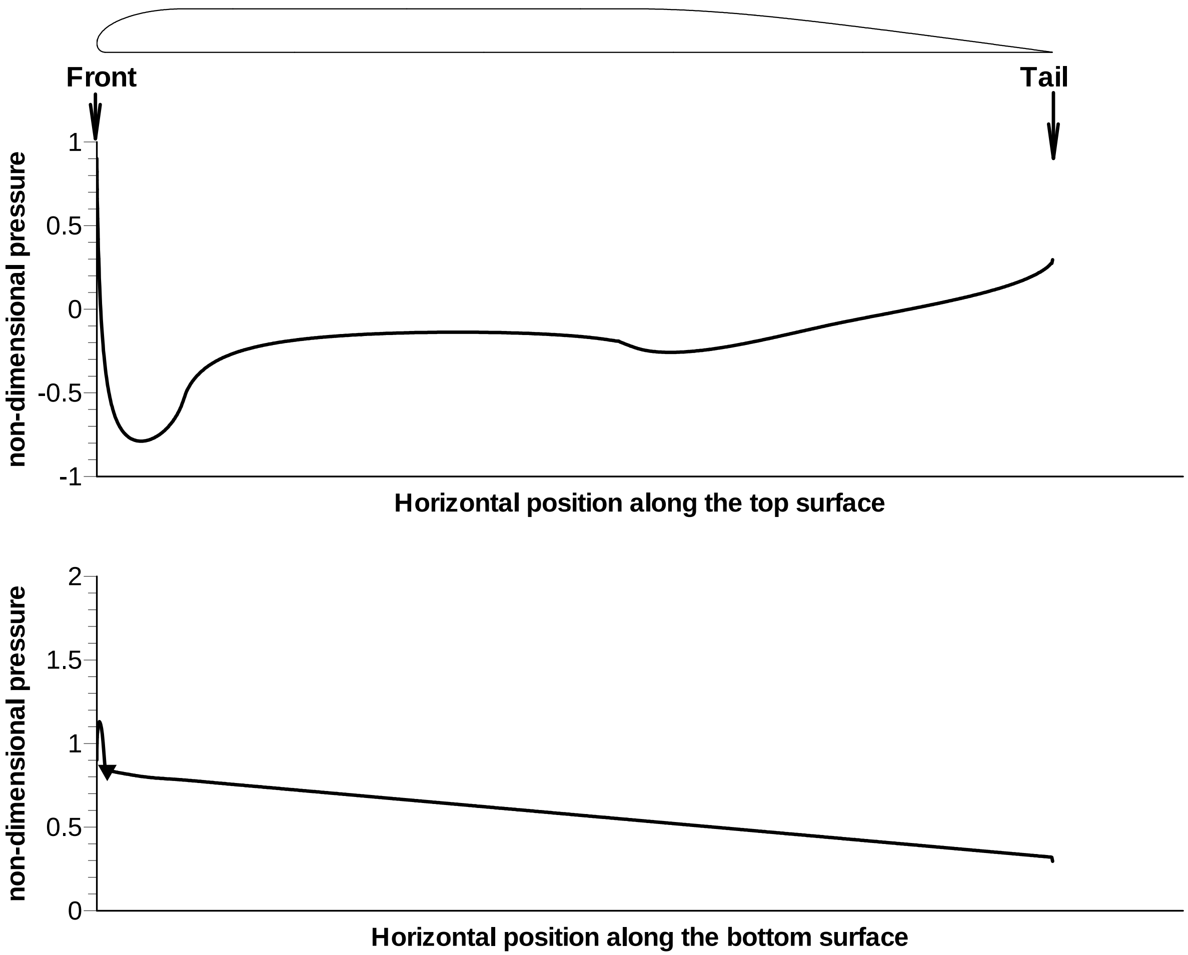

Figure 3.13: Non-dimensional kinetic pressure for Case 3($U = 1\ \ m/s$; $h = 0.02\ \ m$; $H/w = 0.5$)

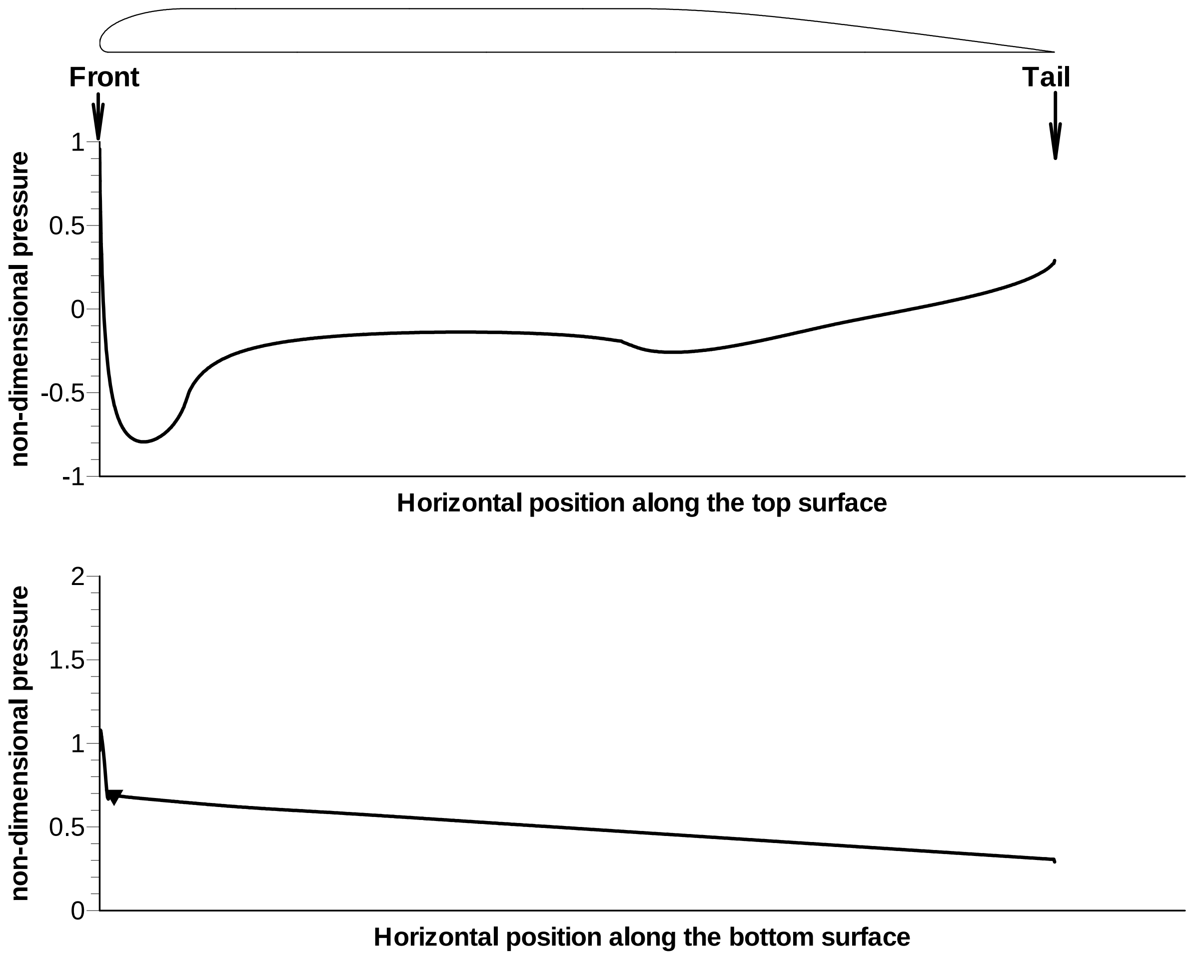

Figure 3.14: Non-dimensional kinetic pressure Case 4($U = 1\ m/s;\ h = 0.05\ m;\ H/w = 0.5$)

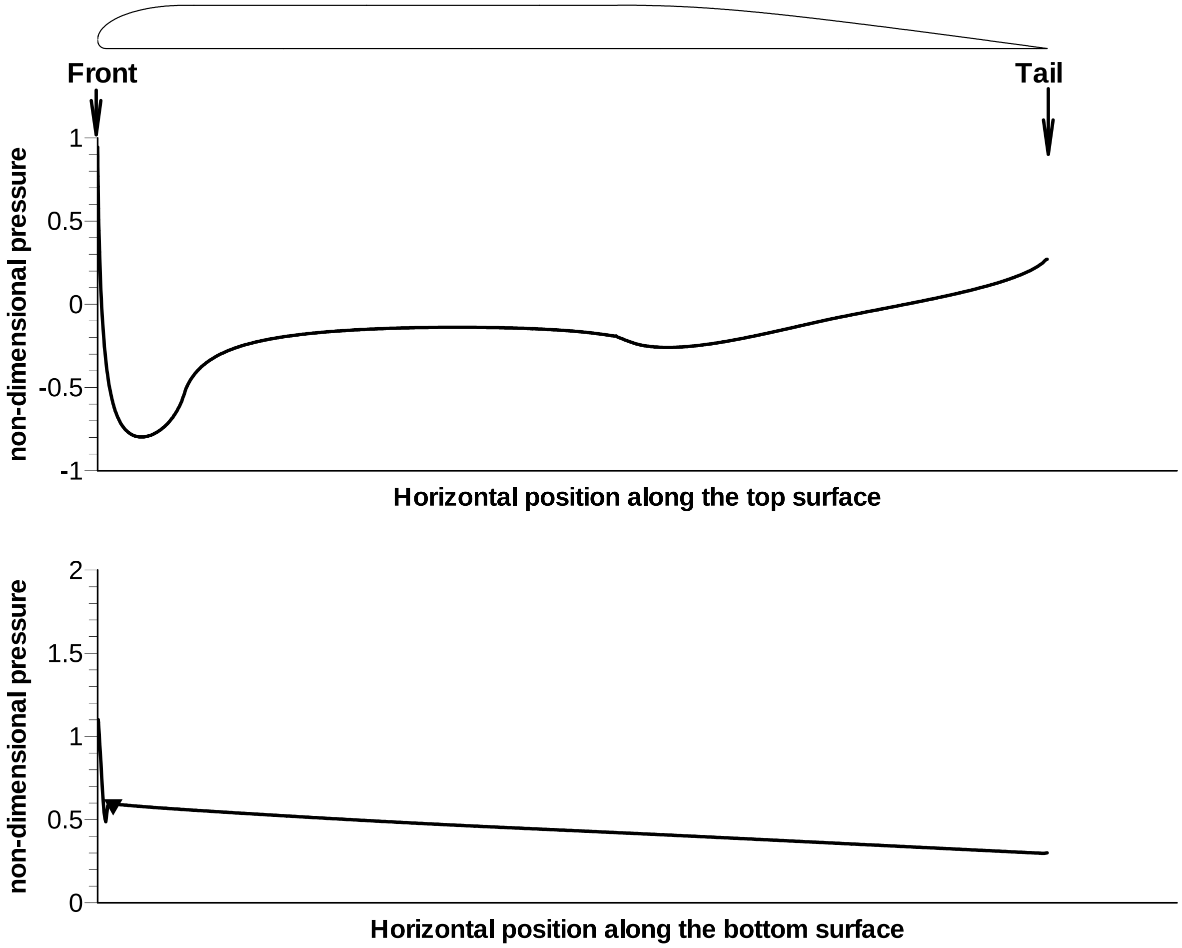

Figure 3.15: Non-dimensional kinetic pressure for Case 5($U = 1 \ m/s$; $h = 0.1 \ m$; $H/w = 0.5$)

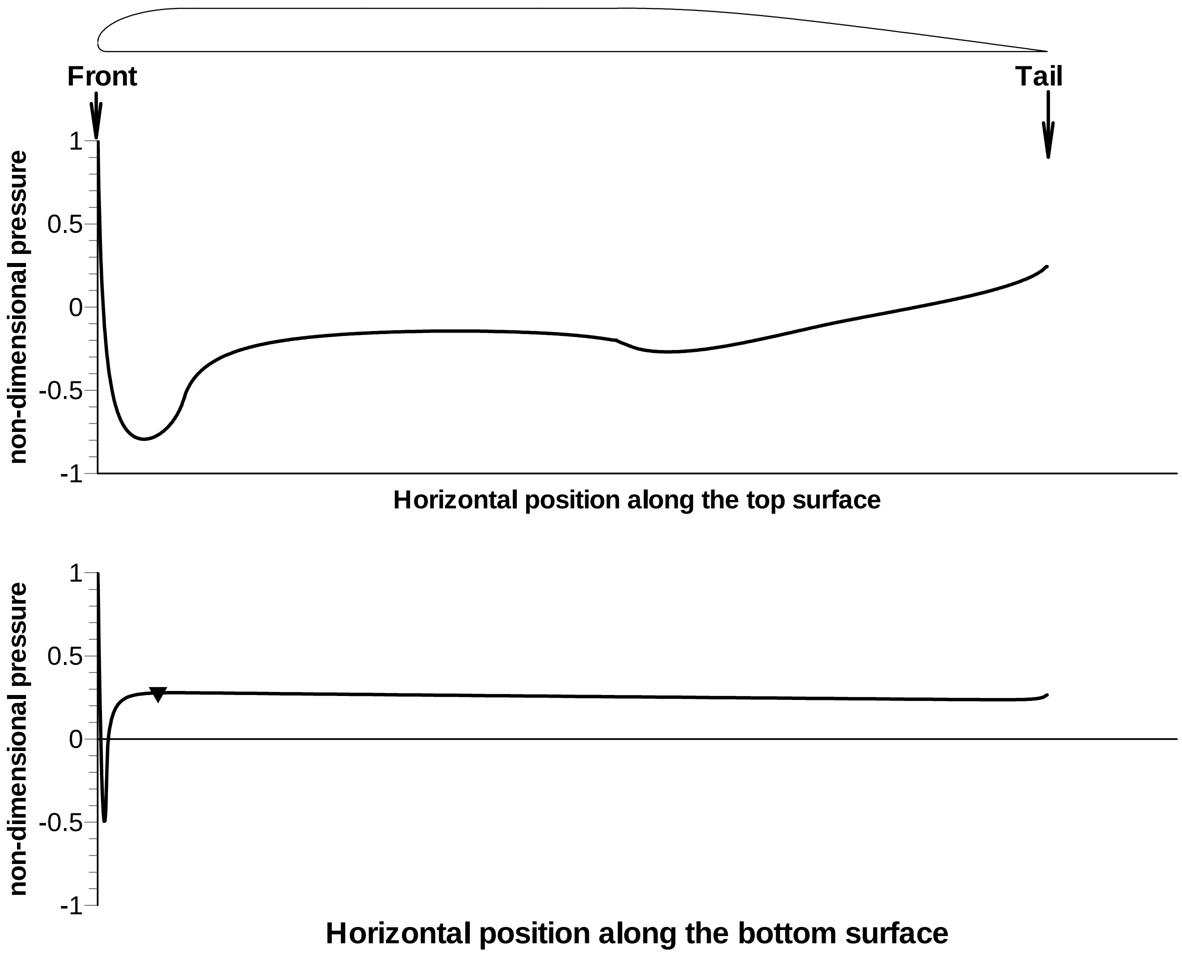

Figure 3.16: Non-dimensional kinetic pressure for Case 6($U = 1\ m/s;\ h = 1\ m;\ H/w = 0.5$)

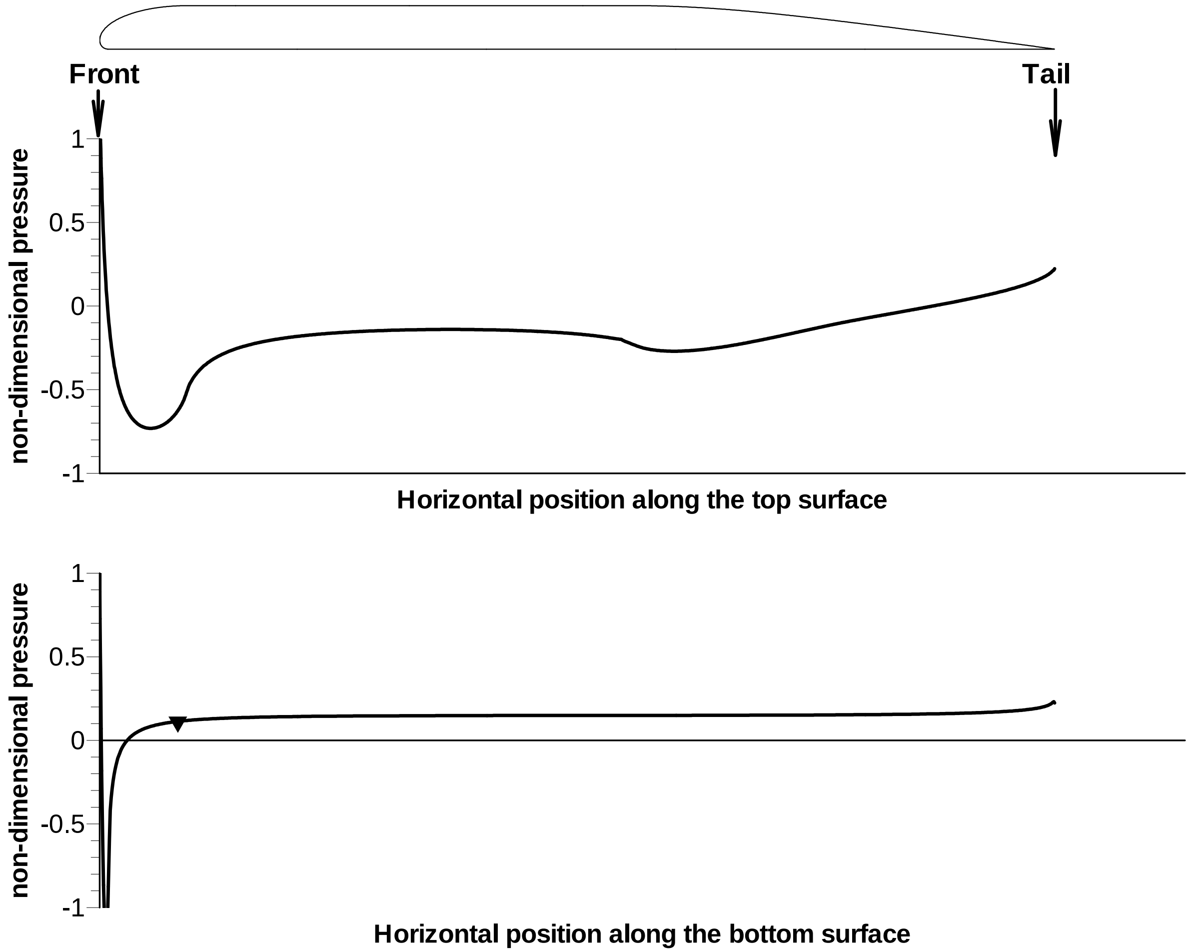

Figure 3.17: Non-dimensional kinetic pressure for Case 7($U = 1\ m/s$; $h = 10\ m$; $H/w = 0.5$)

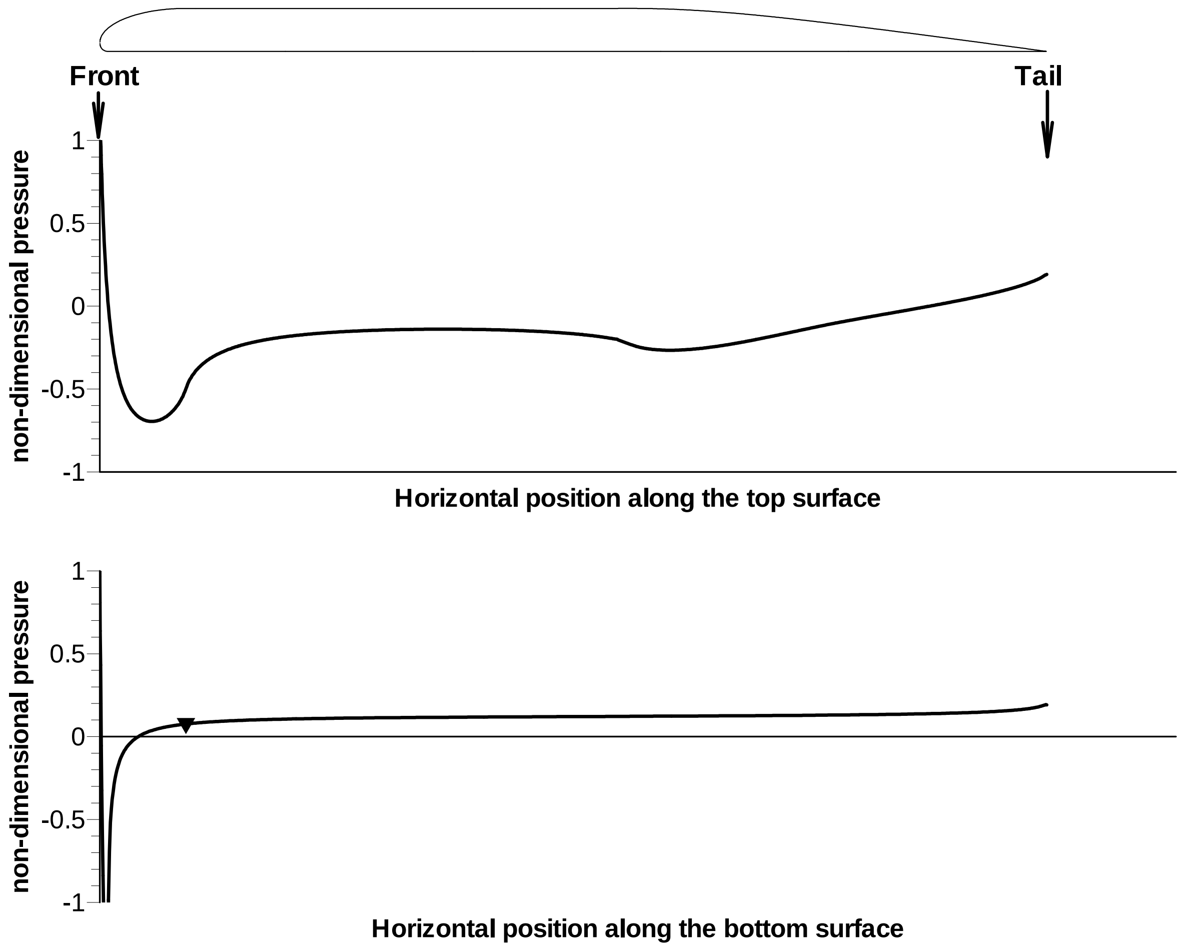

Figure 3.18: Non-dimensional kinetic pressure for Case 8($U = 1 \ m/s$; $h = 50 \ m$; $H/w = 0.5$)

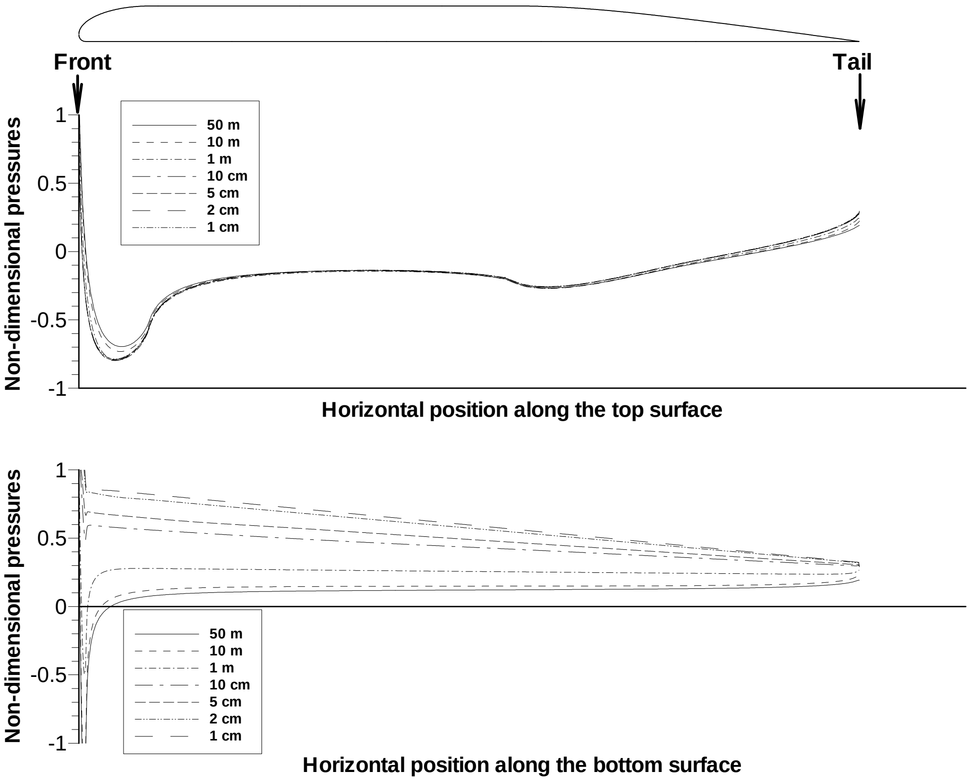

Figure 3.19: Change of non-dimensional kinetic pressure with distance *h*

As shown in Figures 3.13 to 3.18, along the bottom surface of the slide mass the pressures p_b / p_{stag} decrease almost linearly beginning at a point a very short distance behind the front nose of the slide mass and ending at the tail of the slide mass. The pressures p_b / p_{stag} at the beginning of this linear variation are marked by triangles in Figure 3.13 to 3.18. Again for comparison, the non-dimensional pressures at the bottom surface p_b / p_{stag} for all six cases are plotted together in Figure 3.19. It can be seen the non-dimensional pressure along the bottom surface of the slide mass p_b / p_{stag} changes when the distance h changes. The non-dimensional pressures at the beginning of the slide mass where pressures decrease linearly (marked by triangles in Figures 3.13 to 3.18) are plotted against the ratios of distance h to height of the slide mass H (h / H) in Figure 3.20. A smooth curve is fitted to the data points in Figure 3.20. The equation for the curve is as follows

$$\frac{p}{p_{stag}} = \frac{1}{1 + 2.57\left(\frac{h}{H}\right)^{0.58}} \qquad for \qquad h > 0 \tag{3.5}$$

Similarly, the non-dimensional pressures at the tail end of the slide mass are plotted against the ratios h / H in Figure 3.21. A smooth curve is fitted to the data points in Figure 3.21. The equation for the curve is as follows

$$\frac{p}{p_{stag}} = \frac{1}{1 + 0.15\left(\frac{h}{H}\right)^{0.4}} \qquad for \qquad h > 0 \tag{3.6}$$

The equations 3.5 and 3.6 will be used to estimate the kinetic pressure along the bottom surface of the slide mass as discussed in Chapter 4.

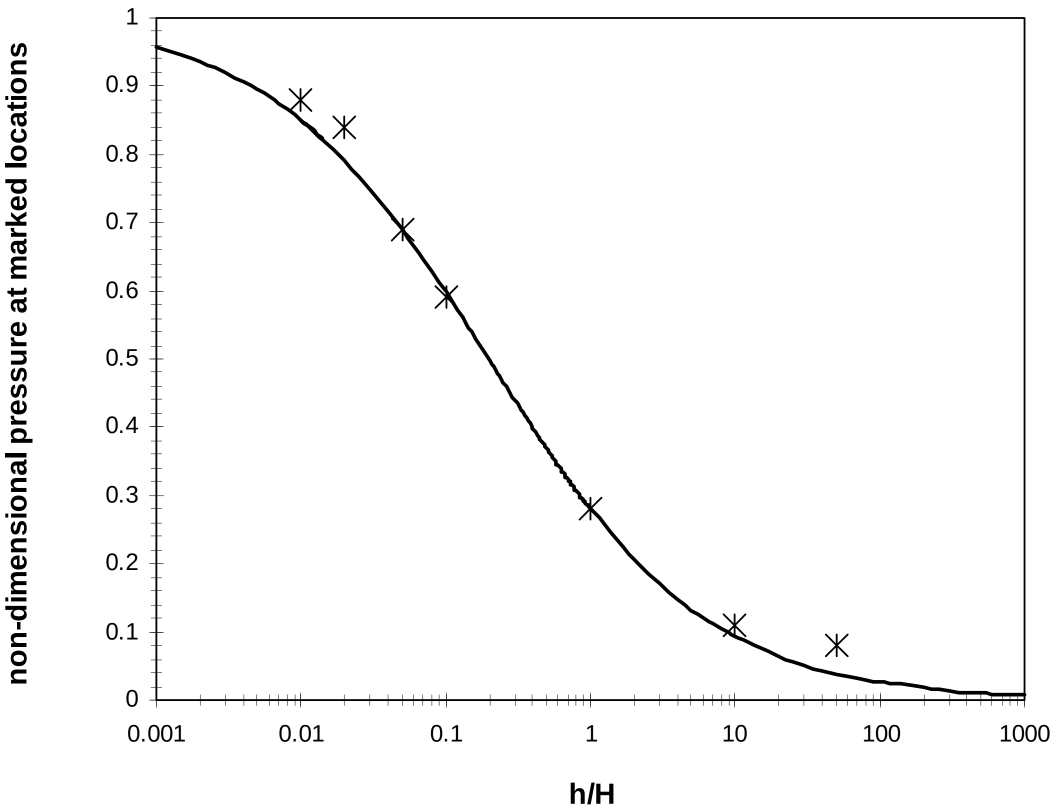

Figure 3.20: Marked non-dimensional kinetic pressures vs h/H

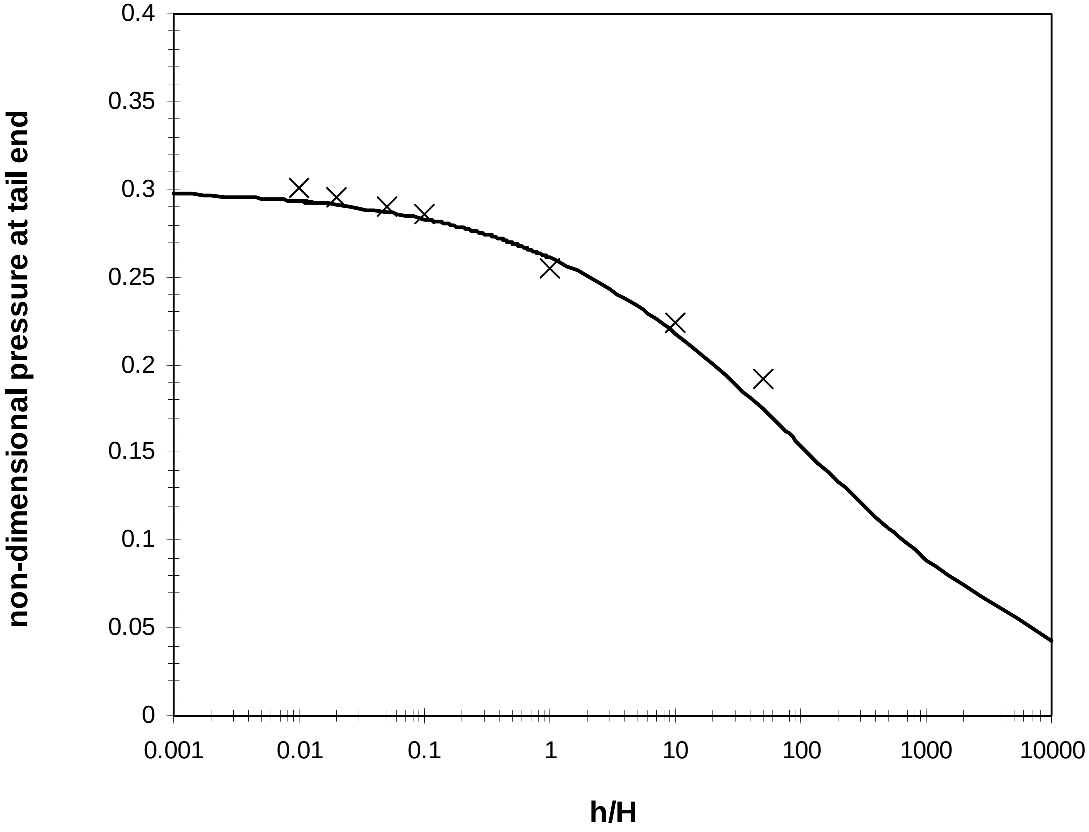

Figure 3.21: Non-dimensional kinetic pressure at tail end of the slide mass vs *h*

3.3.3.2 Effect of distance h on viscous shear stresses

The non-dimensional shear stresses for cases 3 to 8 are shown in Figures 3.22 through 3.27, respectively. The shear stresses calculated using the analytical solution developed for flow above a smooth flat plate (Equation 3.4) are normalized by the stagnation pressure p_{stag} and also plotted in Figures 3.22 to 3.27. For similar reasons discussed in Section 3.3.1.3, the viscous shear stresses on the slide mass will be approximated using the analytical solution developed for flow above a smooth flat plate (Equation 3.4) in the block model (as discussed in Chapter 4) regardless of the distance h, between the bottom surface of the slide mass and underlying ground.

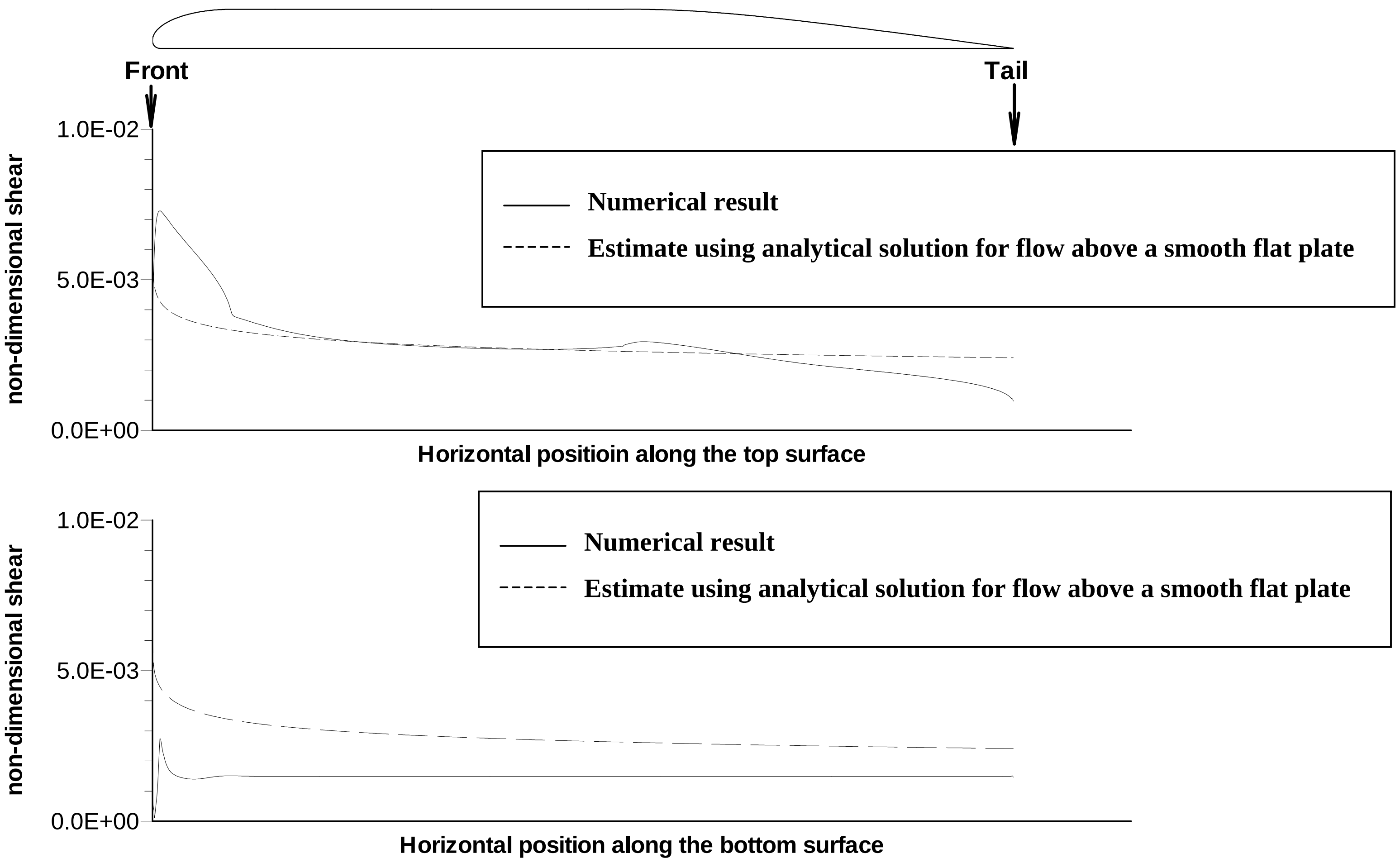

Figure 3.22: Non-dimensional shear stress for Case 3($U = 1 \ m/s$; $h = 0.02 \ m$; $H/w = 0.5$)

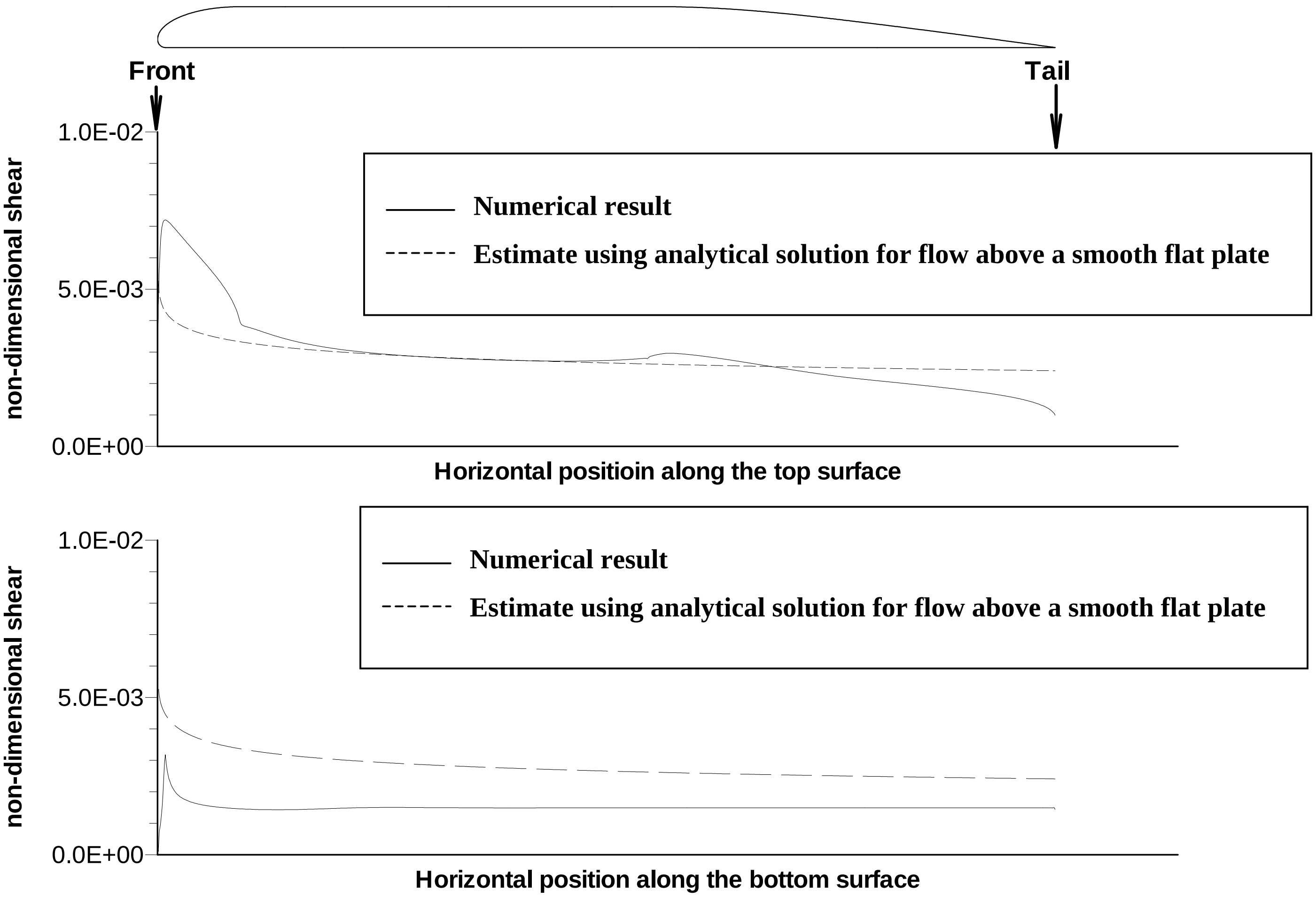

Figure 3.23: Non-dimensional shear stress for Case 4($U = 1$ m/s; $h = 0.05$ m; $H/w = 0.5$)

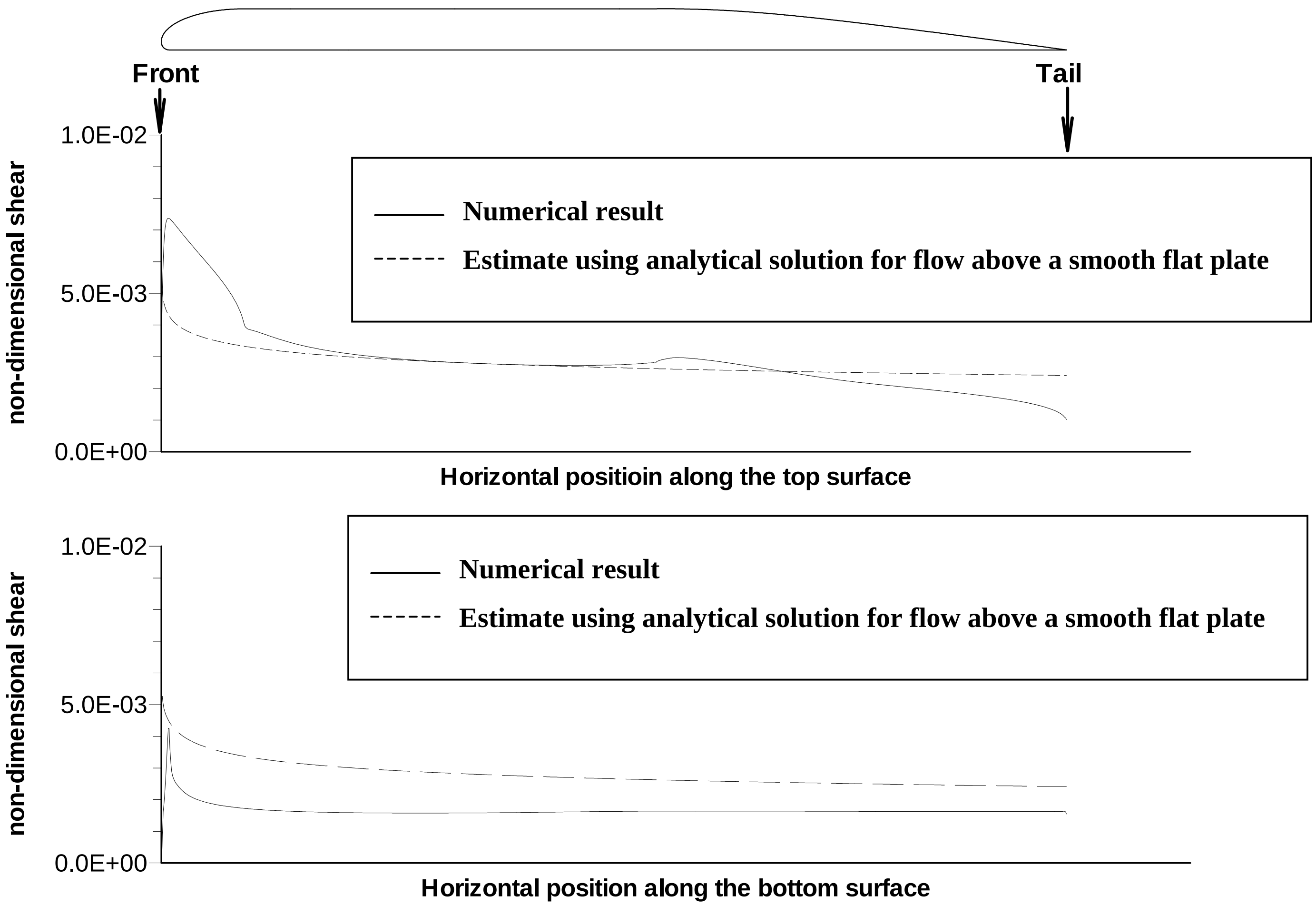

Figure 3.24: Non-dimensional shear stress for Case 5($U = 1 \ m/s$; $h = 0.1 \ m$; $H/w = 0.5$)

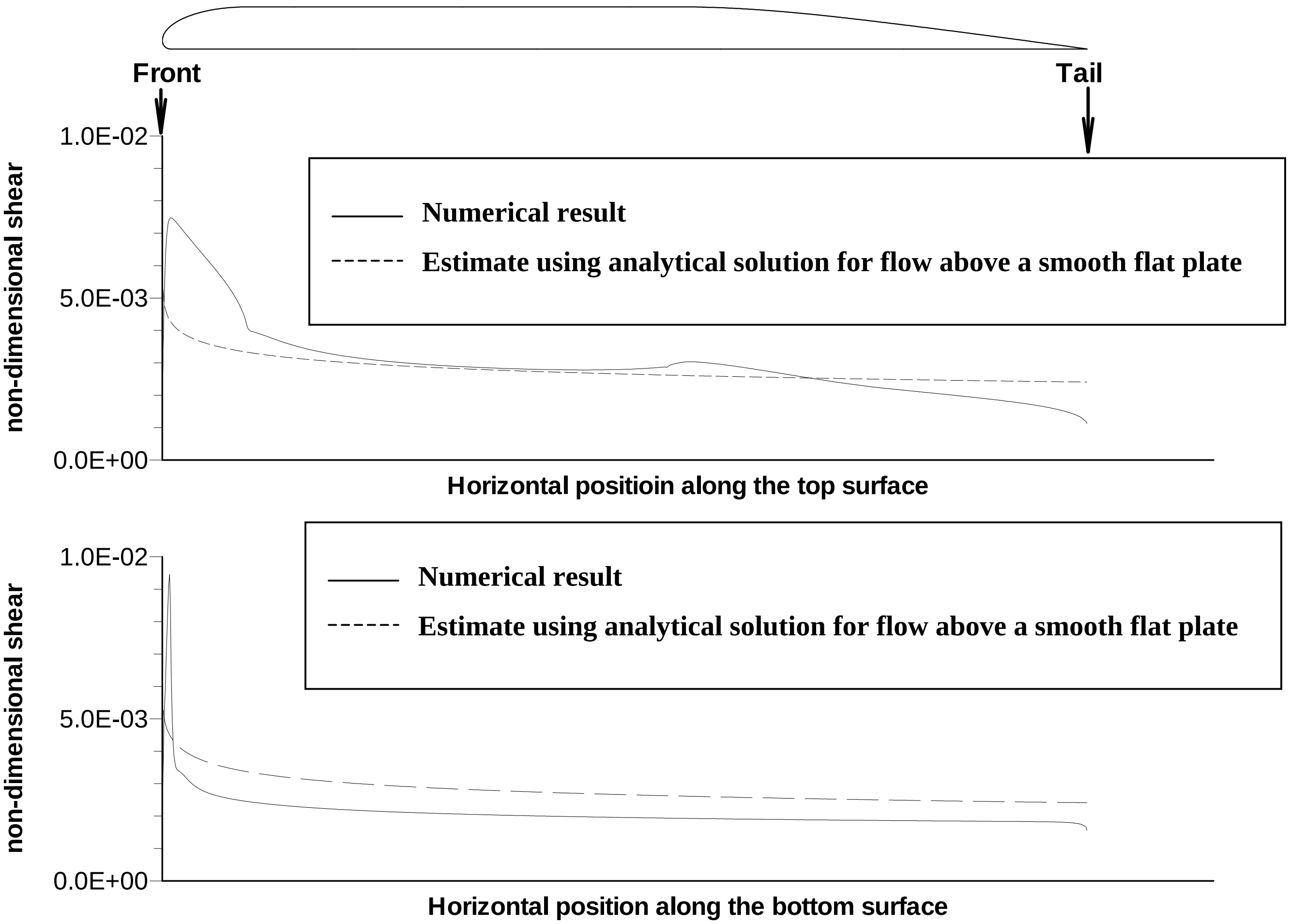

Figure 3.25: Non-dimensional shear stress for Case 6($U = 1 \ m/s$; $h = 1 \ m$; $H/w = 0.5$)

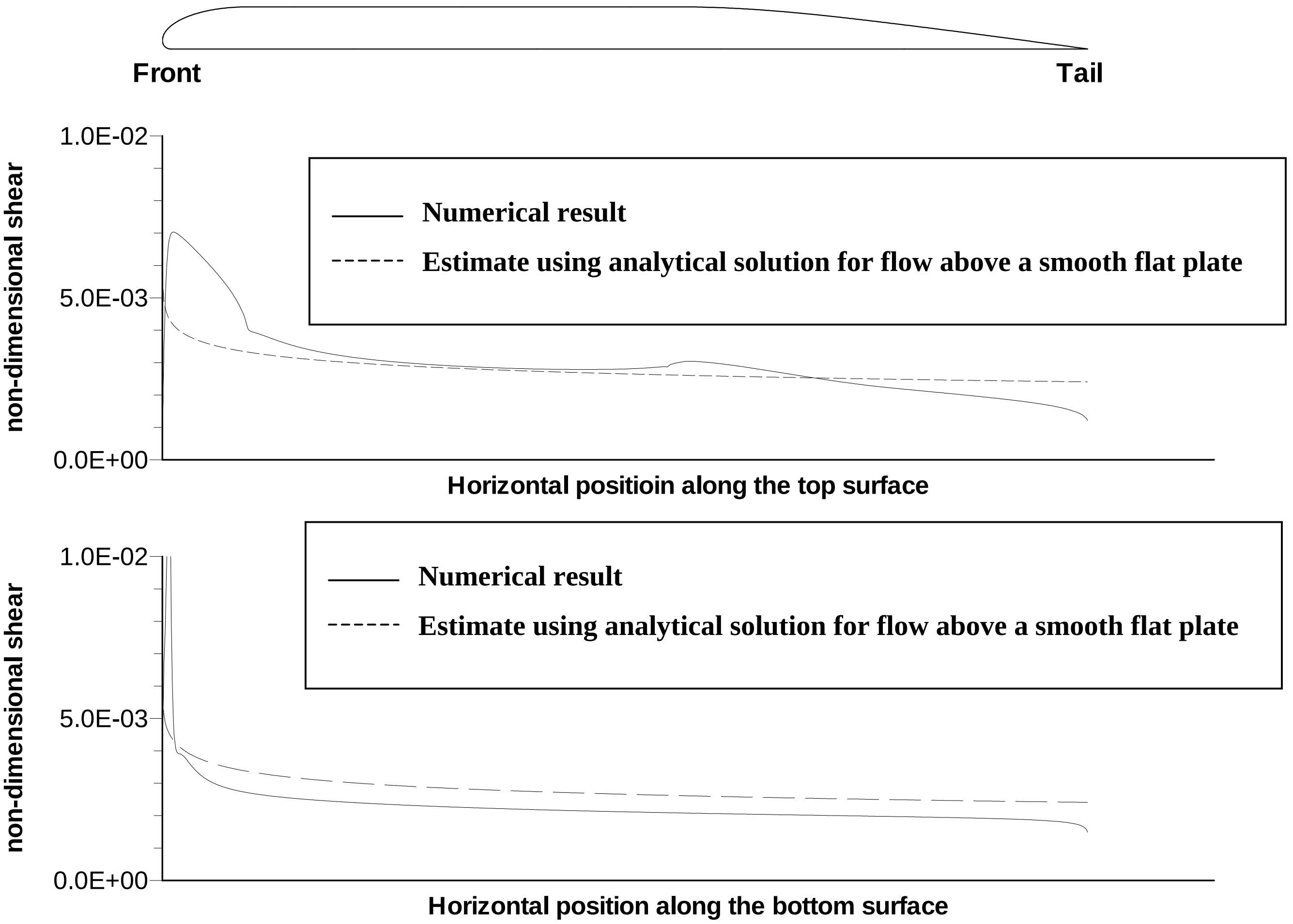

Figure 3.26: Non-dimensional shear stress for Case 7($U = 1 \ m/s$; $h = 10 \ m$; $H/w = 0.5$)

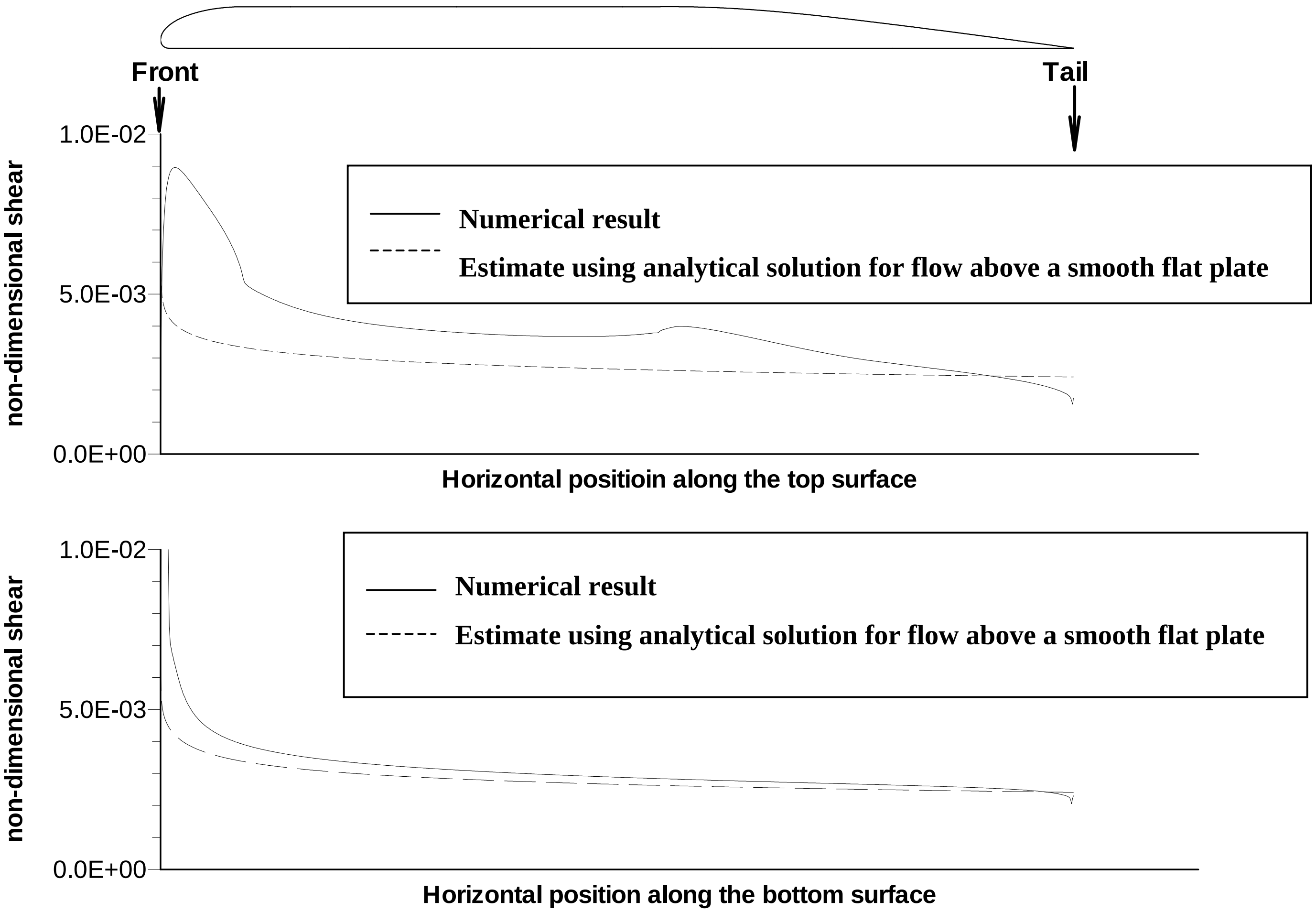

Figure 3.27: Non-dimensional shear stress for Case 8($U = 1 \ m/s$; $h = 50 \ m$; $H/w = 0.5$)

3.3.3.3 Summary on the effect of distance, h, between the bottom surface of the slide mass and underlying ground

As discussed above, a change of distance between the bottom surface of the slide mass and underlying ground h has the following effect on the hydrodynamic stresses:

1. Along the top surface of the slide mass, the non-dimensional kinetic pressures p_t / p_{stag} do not change with the distance h;
2. Along the bottom surface of the slide mass, the non-dimensional kinetic pressures p_b / p_{stag} vary linearly beginning at a point a very short distance behind the front nose of the slide mass and ending at the tail end of the slide mass. The pressures at the beginning and end of the linear distribution vary with the distance, h, and can be estimated by Equations 3.5 and 3.6 for any distance h larger than zero;
3. Along the top and bottom surfaces of the slide mass, the non-dimensional shear stresses τ_t / p_{stag}, τ_b / p_{stag} can be approximated by the analytical solution developed for flow above a smooth flat plate (Equation 3.4) for any distance h larger than zero.

3.3.4 Effect of hydroplaning

In order to study the effect of hydroplaning on the hydrodynamic stresses, Case 9 was analyzed where the slide mass did not hydroplane. For Case 9, the bottom surface of the slide mass is in contact with the underlying ground. The geometry for Case 9 is shown in Figure 3.28. The exposed surfaces of the slide mass and the underlying ground compose the bottom of the flow domain. The boundary conditions are shown in Figure 3.29. The exposed surface of the slide mass is a stationary non-slip wall because the slide mass does not move relative to itself. The exposed surface of the underlying ground is a sliding non-slip wall because the ground moves relative to the slide mass. The mesh for Case 9 is shown in Figure 3.30 and has 553664 rectangular and triangular elements. When the slide mass does not hydroplane, the hydrodynamic stresses are only applied on the exposed surfaces of the slide mass, not on the bottom surface.

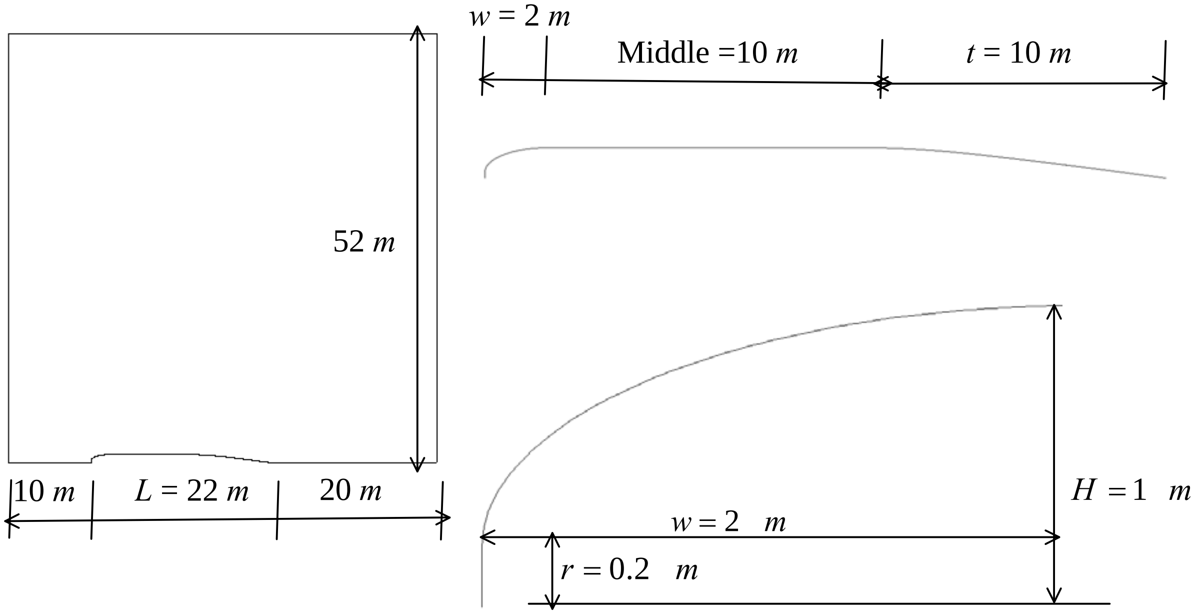

Figure 3.28: Geometry for Case 9($U = 1\ m/s$; $h = 0$; $H/w = 0.5$)

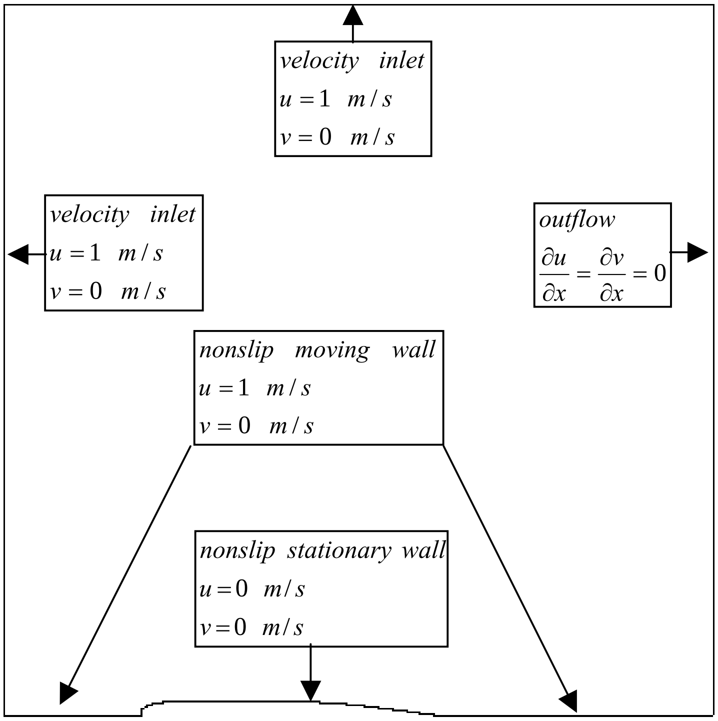

Figure 3.29: Boundary conditions for Case 9($U = 1 \ m/s$; $h = 0$; $H/w = 0.5$)

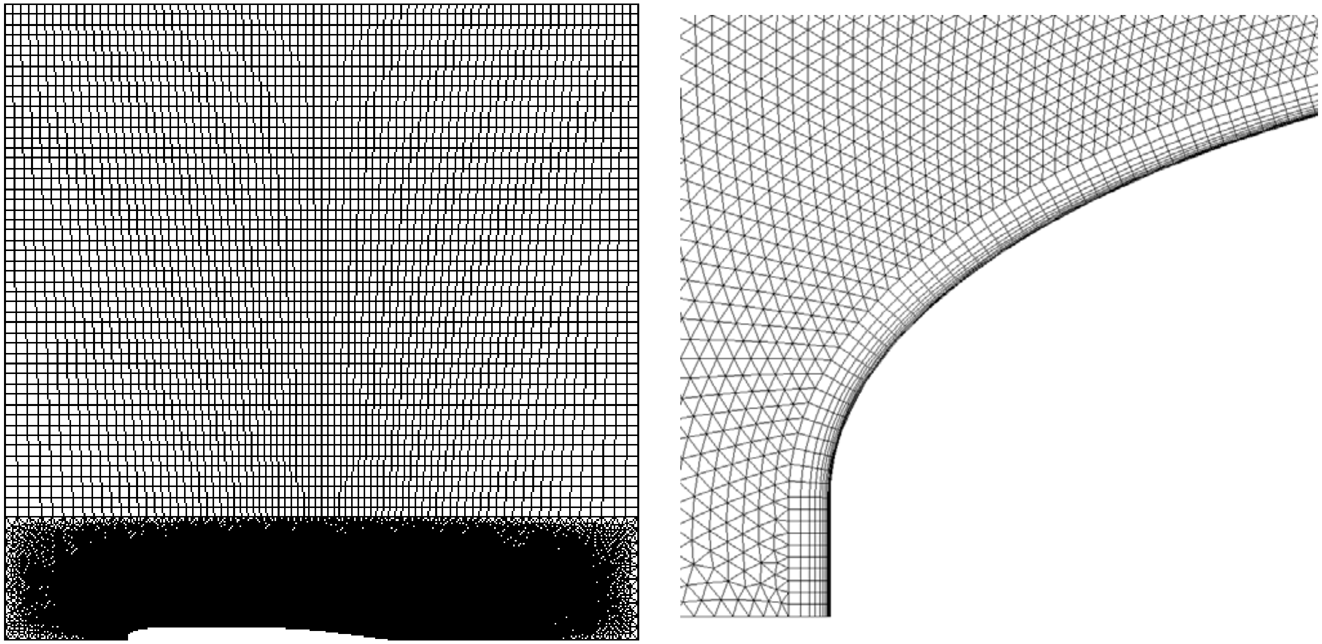

Figure 3.30: Mesh for Case 9($U = 1\ m/s$; $h = 0$; $H/w = 0.5$)

3.3.4.1 Effect of hydroplaning on kinetic pressures

For Case 9, the pressures along the top surface of the slide mass p_t / p_{stag} are plotted in Figure 3.31. For comparison, the pressures along the top surface of the slide mass p_t / p_{stag} for Case 1 are also plotted in Figure 3.31. It can be seen that the pressures p_t / p_{stag} are almost identical. It is hard to distinguish the pressures for Case 1 from those for Case 9. Therefore whether or not hydroplaning occurs has negligible influence on the non-dimensional kinetic pressure, p_t / p_{stag}, along the top surface of the slide mass.

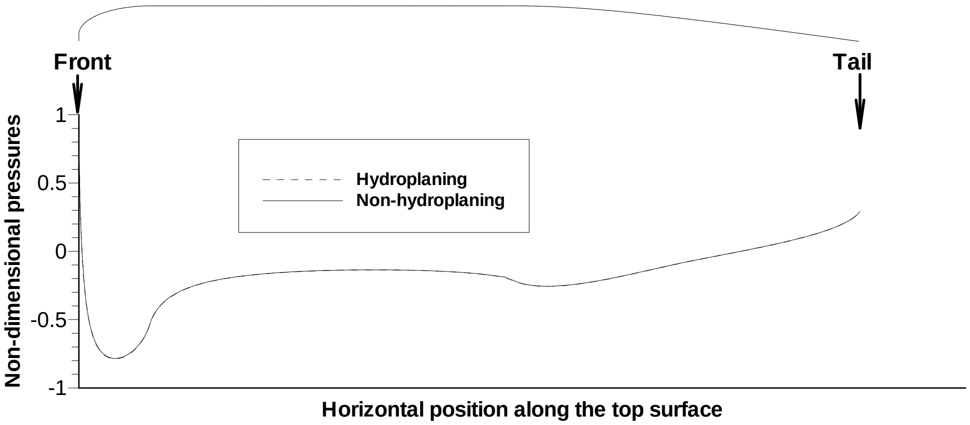

Figure 3.31: Non-dimensional kinetic pressure for Case 9($U = 1 \ m/s$; $h = 0$; $H/w = 0.5$)

3.3.4.2 Effect of hydroplaning on viscous shear stresses

The non-dimensional shear stresses along the top surface of the slide mass τ_t / p_{stag} for Case 9 are shown in Figure 3.32. The computed shear stresses using the analytical solution developed for flow above a smooth flat plate (Equation 3.4) are divided by the stagnation pressure p_{stag} and also plotted in Figure 3.32. It can be seen that the shear stresses calculated using the analytical solution developed for flow above a smooth flat plate (Equation 3.4) are close to the numerical results. Therefore the analytical solution for shear stresses developed for flow above a smooth flat plate provides acceptable approximation for shear stresses on the top surface of the slide mass regardless of whether or not hydroplaning occurs.

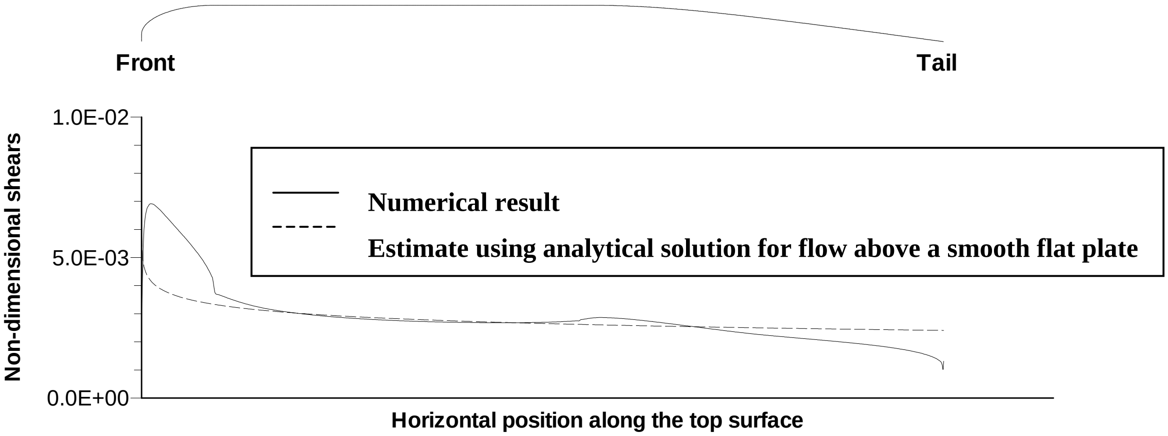

Figure 3.32: Non-dimensional shear for Case 9($U = 1\ m/s$; $h = 0$; $H/w = 0.5$)

3.3.5 Effect of height-to-width ratio of the front portion

To study the influence of the ratio between the height (H) and the width of the front portion (w) of the slide mass, Case 10 was analyzed and compared with Case 9. In both Cases 9 and 10, the slide masses were assumed not to hydroplane ($h = 0$) and the free field velocity U is 1 m/s. The only difference between Cases 9 and 10 is the height-to-width ratio H/w of the front part of the slide mass. The height-to-width ratios (H/w) for Cases 9 and 10 are 0.5 and 2.0 respectively. The front of the slide mass for Case 10 has a more abrupt curvature than that for Case 9. The geometry for Case 10 is shown in Figure 3.33. The mesh for Case 10 is shown in Figure 3.34 and includes 526722 rectangular and triangular elements.

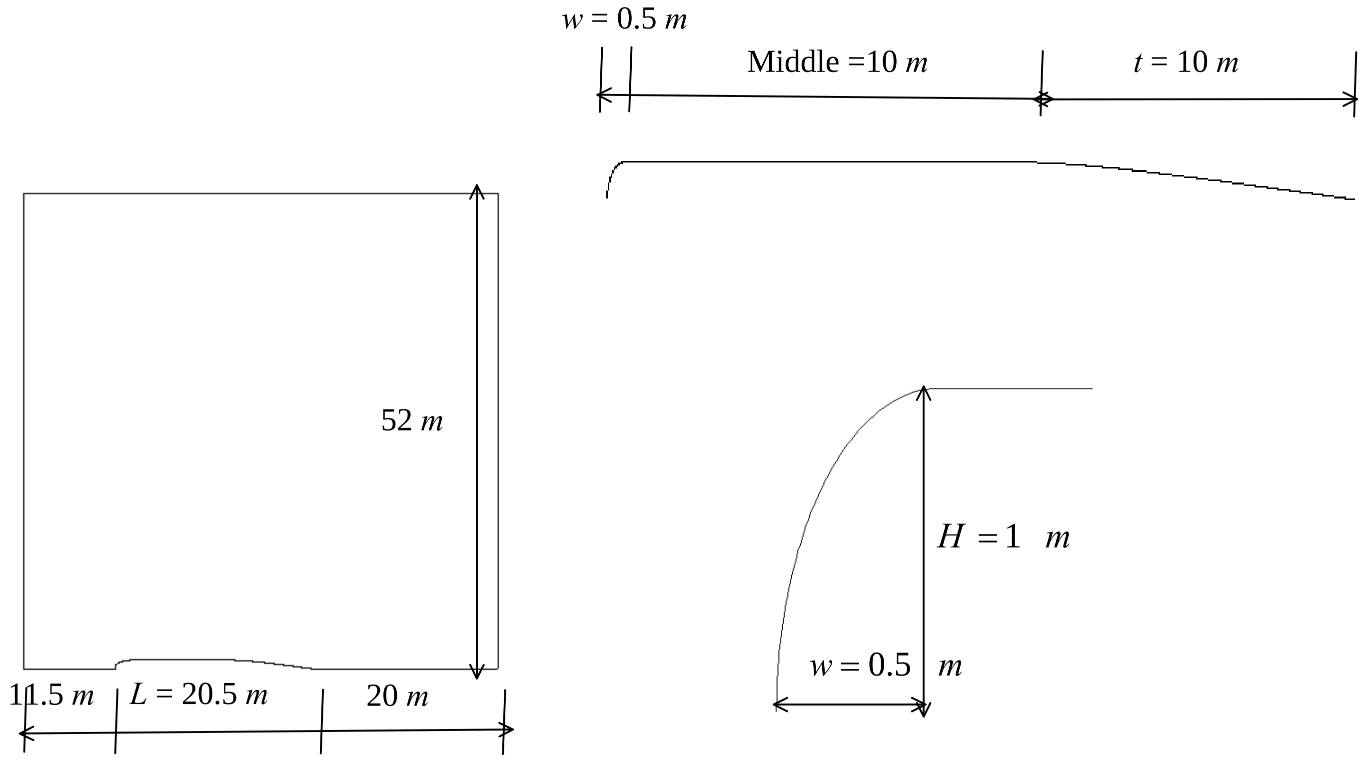

Figure 3.33: Geometry for Case 10($U = 1 \; m/s$; $h = 0$; $H/w = 2.0$)

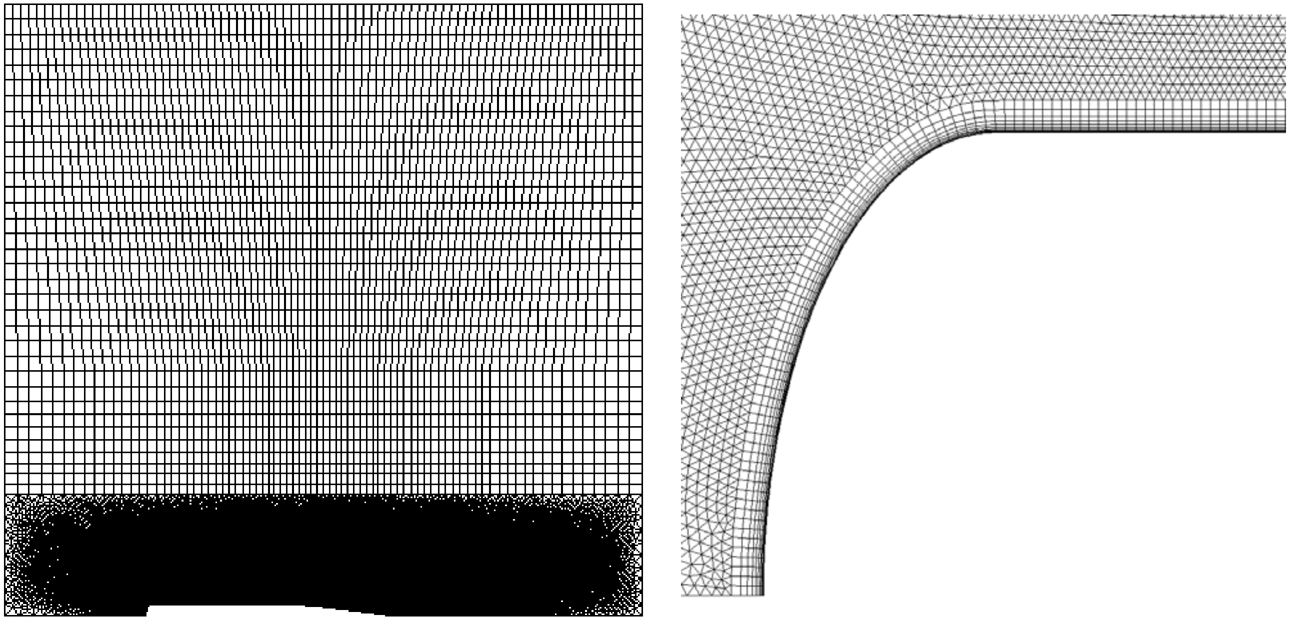

Figure 3.34: Mesh for Case 10($U = 1\ m/s$; $h = 0$; $H/w = 2.0$)

3.3.5.1 Effect of height-to-width ratio H/w on kinetic pressures

The non-dimensional kinetic pressures along the top surfaces of the slide mass p_t / p_{stag} for Cases 9 and 10 are shown in Figure 3.35. The pressures p_t / p_{stag} for both cases are similar along the middle and tail portions of the top surfaces. The non-dimensional pressures p_t / p_{stag} at the front noses of the slide masses are also similar and both equal to 1.0. However, the kinetic pressures p_t / p_{stag} along the front portion of the surfaces (from point I to point J in Figures 3.36 and 3.37) are different. The magnitude of the negative pressures on the slide mass with larger height-to-width ratio ($H/w = 2.0$ for Case 10) is much larger than that with smaller height-to-width ratio ($H/w = 0.5$ for Case 9).

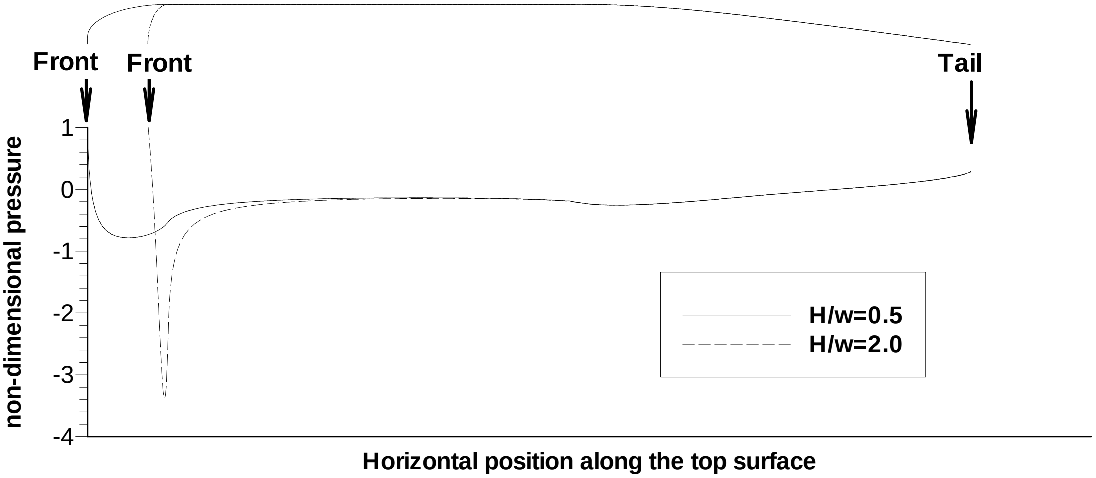

Figure 3.35: Non-dimensional pressures for Case 9 ($U = 1$ m/s; $h = 0$; $H/w = 0.5$) and Case 10 ($U = 1$ m/s; $h = 0$; $H/w = 2.0$)

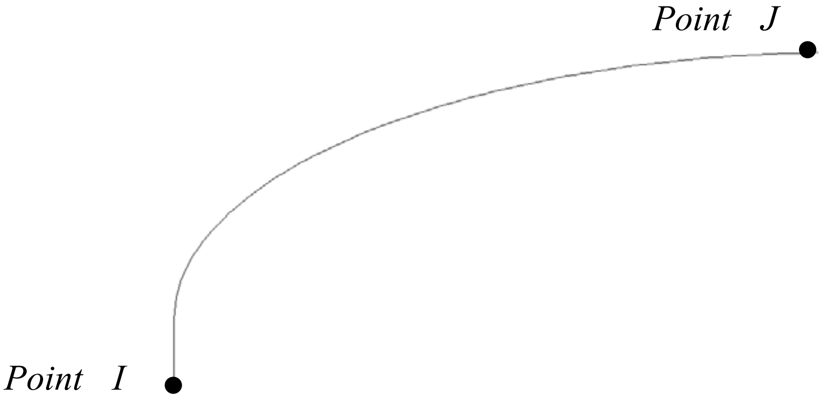

Figure 3.36: Front portion of the surface for Case 9 ($U = 1\ m/s$; $h = 0$; $H/w = 0.5$)

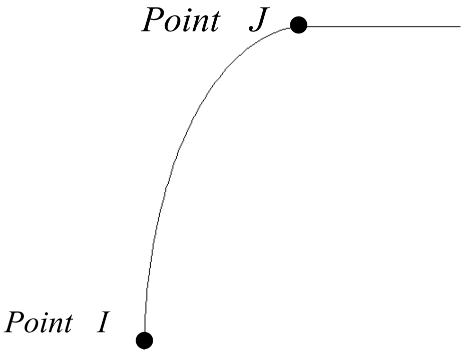

Figure 3.37: Front portion of the surface for Case 10 ($U = 1\ m/s$; $h = 0$; $H/w = 2.0$)

3.3.5.2 Effect of height-to-width ratio H/w on the on-set condition of hydroplaning

In section 3.3.1.2, it was discussed that hydroplaning was expected to happen when the Froude number Fr_d was smaller than $\sqrt{2}$ because of the negative kinetic pressure along the front portion of the surface of the slide mass (the curved portion from point I to point J shown in Figure 3.2 for Case 1, and the curved portions from point I to point J in Figures 3.36 and 3.37 for Cases 9 and 10). In the previous section 3.3.5.1, it was shown that the magnitude of the negative pressures on the slide mass increases as the height-to-width ratio H/w increases. Therefore the critical Froude number $Fr_{d,crit}$ for the on-set of hydroplaning should decrease with the increase of the height-to-width ratio H/w of the slide mass. The effect of height-to-width ratio, H/w, of the slide mass on the on-set condition of hydroplaning will be considered by applying appropriate kinetic pressures on the slide mass as described later in Chapter 4.

3.3.5.3 Effect of height-to-width ratio H/w on viscous shear stresses

The non-dimensional shear stresses along the top surface for Case 10 are shown in Figure 3.38. The shear stresses are also computed using the analytical solution developed for flow above a smooth flat plate (Equation 3.4). After dividing by the stagnation pressure p_{stag}, the shear stresses computed using the analytical solution (Equation 3.4) are also plotted in Figure 3.38. It can be seen that the shear stresses calculated using the analytical solution developed for flow above a smooth flat plate (Equation 3.4) are similar to the shear stresses from the numerical analyses. Therefore the analytical solution for shear stresses for flow above a smooth flat plate provides acceptable approximation for shear stresses on the top surface of the slide mass regardless of the height-to-width ratio, H/w.

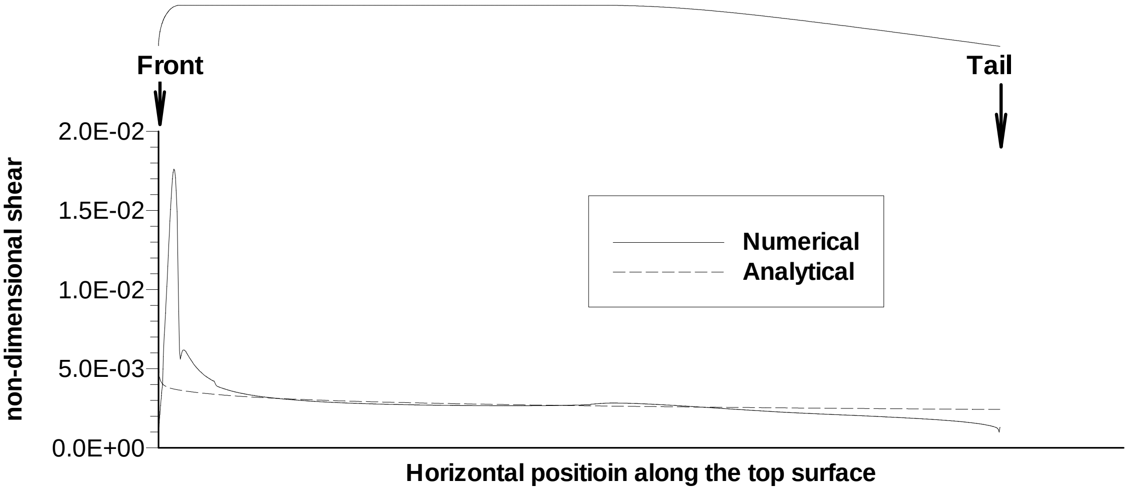

Figure 3.38: Non-dimensional shear for Case 10 ($U = 1$ m/s; $h = 0$; $H/w = 2.0$)

3.3.5.4 Discussions

Although the effect of height-to-width ratio H / w on hydrodynamic stresses was studied for slides that do not hydroplane, the influence of height-to-width ratio H / w for slides that hydroplane is expected to be similar. As concluded in section 3.3.4, whether or not hydroplaning occurs has negligible effect on hydrodynamic stresses along the top surface of the slide mass. Therefore the conclusions about the effect of the height-to-width ratio H / w of the slide mass on hydrodynamic stresses along the top surface of the slide mass drawn in sections 3.3.5.1 and 3.3.5.2 for slide masses that do not hydroplane can be applied to slide masses that hydroplane. Along the bottom of slide masses that hydroplane, the hydrodynamic stresses are determined by the flow between the bottom surface of the slide mass and the underlying ground. This flow and the hydrodynamic stresses along the bottom surface of the slide mass are not significantly affected by the height-to-width ratio H / w of the front portion of the slide mass.

3.4 Conclusions

A numerical model was developed and used to study the flow around a moving slide mass. The study has produced a better understanding of the flow around the slide mass especially of the resulting pressures and shear stresses exerted on the mass. The following conclusions can be drawn from the numerical modeling:

1. When normalized by the stagnation pressure p_{stag}, the non-dimensional kinetic pressures on the surfaces of the slide mass are not influenced by the magnitude of the free field velocity;
2. Along the top surface of the slide mass, hydrodynamic stresses are not influenced by the onset of hydroplaning or the distance between the

underlying ground and the bottom surface of the slide mass that hydroplanes;

3. The kinetic pressures on the middle portion of the top surface of the slide mass are essentially zero for slides in deep water;
4. The non-dimensional kinetic pressures on the tail portion of the top surface of the slide mass increases linearly from zero at the beginning of the tail portion of the slide mass to 0.3 at the end of the slide mass;
5. The kinetic pressure is negative along the frontal portion of the top surface of the slide mass and provides a lift on the slide mass. The magnitude of this negative pressure increases as the height-to-width ratio of the slide mass increases;
6. Along the bottom surface of slide mass that hydroplanes, the non-dimensional kinetic pressures vary linearly beginning at a point a very short distance behind the front nose of the slide mass and extending to the tail end of the slide mass. The pressures at the point a very short distance behind the front nose and at the tail end of the slide mass can be estimated using Equation 3.3;
7. The shear stress along the top and bottom surfaces of the slide mass can be estimated using analytical solution for flow above a smooth flat plate (Equation 3.4);

The negative kinetic pressure along the frontal portion of the top surface of the slide mass explains why a slide mass hydroplanes when the Froude number Fr_d is smaller than $\sqrt{2}$. Also, the change of this negative pressure with the height-to-width ratio of the slide mass suggests that it is not appropriate to use one critical value of Froude number, $Fr_{d,crit}$ to determine whether or not hydroplaning occurs for slide masses with different height-to-width ratios. In order to determine the on-set condition of hydroplaning for any specific slide mass, a block model is developed in the next chapter to simulate the dynamic response of a slide mass and all the above conclusions derived for the hydrodynamic stresses on the slide mass are applied as stress boundary conditions for the block model. In this block model, the hydrodynamic stresses on the surfaces of the block are estimated based on conclusions 1 to 7 and applied as external stresses on the block. Further details of how the stresses are estimated and applied in the block model are discussed in the next chapter.

Chapter 4: Development of Block Model for Subaqueous Slides involving Hydroplaning

A block model was developed to simulate the process of sliding for submarine slides. The results of the numerical modeling of hydrodynamic stresses described in the previous chapter were used to establish the boundary conditions for the block model. The model, including its implementation in a computer code written in the C programming language, is discussed in this chapter. The computer code and a user's guide for the program are also included in Appendix B.

4.1 Governing Equations of Motion

In the block model, the slide mass is represented as a rigid rectangular block which moves and rotates in the plane $x-o-y$ as shown in Figure 4.1. No change in total volume of the slide mass is assumed during the process of sliding because sliding usually lasts no longer than several minutes and the slide mass of interest usually consists of saturated fine-grained silts or clays with very permeability. Thus there is negligible drainage of water into or out of the soil mass during sliding.

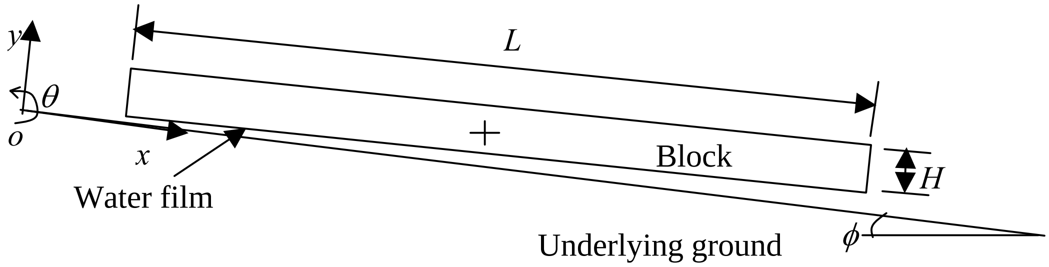

Note: The cross marks the center of the block.

Figure 4.1: Geometry and coordinate system for the block model

Movement of the block involves three degrees of freedom. The block can translate in the x and y directions and rotate in the $x-o-y$ plane. The translations of the center of the block (marked by a cross in Figure 4.1) and the rotation of the block relative to the center are computed from the following governing equations:

$$\ddot{x} = \frac{F_x}{M} \tag{4.1}$$

$$\ddot{y} = \frac{F_y}{M} \tag{4.2}$$

$$\ddot{\theta} = \frac{T}{I} \tag{4.3}$$

where $\ddot{x}$, $\ddot{y}$ are the accelerations in the x and y directions; F_x, F_y are the total external forces on the block in the x and y directions; $\ddot{\theta}$ is the angular acceleration in the $x-o-y$ plane and T is the total external torque about the center of the block in the θ direction. The quantity, M, in Equations (4.1) and (4.2) represents the mass of the block and can be calculated as:

$$M = \rho_s HL \tag{4.4}$$

The quantity I in Equation (4.3) is the moment of inertia about the center of the block and can be calculated as:

$$I = \frac{1}{12}\rho_s HL\left(H^2 + L^2\right) \tag{4.5}$$

where ρ_s is the total mass density of the soil, H is the height of the block and L is the length of the block.

4.2 Occurrence of Hydroplaning

The occurrence of hydroplaning depends on the contact condition between the bottom surface of the block and the underlying ground. In order to determine the contact condition, a height of roughness h_r at the interface between the block and underlying ground is compared with the displacement of the block in the y direction along the bottom surface.

The height of roughness, h_r, is determined by the size of soil particles in the slide mass and the surface property of the underlying ground. For underlying ground consisting of soil, the height of roughness h_r is assumed to be equal to d_{95}, of the soil at the interface between the block and underlying ground, where d_{95} is the size of grains at which 95% of the soil is finer than.

The displacement of the block in the y direction may vary in the x direction. At the front and tail ends of the block, the displacements are designated as h_f and h_t respectively as shown in Figure 4.2. The displacements h_f and h_t can be calculated as:

$$h_f = y_o + \Delta y - \frac{1}{2}H + \frac{1}{2}L\sin\theta \tag{4.6}$$

$$h_t = y_o + \Delta y - \frac{1}{2}H - \frac{1}{2}L\sin\theta \tag{4.7}$$

where y_o is the initial y coordinate of the center of the block, Δy is the displacement of the center of the block in the y direction, H is the height of the block, L is the length of the block and θ is the angle between the bottom of the block and underlying ground.

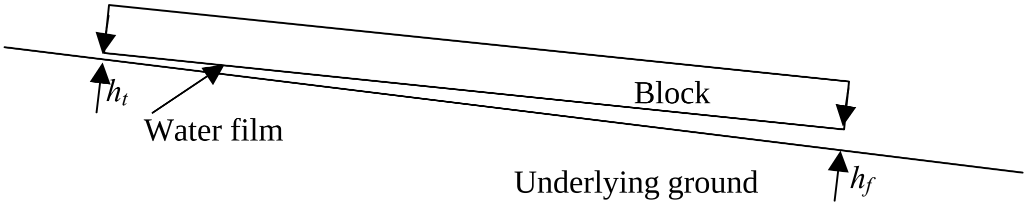

Figure 4.2: Distance between the block and underlying ground

Three possible contact conditions are considered based on a comparison of the displacements h_f, h_t and the height of roughness h_r as follows:

1) No hydroplaning: The bottom surface of the block is in contact with the underlying ground everywhere, i.e.

   $$h_f \le h_r \quad and \quad h_t \le h_r \tag{4.8}$$

2) Partial hydroplaning: Part of the bottom surface is in contact with the ground and the other part is not, i.e.

   $$\min(h_f, h_t) < h_r < \max(h_f, h_t) \tag{4.9}$$

3) Complete hydroplaning: No part of the bottom surface of the block is in contact with the ground surface, i.e.

   $$h_f \ge h_r \quad and \quad h_t \ge h_r \tag{4.10}$$

The forces applied on the bottom surface of the block change with the occurrence of hydroplaning. The forces on the bottom of the block for the above three conditions are discussed in the following section.

4.3 Forces on Block

The external forces on the block are considered to be represented by the submerged weight of the block, reactive forces applied on the bottom of the block by the underlying ground, and the hydrodynamic stresses applied on the surfaces of the block by the surrounding fluid. The potential stresses and forces on the block are summarized in Table 4.1 and also illustrated in Figure 4.3. The stresses and forces on the block are discussed as in the sections below.

Table 4.1: Possible stresses on the block

Stress	Symbol	No Hydroplaning	Partial Hydroplaning	Complete Hydroplaning
Effective gravitational force at the center of the block	G'	Applied		
Kinetic pressure on the leading edge	p_u	Applied		
Kinetic pressure on the tail surface	p_d	Applied		
Kinetic pressure on the top surface	p_t	Applied		
Kinetic pressure on the bottom surface (pore water pressure on the bottom surface) due to movement down slope	p_b	Applied as pore water pressure	Applied as kinetic pressure	Applied as kinetic pressure
Kinetic damping force	$\tilde{N}_w$	Not applied	Applied	Applied
Kinetic damping moment	M_w	Not applied	Applied	Applied
Viscous shear along the leading edge	τ_u	Applied		
Viscous shear along the tail surface	τ_d	Applied		
Viscous shear along the top surface	τ_t	Applied		
Viscous shear along the bottom surface	τ_b	Not applied	Not applied	Applied
Effective support on the bottom surface applied by the ground surface	N'_{bu}, N'_{bd}	Applied		
Damping force applied by the ground surface	D_{sd}, D_{su}	Applied		
Friction on the bottom surface	c	Applied	Not applied	Not applied

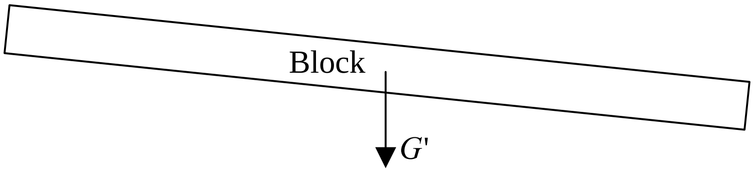

(a) Effective weight of the block

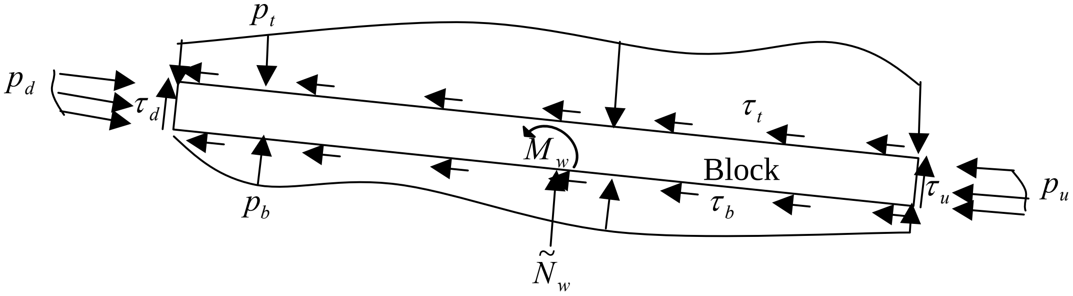

(b) Forces applied by the surrounding fluid

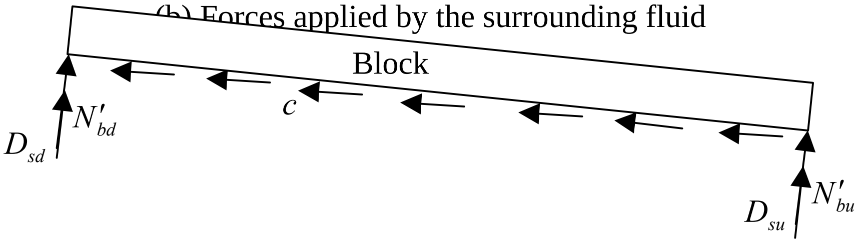

(c) Forces applied by the ground surface

Figure 4.3: Forces on the block

4.3.1 Submerged weight

The submerged weight of the block G' is calculated as:

$$G' = (\rho_s - \rho_w)gHL \tag{4.11}$$

where ρ_s is the total density of soil, ρ_w is the density of water, g is the acceleration of gravity, H is the height of the block and L is the length of the block. The force due to the effective weight G' acts through the centroid of the block as shown in Figure 4.3a.

4.3.2 Kinetic pressure

The surrounding fluid exerts hydrodynamic stresses on the surface of the block when the block moves. There are two types of hydrodynamic stresses: kinetic pressure and viscous shear. The kinetic pressures caused by the motion of the block in the x direction include pressures on all four surfaces of the block, p_u, p_d, p_t and p_b as shown in Figure 4.3b. These kinetic pressures are determined based on the numerical modeling of flow around a sliding mass that was discussed in the previous chapter. In order to better explain the kinetic pressures, a local reference system $r-s$ as shown in Figure 4.4 is used. The symbols s and r are the local coordinates along the surfaces of the block. The kinetic pressures on each surface of the block are discussed in the sections below.

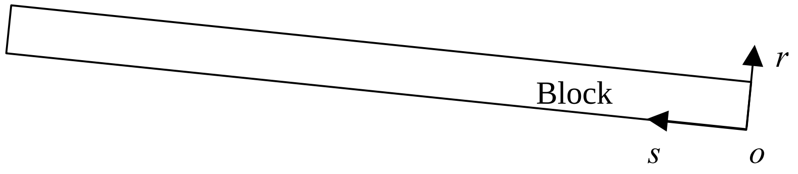

Figure 4.4: Local coordinate system for the block model

4.3.2.1 Along the leading edge

The kinetic pressure, p_u, on the leading edge of the block (Figure 4.3b) varies linearly from the stagnation pressure $\frac{1}{2}\rho_w V_x^2$ at $r=0$ to zero at $r=\alpha H$, where α is the "head ratio" of the block. The head ratio is defined as the ratio of block's height at the front to the average height of the block H. The head ratio α is a non-dimensional constant and is used to consider the effect of the frontal shape on the kinetic pressure p_u. The kinetic pressure p_u can be calculated as:

$$p_u = \frac{1}{2}\rho_w V_x^2 \left(1 - \frac{r}{\alpha H}\right) \tag{4.12}$$

where ρ_w is the density of water, V_x is the velocity of the block in the x direction, r is the local coordinate along the front surface of the block and H is the height of the block.

4.3.2.2 Along the trailing edge

The kinetic pressure, p_d, along the trailing surface of the block (Figure 4.3b) is assumed to vary linearly in the r direction from zero at $r = H$ to $0.3p_{stag}$ at $r = 0$. The kinetic pressure p_d is calculated as:

$$p_d = 0.3\left(\frac{1}{2}\rho_w V_x{}^2\right)\left(1 - \frac{r}{H}\right) \tag{4.13}$$

4.3.2.3 Along the top surface

The kinetic pressure, p_t, along the top surface of the block (Figure 4.3b) is assumed to vary linearly over three separate ranges. The distribution of kinetic pressure p_t is shown in Figure 4.5. Over the first range, the kinetic pressure p_t varies linearly from zero at $s = 0$ to $\lambda \frac{1}{2}\rho_w V_x^2$ at $s = \frac{1}{2}\beta H$. Over the second range, the kinetic pressure p_t varies linearly from $\lambda \frac{1}{2}\rho_w V_x^2$ at $s = \frac{1}{2}\beta H$ to zero at $s = \beta H$. Over the third range, , the kinetic pressure p_t is zero from $s = \beta H$ to $s = L$. The constant β is the ratio of the length along the top surface of the block where negative kinetic pressure is applied to the height of the block. The constant λ represents the lowest pressure along the top surface of the sliding block normalized by the stagnation pressure. The kinetic pressure p_t is, thus, calculated as:

$$p_t = \begin{cases} \lambda \frac{1}{2}\rho_w V_x^2 \frac{s}{0.5\beta H} & 0 \le s \le \frac{1}{2}\beta H \\ \lambda \frac{1}{2}\rho_w V_x^2 \left(2 - \frac{s}{0.5\beta H}\right) & \frac{1}{2}\beta H \le s \le \beta H \\ 0 & \beta H \le s \le L \end{cases} \tag{4.14}$$

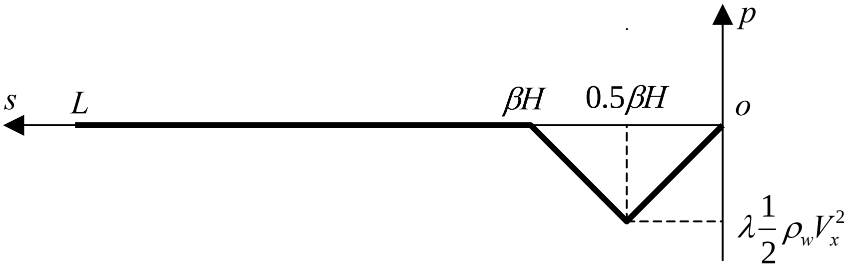

Figure 4.5: The distribution of pressure p_t along the top surface of the block

4.3.2.4 Along the bottom surface

The pressure, p_b, along the bottom surface of the block depends on the following three possible conditions:

1) <u>No hydroplaning</u>: Excess pore water pressure is assumed to be applied along the bottom surface. The pressure p_b is also assumed to be uniform and can be calculated as:

$$p_b = \frac{1}{2}\rho_w V_x^{\ 2} \tag{4.15}$$

where ρ_w is the density of water, V_x is the velocity of the block in the x direction;

2) Partial hydroplaning: Excess pore water pressure is assumed to be applied on the non-hydroplaning portion of the bottom surface and the kinetic pressure is applied on the hydroplaning portion of the bottom surface. The bottom pressure, p_b, is assumed to be uniform and can be calculated as:

$$p_b = \begin{cases} \frac{1}{2}\rho_w V_x^{2}\left[\frac{1}{1+2.57\left(\frac{h_f}{H}\right)^{0.58}}\right] & for \quad h_f \geq h_t \\ \frac{1}{2}\rho_w V_x^{2}\left[\frac{0.3}{1+0.15\left(\frac{h_t}{H}\right)^{0.4}}\right] & for \quad h_f \leq h_t \end{cases} \tag{4.16}$$

3) Complete hydroplaning: Kinetic pressure, p_b, is applied on the entire bottom surface of the block and can be calculated as:

$$p_b = \frac{1}{2}\rho_w V_x^{2} \times \left\{\left[\frac{1}{1+2.57\left(\frac{h_f}{H}\right)^{0.58}}\right]\left(1-\frac{s}{L}\right)+\left[\frac{0.3}{1+0.15\left(\frac{h_t}{H}\right)^{0.4}}\right]\left(\frac{s}{L}\right)\right\} \tag{4.17}$$

4.3.3 Viscous shear stresses

The viscous shears caused by the motion of the block in the x direction are expressed by τ_u, τ_d, τ_t and τ_b as shown in Figure 4.3b. Shear stresses, τ_u and τ_d, along the leading and trailing (front and tail) surfaces of the block, respectivel, are neglected. The shear stress along the bottom of the slide mass τ_b is only applied when complete hydroplaning occurs as discussed in section 4.2. Along the top and bottom surfaces of the block, shear stress τ_t and τ_b are estimated by the theory for a turbulent boundary layer along a flat plate as

$$\tau_t = \tau_b = \frac{1}{2}\rho_w V_x{}^2 \left(\frac{0.027}{\left(\frac{V_x s}{\upsilon} \right)^{1/7}} \right) \tag{4.18}$$

where υ is the kinematic viscosity of water. More details about the theory for turbulent boundary layers can be found in Crowe, et al. (2000).

4.3.4 Forces by underlying ground

There are two types of forces applied on the bottom surface of the block by the underlying ground, i.e. the normal support and resistance. The two types of forces are discussed in the following sections.

4.3.4.1 Support by underlying ground

When the block is in contact with the underlying ground, a positive effective normal stress may be applied at the bottom surface of the block by the underlying ground. For simplicity, the forces due to the effective normal stresses are simulated by two springs. The springs are assumed to produce the same total normal force and moment as produced by the normal stresses in the soil distributed along the bottom of the block. As shown in Figure 4.6, the two springs connect the lower corners of the block to the underlying ground. The forces produced by the springs on the block are designed as N'_{bu} and N'_{bd} respectively for the front and trailing corners.

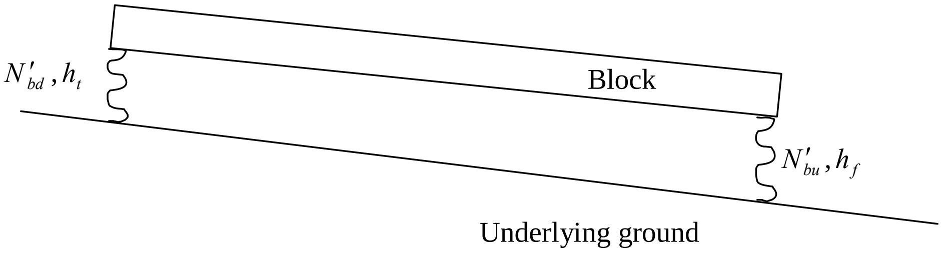

Figure 4.6: Springs between the block and underlying ground

The forces N'_{bu} and N'_{bd} depend on the displacements of the block at the front and trailing corners h_f and h_t respectively. The force-displacement curve of the springs ($N'_{bu} - h_f$ and $N'_{bd} - h_t$) is shown in Figure 4.7.

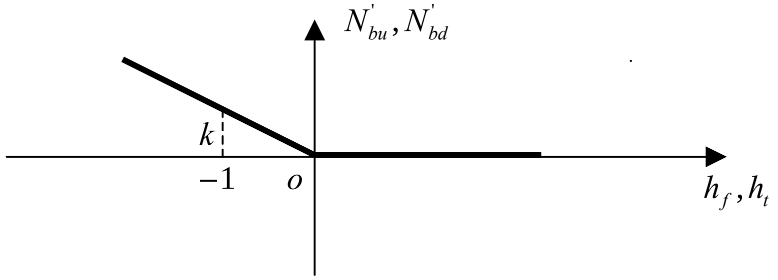

Figure 4.7: Force-displacement curve of the springs

As shown in Figure 4.7, the tensile strength of the springs is zero. When compressed, the springs are linearly elastic. The forces applied by the springs N'_{bu} and N'_{bd} are zero when displacements h_f and h_t are positive. When the displacements h_f and h_t are negative, the forces N'_{bu} and N'_{bd} can be calculated as:

$$N'_{bu} = \begin{cases} 0 & h_f \geq 0 \\ -kh_f & h_f < 0 \end{cases} \tag{4.19}$$

$$N'_{bd} = \begin{cases} 0 & h_t \geq 0 \\ -kh_t & h_t < 0 \end{cases} \tag{4.20}$$

where k is a spring constant. The constant k is determined based on the settlement at the center of a flexible rectangular footing on the surface of an elastic ground (Das, 1999) as follows:

$$k = \frac{E}{1-\nu^2}\frac{1}{10} \tag{4.21}$$

Where E is the modulus of elasticity and ν is the Poisson's ratio for the underlying soil. The parameters E and ν are parameters defined in terms of effective stresses of the soil.

4.3.4.2 Resistance by underlying ground

For no hydroplaning condition, a shear stress is applied on the bottom surface of the block by the underlying ground. The shear stress is assumed to be equal to the un-drained shear strength (c) of soil at the interface. For partial and complete hydroplaning conditions, it is assumed that no shear stress is applied on the block by the underlying ground. The un-drained shear strength c is calculated as

$$c = \tau_y + \mu_s \frac{\dot{x}}{\left(\frac{H}{2}\right)} \tag{4.22}$$

where τ_y is the static shear strength of soil corresponding to infinitely low strain rate, $\dot{x}$ is the slide velocity of the block, H is the height of the block and μ_s is the strain rate factor for soil. The second term in Equation 4.22 represents the influence of strain rate on the shear strength of soil c. The strain rate at the bottom surface of the block is assumed to be $\dot{x}/\left(\frac{H}{2}\right)$.

4.3.5 Damping effects

Two types of damping effects are considered in the block model. One is referred to as kinetic damping which is applied by the surrounding water. The other is soil damping which is applied by the underlying ground. The damping forces are discussed as follows.

4.3.5.1 Water damping

Water damping is produced by the hydrodynamic stresses caused by the block's motion in the y direction and rotation in the $x-o-y$ plane. These hydrodynamic stresses are shown in Figure 4.8. Compared to the kinetic pressure along the bottom surface of the block $\tilde{p}_b$, the other hydrodynamic stresses are negligible. The kinetic pressure $\tilde{p}_b$ is only applied after the block reaches the complete hydroplaning condition.

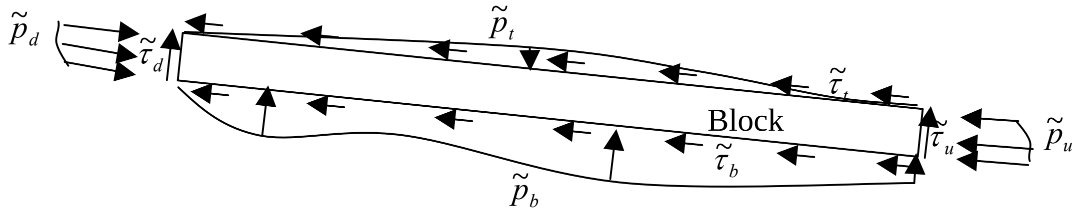

Figure 4.8: Hydrodynamic stresses producing kinetic damping effect

When the bottom surface of the block is parallel to the underlying ground, i.e. $h_f = h_t$ and $\theta = 0$, the kinetic pressure $\tilde{p}_b$ can be estimated analytically. According to the analytical solution for squeeze film lubrication (Panton, 1984), the kinetic pressure $\tilde{p}_b$ can be expressed as:

$$\tilde{p}_b = \begin{cases} 6\dfrac{\mu L^2}{h_f^3}\dot{y}\left[\dfrac{s}{L}\left(\dfrac{s}{L}-1\right)\right] = 6\dfrac{\mu L^2}{h_t^3}\dot{y}\left[\dfrac{s}{L}\left(\dfrac{s}{L}-1\right)\right] & \mathit{for} \quad h_f = h_t > h_r \\ 6\dfrac{\mu L^2}{h_r^3}\dot{y}\left[\dfrac{s}{L}\left(\dfrac{s}{L}-1\right)\right] & \mathit{for} \quad h_f = h_t \le h_r \end{cases} \tag{4.23}$$

The distribution of kinetic pressure $\tilde{p}_b$ is plotted in Figure 4.9. As shown in Figure 4.9, the pressure $\tilde{p}_b$ is symmetric about the midpoint of the bottom surface ($x = L/2$). The peak value of pressure $\tilde{p}_b$ is $-\dfrac{3}{2}\dfrac{\mu L^3}{\max(h_f, h_r)^3}\dot{y}$ at the midpoint of the bottom surface, i.e. $x = L/2$. The integration of pressure $\tilde{p}_b$ along the bottom surface of the block yields the total normal force on the bottom surface $\tilde{N}_w$ as:

$$\tilde{N}_w = \int_0^L \tilde{p}_b ds = \begin{cases} \int_0^L 6\dfrac{\mu L^2}{h_f^3}\dot{y}\left[\dfrac{s}{L}\left(\dfrac{s}{L}-1\right)\right]ds & for \quad h_f = h_t > h_r \\ \int_0^L 6\dfrac{\mu L^2}{h_r^3}\dot{y}\left[\dfrac{s}{L}\left(\dfrac{s}{L}-1\right)\right]ds & for \quad h_f = h_t \le h_r \end{cases}$$

$$= \begin{cases} -\dfrac{\mu L^3}{h_f^3}\dot{y} = -\dfrac{\mu L^3}{h_t^3}\dot{y} & for \quad h_f = h_t > h_r \\ -\dfrac{\mu L^3}{h_r^3}\dot{y} & for \quad h_f = h_t \le h_r \end{cases} \tag{4.24}$$

The moment M_w about the center of the block produced by the kinetic pressure $\tilde{p}_b$ is zero.

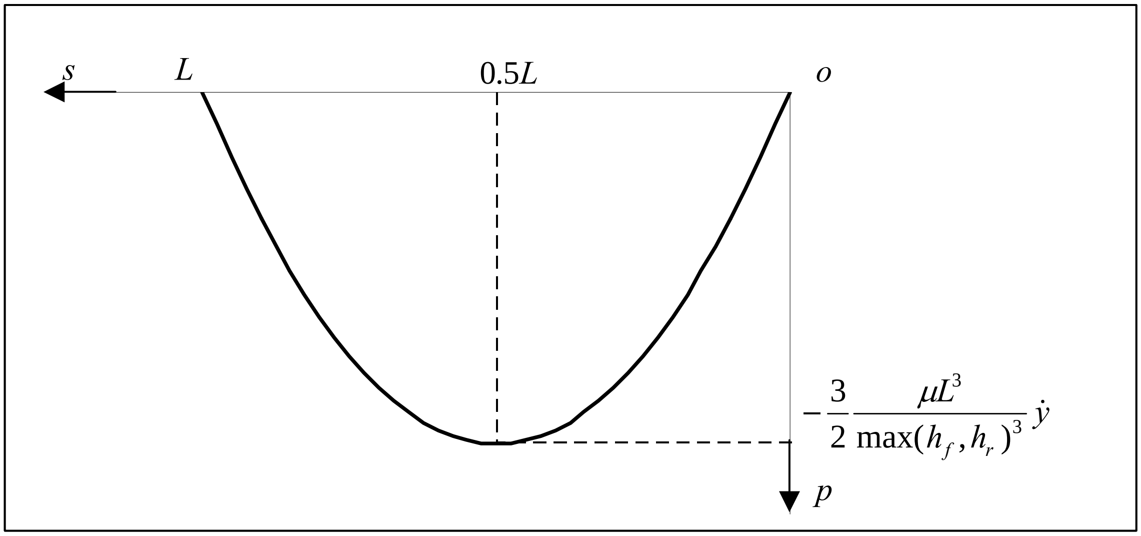

Figure 4.9: Kinetic pressure $\tilde{p}_b$ for $h_f = h_t$ and $\theta = 0$

When the bottom surface of the block is not parallel to the underlying ground, i.e. $h_f \neq h_t$ and $\theta \neq 0$, the total normal force $\tilde{N}_w$ and the moment M_w are approximated by using the average value of the displacements, h_f and h_t, at the leading and trailing ends of the block. The force $\tilde{N}_w$ and the moment M_w are assumed to be:

$$\tilde{N}_w = \begin{cases} -\dfrac{\mu L^3}{\left(0.5*(h_f + h_t)\right)^3}\dot{y} & for \quad 0.5*(h_f + h_t) > h_r \\ \\ -\dfrac{\mu L^3}{h_r^3}\dot{y} & for \quad 0.5*(h_f + h_t) \le h_r \end{cases} \tag{4.25}$$

$$M_w = \begin{cases} -\dfrac{\mu}{0.5*(h_f + h_t)^3}\dot{\theta}L^5 \sin(\theta) & for \quad 0.5*(h_f + h_t) > h_r \\ \\ -\dfrac{\mu}{h_r^3}\dot{\theta}L^5 \sin(\theta) & for \quad 0.5*(h_f + h_t) \le h_r \end{cases} \tag{4.26}$$

It can be seen that Equation 4.26 yields a moment M_w of zero when the bottom surface of the block is parallel to the underlying ground ($\theta = 0$).

4.3.6.2 Soil damping

When the block is in contact with the underlying ground, the kinetic energy of the block dissipates into the underlying ground by wave propagation. To simulate the effect of energy dissipation, soil damping forces D_{sd} and D_{su} are applied on the lower corners of the block as shown in Figure 4.2c. When the downstream corner of the block is not in contact with the underlying ground, i.e. $h_t > 0$, the force D_{sd} is zero. When the downstream corner of the block is in contact with the underlying ground, i.e. $h_t \le 0$, the force D_{sd} is estimated by Equation 4.27. Similarly, the force D_{su} is calculated by Equation 4.28.

$$D_{sd} = \begin{cases} 0 & for \quad h_t > 0 \\ \\ -\dfrac{1}{4}L\dfrac{\sqrt{\rho_g G}}{1-\nu}(\dot{y} - 0.5L\cos\dot{\theta}) & for \quad h_t \le 0 \end{cases} \tag{4.27}$$

$$D_{su} = \begin{cases} 0 & for \quad h_f > 0 \\ -\frac{1}{4} L \frac{\sqrt{\rho_g G}}{1-\nu}(\dot{y} + 0.5L\cos\dot{\theta}) & for \quad h_f \le 0 \end{cases} \tag{4.28}$$

Where ρ_g is the total density of soil in the underlying ground, and G is the shear modulus of the underlying soil. Equations 4.27 and 4.28 are based on the analytic solutions for the dynamic response of footings on elastic ground. More details can be found in Richart, et. al. (1970).

4.4 Time Integration Scheme

The sliding process of the block is disretisized into a step-by-step phenomenon using a Newmark scheme (Newmark, 1959). The initial conditions, and the updating method between two immediate steps are discussed as follows.

4.4.1 Initial conditions

At the beginning, i.e., $t = 0$, the coordinate $x(0)$, velocities $\dot{y}(0)$ and $\dot{\theta}(0)$ of the block are assumed to be zero. The initial velocity $\dot{x}(0)$ is specified as an input parameter. The block is also assumed to be at static rest along the y and θ directions before any kinetic forces are applied. By equating the component of the effective weight (G') along y direction with the support of the underlying ground ($N_{bu}^{'}$ and $N_{bd}^{'}$), the initial coordinate $y(0)$ of the block is computed. By setting the resultant moment of the support ($N_{bu}^{'}$ and $N_{bd}^{'}$) and resistance ($c \cdot L$) by underlying ground to be zero, the initial coordinate $\theta(0)$ of the block is computed. The dynamic equilibrium of the block is then solved for to compute the initial accelerations $\ddot{x}(0)$, $\ddot{y}(0)$ and $\ddot{\theta}(0)$.

4.4.2 Newmark scheme

During any increment of time, the accelerations of the block are assumed to be constant and equal to the average value of the accelerations at the beginning and end of the time increment. For any time step, the variables including accelerations ($\ddot{x}(t)$, $\ddot{y}(t)$, $\ddot{\theta}(t)$), velocities ($\dot{x}(t)$, $\dot{y}(t)$, $\dot{\theta}(t)$) and coordinates ($x(t)$, $y(t)$, $\theta(t)$) at the beginning ($time = t$) are given. An iterative method is used to compute the variables, $\ddot{x}(t+\Delta t)$, $\ddot{y}(t+\Delta t)$, $\ddot{\theta}(t+\Delta t)$, $\dot{x}(t+\Delta t)$, $\dot{y}(t+\Delta t)$, $\dot{\theta}(t+\Delta t)$, $x(t+\Delta t)$, $y(t+\Delta t)$, and $\theta(t+\Delta t)$ at the end of the time increment ($time = t+\Delta t$).

For the first iteration, the accelerations at the end of the increment are assumed to be equal to those at the beginning, i.e.

$$\ddot{x}(t+\Delta t) = \ddot{x}(t) \tag{4.29}$$

$$\ddot{y}(t+\Delta t) = \ddot{y}(t) \tag{4.30}$$

$$\ddot{\theta}(t+\Delta t) = \ddot{\theta}(t) \tag{4.31}$$

For each iteration, the following steps are conducted:

1. The average accelerations during the increment, velocities and displacements at the end of the increment are calculated as follows:

$$\ddot{x}_{(from \quad t \quad to \quad t+\Delta t)} = 0.5*\left(\ddot{x}(t) + \ddot{x}(t+\Delta t)\right) \tag{4.32}$$

$$\ddot{y}_{(from \quad t \quad to \quad t+\Delta t)} = 0.5*\left(\ddot{y}(t) + \ddot{y}(t+\Delta t)\right) \tag{4.33}$$

$$\ddot{\theta}_{(from \quad t \quad to \quad t+\Delta t)} = 0.5*\left(\ddot{\theta}(t) + \ddot{\theta}(t+\Delta t)\right) \tag{4.34}$$

$$\dot{x}(t+\Delta t) = \dot{x}(t) + \ddot{x}_{(from \quad t \quad to \quad t+\Delta t)}\Delta t \tag{4.35}$$

$$\dot{y}(t+\Delta t) = \dot{y}(t) + \ddot{y}_{(from \quad t \quad to \quad t+\Delta t)}\Delta t \tag{4.36}$$

$$\dot{\theta}(t+\Delta t) = \dot{\theta}(t) + \ddot{\theta}_{(from \quad t \quad to \quad t+\Delta t)}\Delta t \tag{4.37}$$

$$x(t+\Delta t) = x(t) + \dot{x}(t)\Delta t + \frac{1}{2}\ddot{x}_{(from \quad t \quad to \quad t+\Delta t)}\Delta t^2 \tag{4.38}$$

$$y(t+\Delta t) = y(t) + \dot{y}(t)\Delta t + \frac{1}{2}\ddot{y}_{(from \quad t \quad to \quad t+\Delta t)}\Delta t^2 \tag{4.39}$$

$$\theta(t+\Delta t)=\theta(t)+\dot{\theta}(t)\Delta t+\frac{1}{2}\ddot{\theta}_{(from \quad t \quad to \quad t+\Delta t)}\Delta t^{2} \tag{4.40}$$

2. The forces on the block at the end of the increment are calculated from Equations 4.11 to 4.28 using the displacement and velocity calculated by Equations 4.35 to 4.40.
3. The dynamic equilibrium of the block is solved for using Equations 4.1 to 4.5 to compute the accelerations at the end of the increment ($\ddot{x}(t+\Delta t)$, $\ddot{y}(t+\Delta t)$ and $\ddot{\theta}(t+\Delta t)$).
4. The newly computed accelerations, $\ddot{x}(t+\Delta t)_{new}$, $\ddot{y}(t+\Delta t)_{new}$, $\ddot{\theta}(t+\Delta t)_{new}$ and the accelerations used in step 1, $\ddot{x}(t+\Delta t)$, $\ddot{y}(t+\Delta t)$ $\ddot{\theta}(t+\Delta t)$) are used to compute the numerical error for the iteration as follows:

$$error=\max\left(\left|\frac{\ddot{x}(t+\Delta t)_{new}-\ddot{x}(t+\Delta t)}{\ddot{x}(t+\Delta t)}\right|,\left|\frac{\ddot{y}(t+\Delta t)_{new}-\ddot{y}(t+\Delta t)}{\ddot{y}(t+\Delta t)}\right|,\left|\frac{\ddot{\theta}(t+\Delta t)_{new}-\ddot{\theta}(t+\Delta t)}{\ddot{\theta}(t+\Delta t)}\right|\right) \tag{4.41}$$

5. If the error is not acceptably small, the newly computed accelerations are substituted into Equations 4.32 to 4.40 to start another iteration; Steps 1-5 are repeated until the error is acceptably small.

After the iterations are completed, the next time step is considered. The newly computed variables, $\ddot{x}(t+\Delta t)$, $\ddot{y}(t+\Delta t)$, $\ddot{\theta}(t+\Delta t)$, $\dot{x}(t+\Delta t)$, $\dot{y}(t+\Delta t)$, $\dot{\theta}(t+\Delta t)$, $x(t+\Delta t)$, $y(t+\Delta t)$ and $\theta(t+\Delta t)$ from the last step are used as starting conditions, $\ddot{x}(t)$, $\ddot{y}(t)$, $\ddot{\theta}(t)$), ($\dot{x}(t)$, $\dot{y}(t)$, $\dot{\theta}(t)$, $x(t)$, $y(t)$ and $\theta(t)$ for the new step. The iterative method discussed above is then repeated to compute the variables at the end of the new time step.

4.5 Implementation

The scheme of the block model is implemented in a computer code programmed in the C programming language. The program is named rect1.cpp. Details of the program and a user's guide are included in Appendix B.

4.6 Summary

In this chapter, a block model has been developed for the dynamic response of submarine slides. The occurrence of hydroplaning was simulated by monitoring and comparing the displacement of the block in the direction normal to the underlying ground with the height of roughness h_r at the interface between the block and underlying ground. The effective weight of the block, the kinetic pressures and viscous shears by surrounding fluid, the support and resistance by underlying ground, and the forces due to kinetic and soil damping effects were considered in the block model. The influence of hydroplaning was also accounted for by making the forces on the block compatible with the contact condition between the block and underlying ground. The sliding process of the block was disretisized into a step-by-step phenomenon using Newmark scheme. At the beginning of the sliding precess, i.e., $t = 0$, the block is assumed to be at static rest along the y and θ directions before any kinetic forces are applied. The initial velocity of the block, $\dot{x}(0)$, is specified as an input parameter. The block model has been implemented by programming in the C programming language. In order to validate the block model, it is compared with the laboratory experiments by Mohrig, et al. (1999) as discussed in the next chapter.

Chapter 5: Validation of the Block Model

In this chapter, results computed with the block model are compared with the results of laboratory experiments by Mohrig et al. (1999). The conditions of Mohrig, et al.'s experiments are first summarized and the input parameters for the block model are discussed. Results from the block model are then compared with the experimental data. The occurrence of hydroplaning of the slide mass is also examined.

5.1 Experimental Conditions

Mohrig, et al. (1999) performed laboratory experiments on subaqueous slides. In their experiments, they released soil from a large box into a channel with transparent sides. The box from which soil was released was at the upper end of the channel and had a slot 20 mm high and 170 mm wide. The channel was approximately 10 m long, 3 m deep and 20 cm wide. The channel was segmented with a break in slope, the upper and lower slope angles being 6 and 1 degrees, respectively. The break in slope was located approximately 5.7 m downslope from the position where the soil was released. The bottom surface of the channel was a rubber mat which was crenelated into rectangular ridges and grooves in the transverse direction. The width of each ridge and groove was approximately 6.4 mm, and the depth of the grooves was approximately 3.2 mm.

In each experiment, approximately 30 liters of soil were released. The total time to release the soil was about 3.5 s. The properties of the soil are summarized in Table 5.1. The water content of the soil was 63.9%. The soil consisted of a mixture of 40% kaolin, 40% silt and 20% sand by dry weight. The total density of the soil, ρ_s, was approximately 1.6 t/m^3. The static shear strength of the soil τ_y varied from 33 to 49 Pa. Considering the effect of strain rate, the shear strength, c, was calculated as follows:

$$c = \tau_y + \mu_s \dot{\gamma} \tag{5.1}$$

Where μ_s is a constant and $\dot{\gamma}$ is shear strain rate. The constant μ_s varied from 0.019 to 0.035 $kg \cdot m^{-1}s^{-1}$. A grain-size analysis was conducted on the soil and d_{95} was determined to be 0.7 mm.

Table 5.1: Properties of soil used by Mohrig, et al. (1999)

Run	Bottom surface of channle	Static shear strength τ_y (Pa)	Factor of strain rate μ_s $(kg \cdot m^{-1}s^{-1})$	Height of the slide mass H (mm)
1w	Clean	49	0.035	18
2w	Clean	49	0.035	18
3w	Clean	36	0.023	16
4w	Soil	49	0.035	6.5
5w	Soil	33	0.019	16

Mohrig, et al performed five experiments referred to as Runs 1w to 5w. For Runs 1w to 3w, the bottom surface of the channel was clean when the soil was released. For Runs 4w and 5w, a layer of soil was placed on the bottom of the upper 6 degree slope of the channel (extending approximately 5.7 m downslope from the position where the soil was released). For all five runs, the heights of the slide masses H were measured and are listed in Table 5.1. The velocities, U, of the front of the slide mass were reported as functions of run-out distances, x, and are plotted in Figure 5.1.

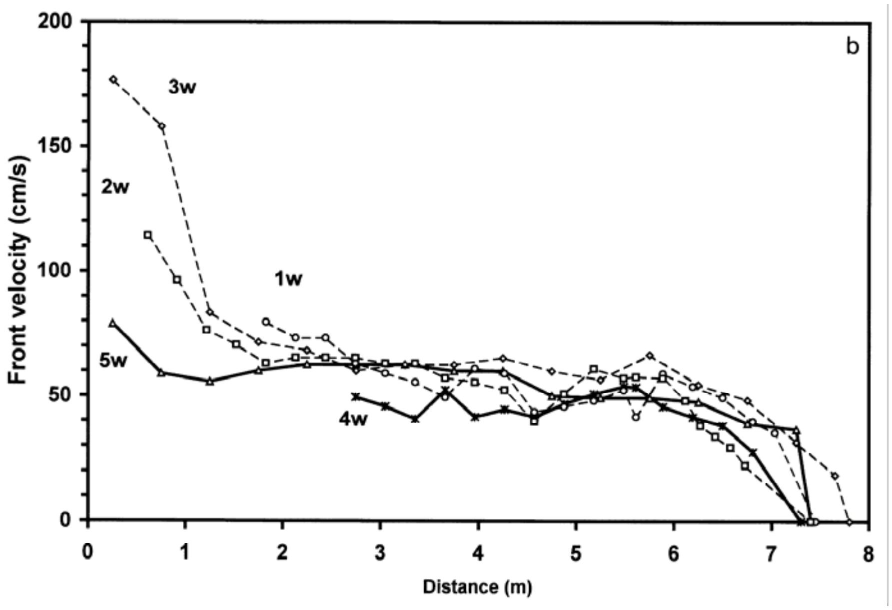

Figure 5.1: Reported front velocity vs run-out distance (Mohrig, et al. (1999))

5.2 Input Parameters

The input parameters used for the block model were based on data reported by Mohrig, et al. (1999). All the parameters and their values are listed in Table 5.2. The values of some parameters were determined directly according to the conditions of Mohrig, et al's experiments. The values of other parameters were determined by trial and error. All the parameters and the methods used to determine their values are discussed in the following sections.

Table 5.2: Input parameters and their values for block model

Run	3w	1w	2w	4w	5w
Slope angle δ	6° for the first 5.7m downslope, and 1° for the rest				
Head ratio α	2				
Non-dimensional constant λ	-5				
Non-dimensional constant β	0.5				
The modulus of elasticity for the underlying ground E (kpa)	8000				
Poisson's ratio for the underlying ground ν	0.4				
Density of soil $\rho_s\,(kg/m^3)$	1600				
Height of roughness h_r (mm)	3.2	3.2	3.2	0.7	0.7
Static shear strength τ_y (Pa)	36	49	49	49	33
Factor of strain rate $\mu_s\,(kg \cdot m^{-1} s^{-1})$	2.3E-02	3.5E-02	3.5E-02	3.5E-02	1.9E-02
Height of the block H (m)	1.6E-02	1.8E-02	1.8E-02	6.5E-03	1.6E-02
Initial velocity (m/s)	1.85	1.00	1.20	0.60	0.80
Dynamic viscosity of surrounding fluid $\mu\,(kg \cdot m^{-1} s^{-1})$	1.15E-02	1.75E-02	1.75E-02	1.75E-02	9.5E-03
Time increment Δt (s)	1.0E-04	1.0E-04	1.0E-04	1.0E-05	1.0E-05
Block length L (m)	0.46	0.52	0.52	0.17	0.46

5.2.1 Parameters determined directly

The height of roughness h_r was assumed to be equal to the depth of the grooves (3.2 mm) when the bottom surface of the channel was clean. When the bottom of the channel was covered by soil, the height of roughness h_r was assumed to be equal to d_{95} of the soil (0.7 mm). The head ratio α of the block and the non-dimensional constant β are assumed to be 2.0 and 0.5, respectively, based on the frontal shape of the sliding mass as shown in Figure 5.2. The height-to-width ratio of the front portion of the slide mass is approximately 3.0 as shown in Figure 5.2. The non-dimensional constant λ is assumed to be -5 based on the distribution of kinetic pressure on the top surface of the slide mass with a height-to-width ratio of 2.0 as shown in Figure 3.35. The modulus of elasticity for the underlying ground E and the Poisson's ratio for the underlying ground ν are based on general properties for loose sandy silt reported by Das (1999). The static shear strength τ_y and factor of strain rate μ_s of soil are reported by Mohrig, et al and listed in Table 5.1. Considering the mixing of soil and surrounding fluid, the viscosity of the surrounding fluid μ was taken as the average value of the factor of strain rate of the soil μ_s (between 0.019 to 0.035 $kg \cdot m^{-1} s^{-1}$) and the viscosity of pure water (0.001 $kg \cdot m^{-1} s^{-1}$). The height of the block H was reported by Mohrig et al. and also listed in Table 5.1. The initial velocity of the block is based on the data shown in Figure 5.1. The plot of front velocity versus run-out distance was extrapolated to estimate an initial front velocity at a run-out distance of zero. As an example, the extrapolation of front velocity versus run-out distance for Run 3w is shown in Figure 5.3. The estimated front velocity is assumed to be the initial velocity of the block.

Figure 5.2: Frontal shape of the sliding soil mass (Mohrig, et al. 1999)

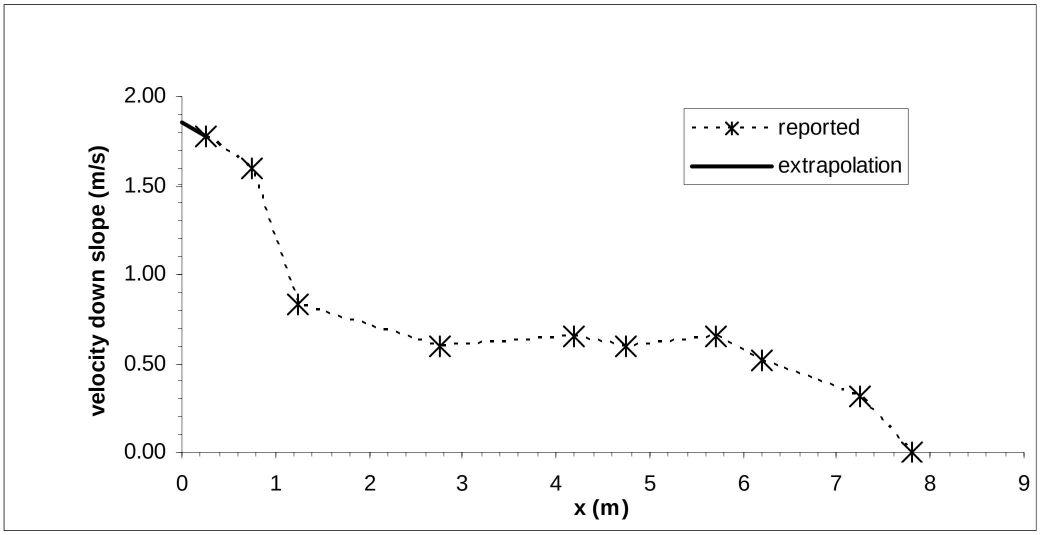

Figure 5.3: Extrapolation of the front velocity versus run-out distance for Run 3w

5.2.2 Parameters determined by trial and error

The length of the sliding block, L, was also determined by trial and error. For every experiment, the length of the slide mass was zero at the beginning of the experiment, but increased as the soil moved down the channel. At the end of the experiment, the length of the slid mass was essentially equal to the run-out distance. However, in the block model, the length of the block was assumed to be constant. In order to determine the appropriate length, L, of the block for the experiment, it was assumed that the length-to-height ratios of the block L/H were the same for all five experiments. As shown in Figure 5.1, over run-out distances smaller than 2 meters, more data points were reported for Run 3w than most of the other runs. Thus, Run 3w was analyzed as a representative case to find an optimum length-to-height ratio L/H which was then used for all runs. Five values for length-to-height ratio L/H were tried. The length-to-height ratios and corresponding lengths of the block are listed in Table 5.3. The computed front velocities versus run-out distances are shown in Figure 5.4. The reported velocities versus run-out distances for Run 3w are also shown in Figure 5.4. It can be seen that when the length of the block L is 0.46 m (length-to-height ratio L/H is 28.75), the numerical results fit the reported experimental values well. Therefore a length-to-height ratio L/H of 28.75 was assumed for all the runs. The lengths of the block L calculated based on the length-to-height ratio L/H as 28.75 for all the runs are listed in Table 5.2.

Table 5.3: Trial for length-to-height ratio L/H

Length-to-height ratio L/H	25.000	26.875	28.750	30.625	32.500
Length of the Block L (m)	0.40	0.43	0.46	0.49	0.52

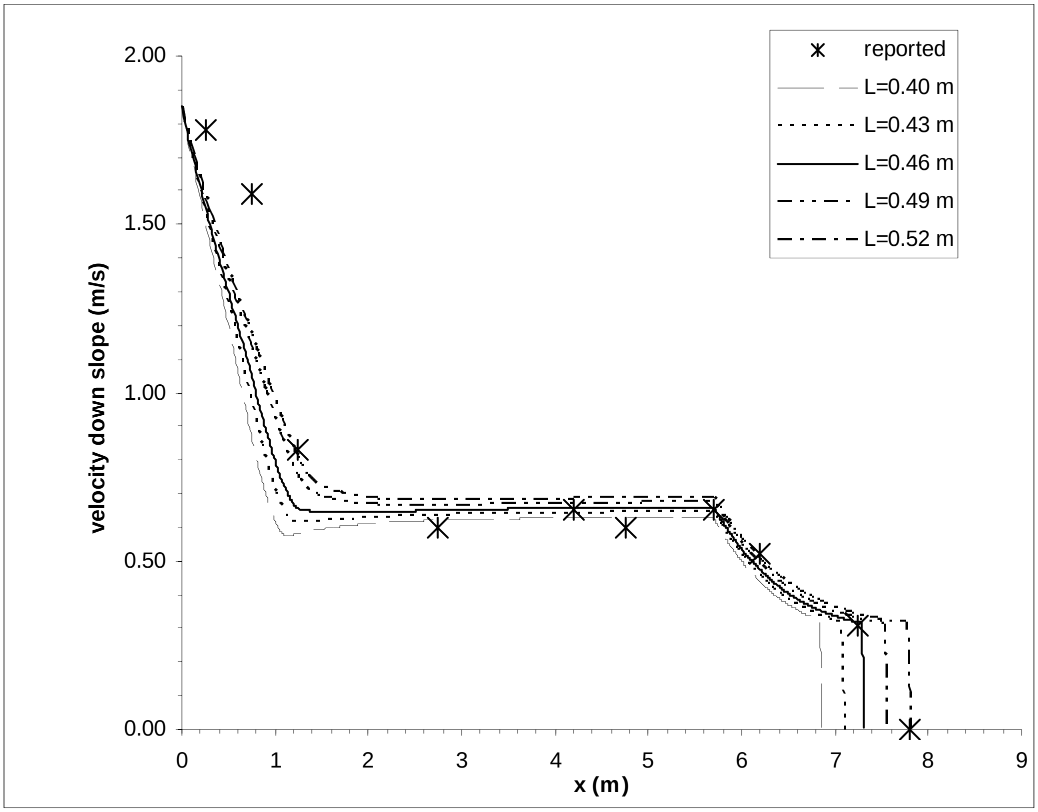

Figure 5.4: Front velocity vs run-out distance for Run 3w

The increment of time Δt used in the computations with the block model was determined by trial and error. Three values for Δt of 0.001 s, 0.0001 s and 0.00001 s were tried. For Run 3w, the numerical results using $\Delta t = 0.0001 \ s$ and $\Delta t = 0.00001 \ s$ are shown together in Figure 5.5. It can be seen that the difference in numerical results using different increments of time Δt is negligible. Using Δt of 0.0001 s was, thus, assumed to be sufficient. Similary, using Δt of 0.0001 s was found to be sufficient for Runs 1w and 2w. For Runs 4w and 5w, a smaller Δt of 0.00001 s was found to be sufficient.

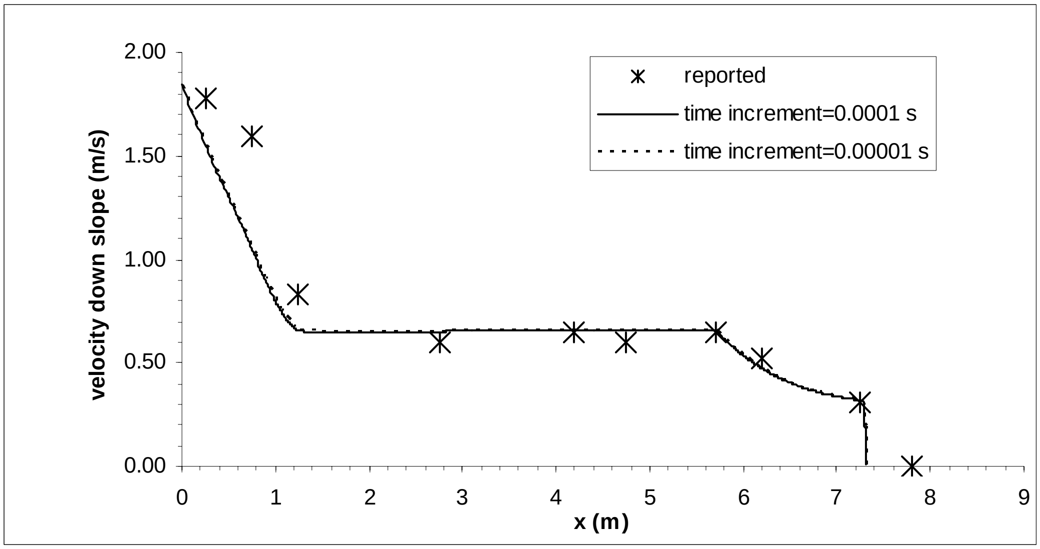

Figure 5.5: Numerical results for Run 3w using $\Delta t = 0.0001\ s$ and $\Delta t = 0.00001\ s$

5.3 Comparison of Numerical Results with Experimental Data

Mohrig, et al. reported the front velocities versus run-out distances for the five tests. They also observed that hydroplaning occurred in all five of the tests. The calculated front velocities versus run-out distances are compared with the experimental data in this section. Also the occurrence of hydroplaning predicted by the block model is discussed in this section.

5.3.1 Front velocity versus run-out distance

The calculated and measured front velocities versus run-out distances for Run 3w were shown previously in Figure 5.4. The calculated front velocities versus run-out distances for runs 1w, 2w, 4w and 5w are shown in Figures 5.6 to 5.9 together with the reported data. It can be seen that the numerical results agree favorably with the experimental data for Runs 1w, 2w, 3w, and 4w. For Run 5w, the block model predicted longer final run-out distance than the experimental measurements.

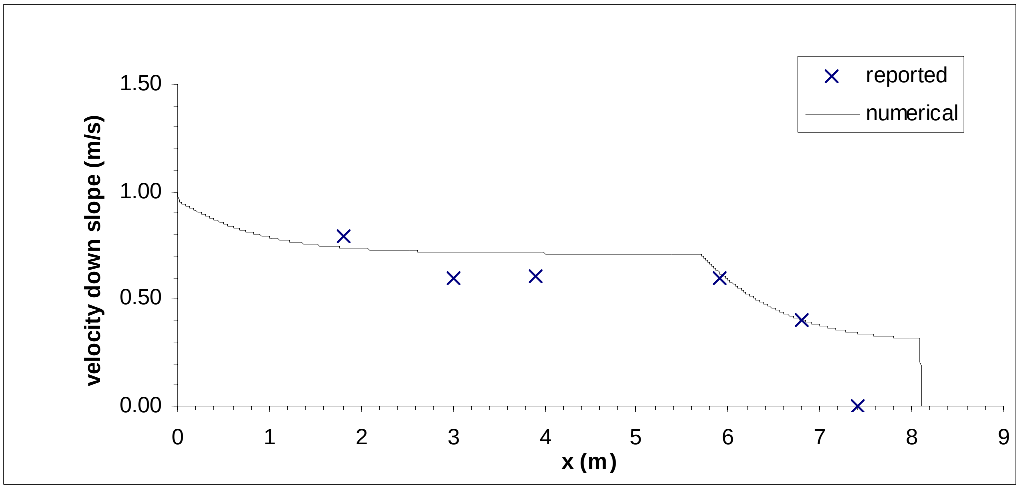

Figure 5.6: Front velocity versus run-out distance for Run 1w

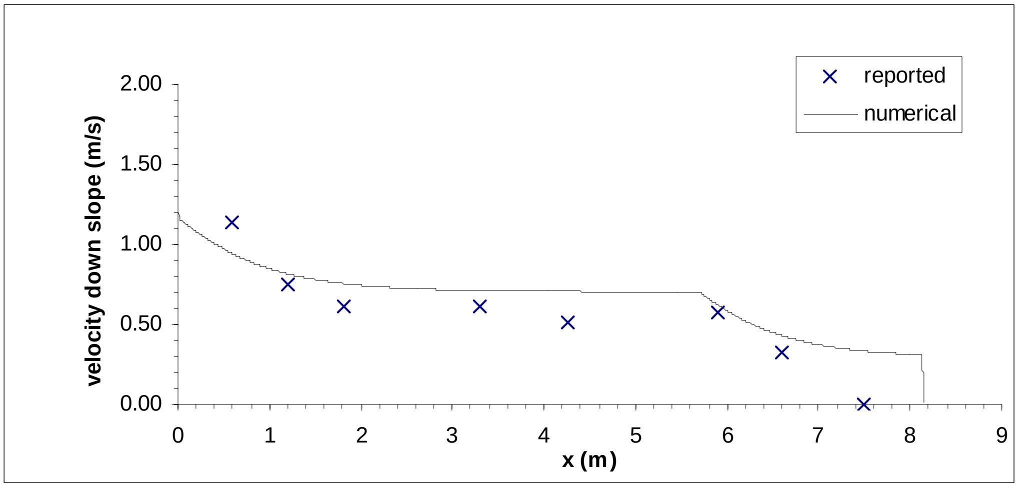

Figure 5.7: Front velocity versus run-out distance for Run 2w

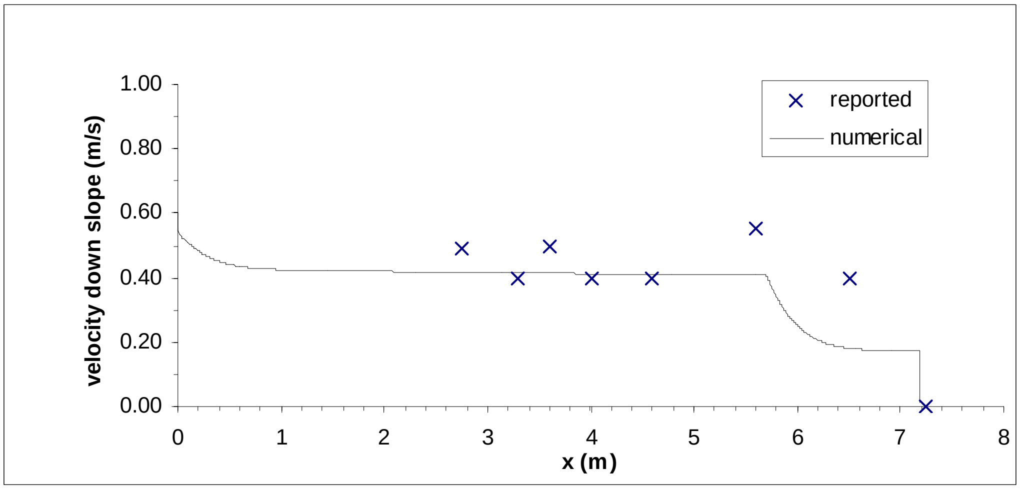

Figure 5.8: Front velocity versus run-out distance for Run 4w

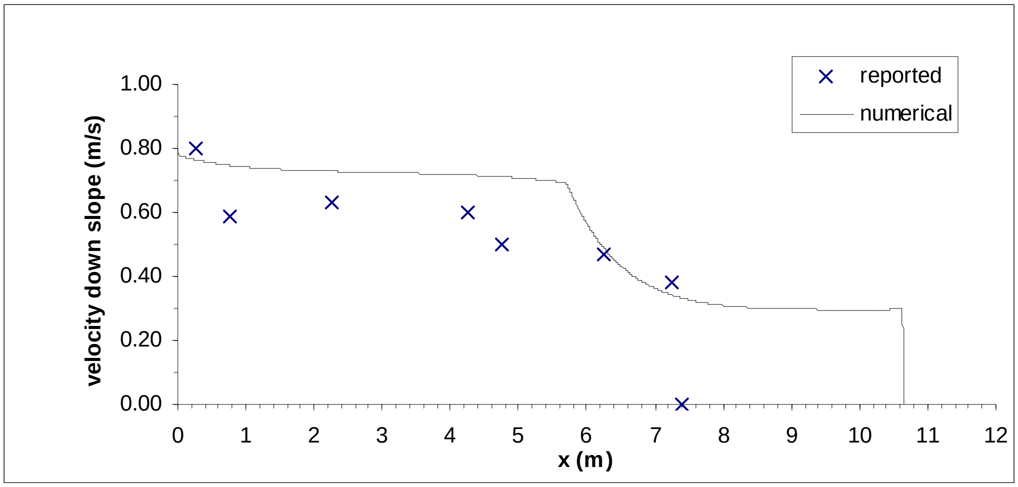

Figure 5.9: Front velocity versus run-out distance for Run 5w

5.3.2 Occurrence of hydroplaning

The calculated displacements, h_f and h_t, in the y direction normal to the underlying slope at the front and tail ends of the block, respectively, are plotted against the run-out distances for Runs 1w to 5w in Figures 5.10 to 5.14. The heights of roughness h_r are also plotted in Figures 5.10 to 5.14. It can be seen that one or both of the displacements h_f and h_t are larger than the heights of roughness h_r over a portion of the run-out distance for all five tests. Thus, the block model indicated that the slide masses should hydroplane in all tests. The ranges of run-out distances over which the displacements h_f and h_t are larger than the heights of roughness h_r are listed in Table 5.4 for the five experiments. The densimetric Froude numbers, Fr_d, for every experiment are computed from the numerical results using Equation 2.1 and are listed in Table 5.4. The densimetric Froude numbers, Fr_d, reported by Mohrig, et al. (1999) based on experimental results are also listed in Table 5.4. As shown in Table 5.4, the prediction of hydroplaning and densimetric Froude numbers, Fr_d, for the experiments is consistent with the observations by Mohrig, et al and provides further confirmation of the block model.

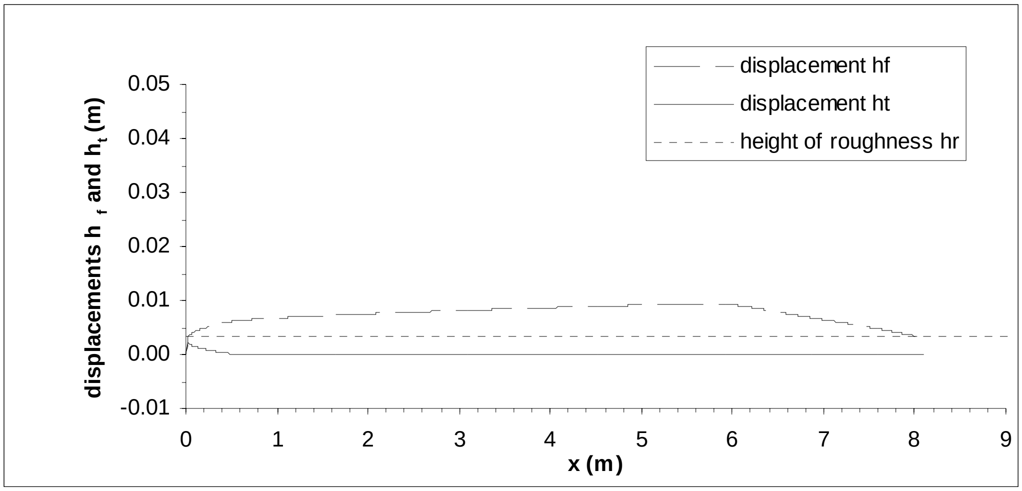

Figure 5.10: Displacements h_f and h_t versus run-out distance for Run 1w

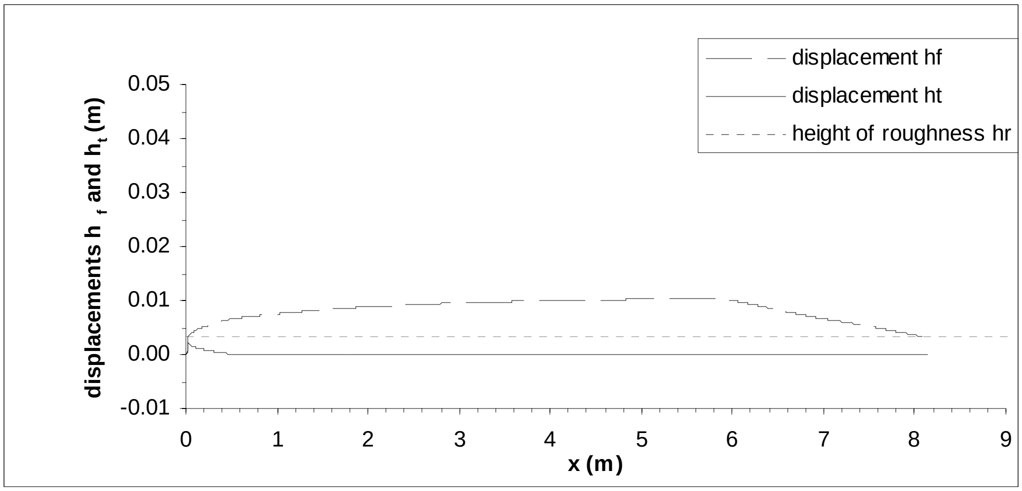

Figure 5.11: Displacements h_f and h_t versus run-out distance for Run 2w

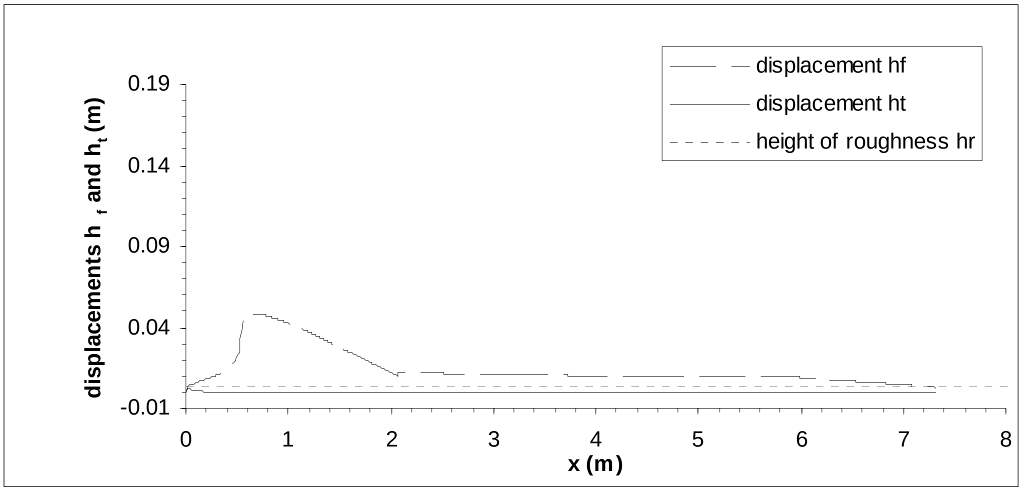

Figure 5.12: Displacements h_f and h_t versus run-out distance for Run 3w

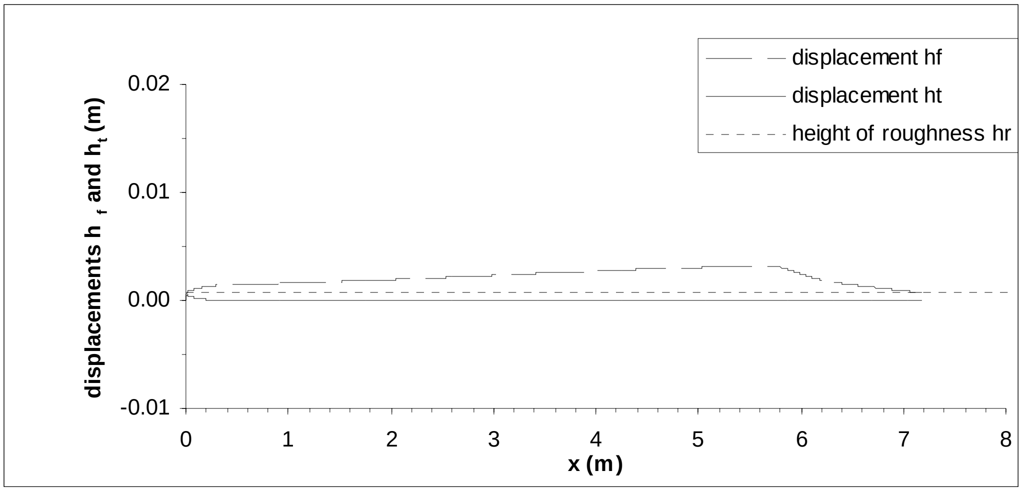

Figure 5.13: Displacements h_f and h_t versus run-out distance for Run 4w

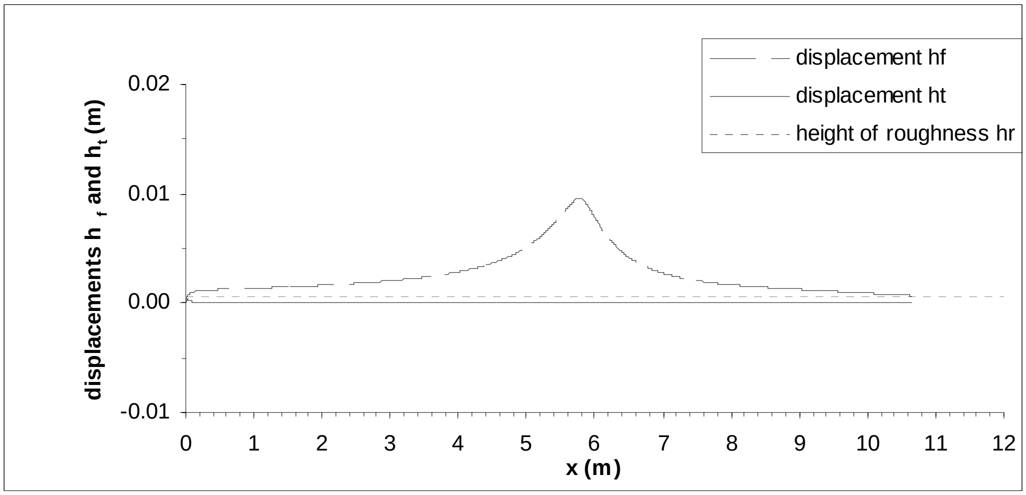

Figure 5.14: Displacements h_f and h_t versus run-out distance for Run 5w

Table 5.4: Ranges of run-out distance over which the block hydroplanes

Run	1w	2w	3w	4w	5w
Minimum run-out distance where $\max(h_f, h_t) \geq h_r$ (m)	0.03	0.02	0.01	0.01	0.02
Maximum run-out distance where $\max(h_f, h_t) \geq h_r$ (m)	8.08	8.12	7.28	7.18	10.62
Densimetric Froude number Fr_d based on numerical results	2.20	2.17	2.19	2.11	2.31
Densimetric Froude number Fr_d based on experimental results	1.90	1.99	1.98	2.47	2.04

5.4 Sequence of Sliding Stages

To illustrate the sliding process, the motion of subaqueous slides can be divided into six stages. The sequence of six stages is illustrated in Figure 5.15 for Run 1w. In Stage 1, the slide mass starts moving with an initial velocity down slope. At Stage 2, the slide mass starts to hydroplane when the displacement of the slide mass at either lower corner, h_f or h_t, becomes larger than the height of roughness h_r. Stage 3 represents steady-state hydroplaning where the velocity of the slide mass down slope is constant. In Stage 4, the slide mass decelerates due to the flatter inclination of the underlying slope. In Stage 5, the slide mass stops hydroplaning when the displacements of the slide mass, h_f and h_t, at the lower corners become both less than the height of roughness, h_r. In Stage 6, the final stage of the sliding process, the slide mass stops moving.

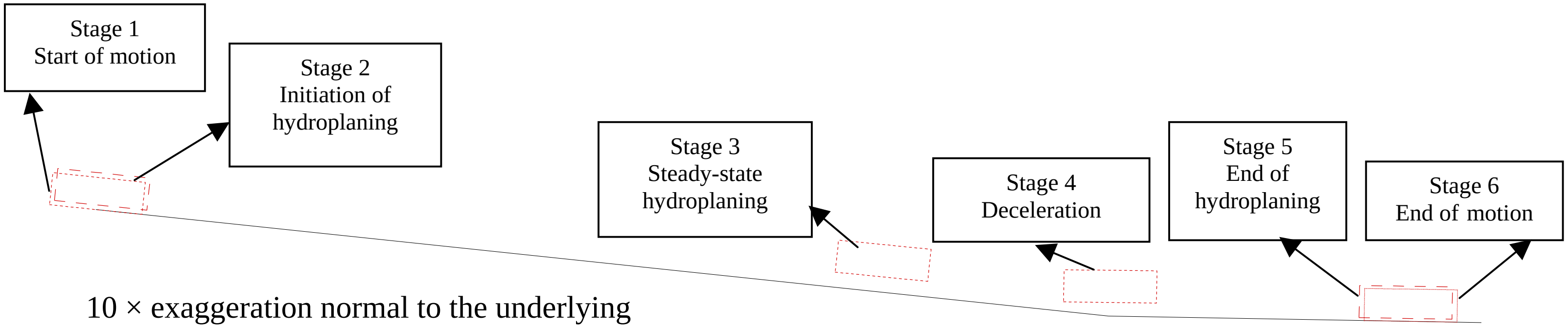

Figure 5.15: Sequence of sliding stages for Run 1w

The six stages and the run-out distance of the slide mass for each stage are listed in Table 5.5.

Table 5.5: Stages of motion for Run 1w

Stage Number	Stage Name	Run-out distance (m)
1	Beginning of the sliding process	0
2	Start of hydroplaning	0.03
3	Steady-state hydroplaning	5.30 – 5.70
4	Deceleration due to change of the underlying slope	5.70 – 8.08
5	Stop of hydroplaning	8.08
6	End of the sliding process	8.11

5.5 Sensitivity Analysis

To examine the sensitivity of numerical results to the input parameters, variations are applied to every parameter in Run 1w. The original input parameters and the variation of each parameter are listed in Table 5.6. After variation, the dynamic viscosity of the surrounding fluid is 1.00E-03 $kg \cdot m^{-1}s^{-1}$, which is the same as for pure water. The numerical results corresponding to the variations are discussed as follows.

Table 5.6: Original input parameters and changes applied for Run 1w

Parameter	Original value	Variation applied	Note
Dynamic viscosity of surrounding fluid $\mu\,(kg \cdot m^{-1}s^{-1})$	1.75E-02	-1.65E-02	After change, the dynamic viscosity is 1.00E-03, which is the same for pure water
Slope angle δ	6° for the first 5.7 m down slope	±10 percent	
	1° after the first 5.7 m down slope		
Head ratio α	2		
Non-dimensional constant λ	-5		
Non-dimensional constant β	0.5		
The modulus of elasticity for the underlying ground E (kpa)	8000		
Poisson's ratio for the underlying ground ν	0.4		
Density of soil $\rho_s\,(kg/m^3)$	1600		
Height of roughness h_r (mm)	3.2		
Static shear strength τ_y (Pa)	49		
Strain rate factor $\mu_s\,(kg \cdot m^{-1}s^{-1})$	3.5E-02		
Height of the block H (m)	1.8E-02		
Initial velocity (m/s)	1.00		
Block length L (m)	0.52		

5.5.1 Dynamic viscosity of surrounding fluid

For the two values of the dynamic viscosity of surrounding fluid (1.75E-2 and 1.00E-3 $kg \cdot m^{-1}s^{-1}$), the ranges of run-out distance over which the block hydroplanes are listed in Table 5.7. It can be seen that the block starts hydroplaning at the same run-out distance for the two values of the dynamic viscosity. The block stops hydroplaning sooner when the dynamic viscosity is 1.00E-03 $kg \cdot m^{-1}s^{-1}$ than when the dynamic viscosity is 1.75E-02 $kg \cdot m^{-1}s^{-1}$.

Table 5.7: Ranges of run-out distance over which the block hydroplanes using different dynamic viscosities of surrounding fluid

Dynamic viscosity of surrounding fluid μ ($kg \cdot m^{-1}s^{-1}$)	1.75E-02	1.00E-03
Range of run-out distance over which hydroplaning occurred (m)	0.03 – 8.08	0.03 – 6.36

The variations of the velocity down slope with run-out distance are shown in Figures 5.16 for the two values of dynamic viscosity. It can be seen that the variation of dynamic viscosity of the surrounding fluid has a negligible effect on the dynamic response of the block during hydroplaning. When the dynamic viscosity of the surrounding fluid is smaller, the block stops hydroplaning sooner and travels a shorter distance.

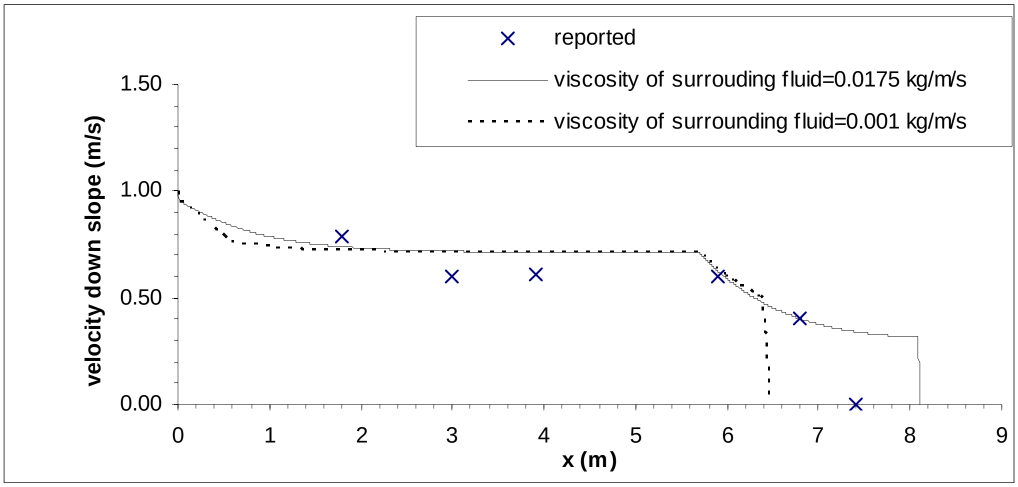

Figure 5.16: Velocity down slope versus run-out distance for two values of dynamic viscosity of surrounding fluid

5.5.2 Slope angle of underlying ground

For the three sets of slope angles for the underlying ground (5.4˚, 6˚ and 6.6˚ for the first 5.7 m down slope, 0.9˚, 1˚ and 1.1˚ after the first 5.7 m down slope) the variations of velocity down slope with run-out distance of the block are shown in Figures 5.17. It can be seen that the velocity and final run-out distance of the block decrease about 4 percent when the slope angle of underlying ground decreases 10 percent.

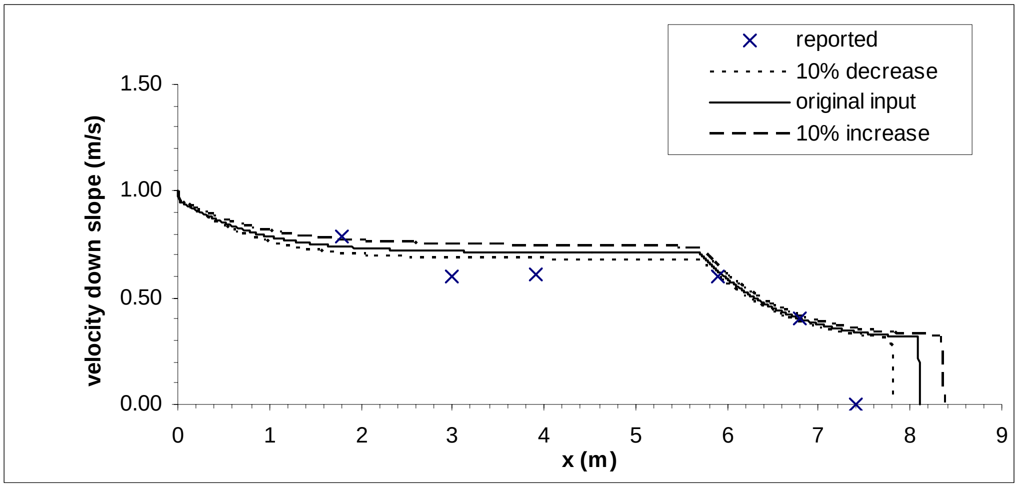

Figure 5.17: Velocity down slope versus run-out distance for three sets of slope angles of underlying ground

5.5.3 Head ratio

For three values of head ratio of the block (1.8, 2.0 and 2.2), the variations of velocity down slope with run-out distance are shown in Figures 5.18. It can be seen that the velocity and final run-out distance of the block increases about 4 percent when the head ratio decreases 10 percent.

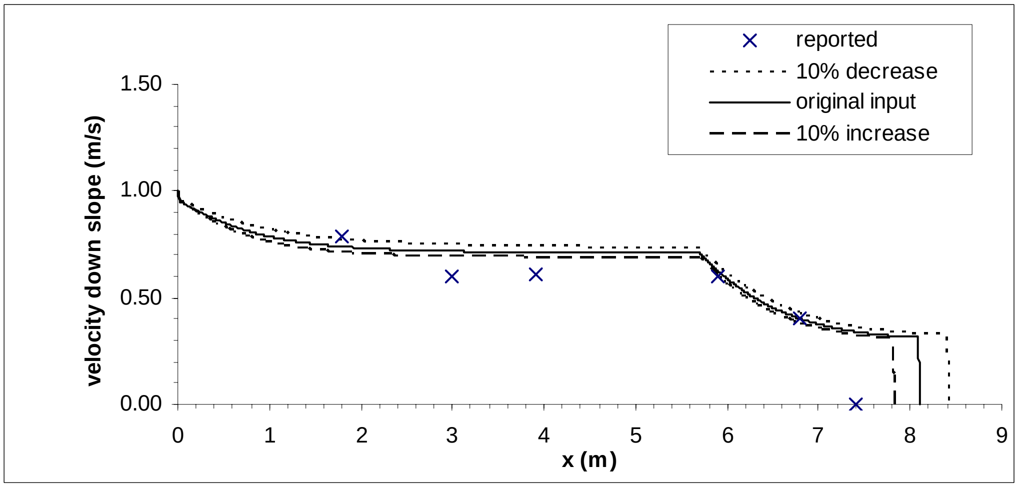

Figure 5.18: Velocity down slope versus run-out distance for three values of head ratio

5.5.4 Non-dimensional constant λ

For three values of the non-dimensional constant, λ, (-4.5, -5 and -5.5) the variations of velocity down slope with run-out distance are shown in Figures 5.19. It can be seen that a 10 percent change of non-dimensional constant, λ, has a negligible effect on numerical results.

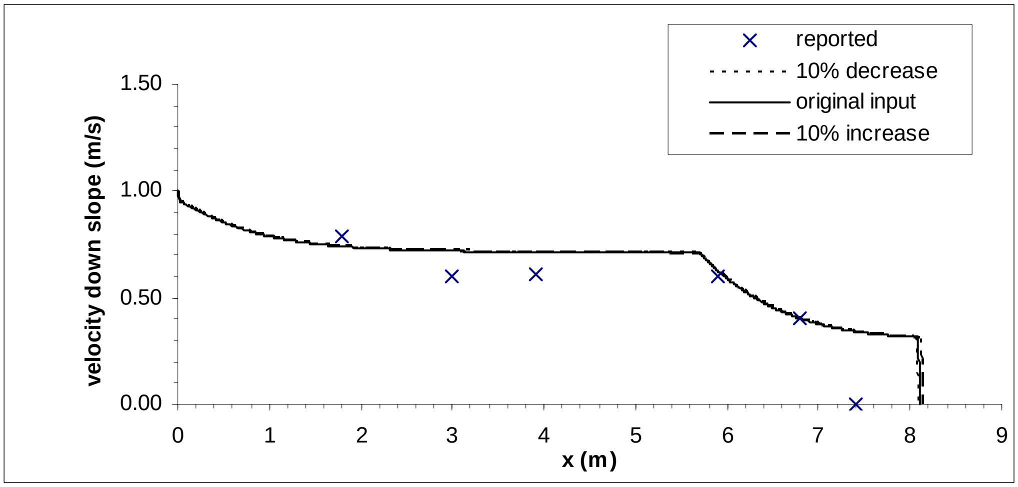

Figure 5.19: Velocity down slope versus run-out distance for three values of non-dimensional constant λ

5.5.5 Non-dimensional constant β

For three values of non-dimensional constant, β, (0.45, 0.5 and 0.55) the variations of velocity down slope with run-out distance are shown in Figures 5.20. It can be seen that a 10 percent change of non-dimensional constant, β, has a negligible effect on numerical results.

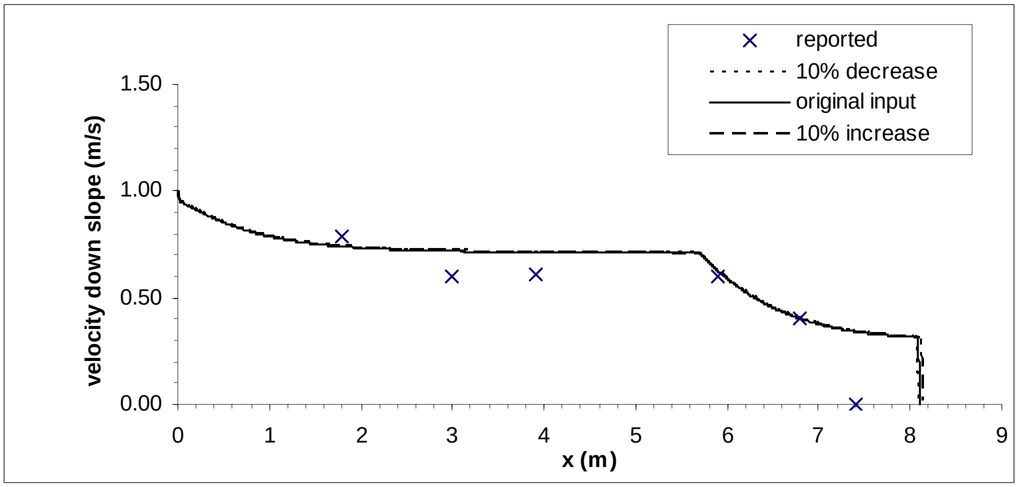

Figure 5.20: Velocity down slope versus run-out distance for three values of non-dimensional constant β

5.5.6 Modulus of elasticity of underlying ground

For three values of the modulus of elasticity for underlying ground (7200, 8000 and 8800 kpa), the variations of velocity down slope with run-out distance are shown in Figures 5.21. It can be seen that a 10 percent change of modulus of elasticity of underlying ground has a negligible effect on numerical results.

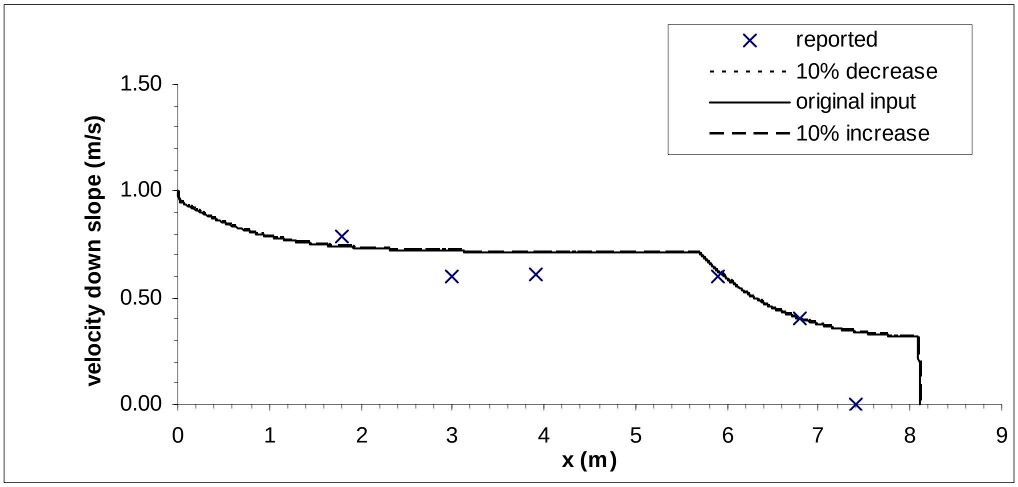

Figure 5.21: Velocity down slope versus run-out distance for three values of the modulus of elasticity for underlying ground

5.5.7 Poisson’s ratio of underlying ground

For three values of the Poisson’s ratios for underlying ground (0.36, 0.4 and 0.44), the variations of velocity down slope with run-out distance are shown in Figures 5.22. It can be seen that a 10 percent change of Poisson’s ratio of underlying ground has a negligible effect on numerical results.

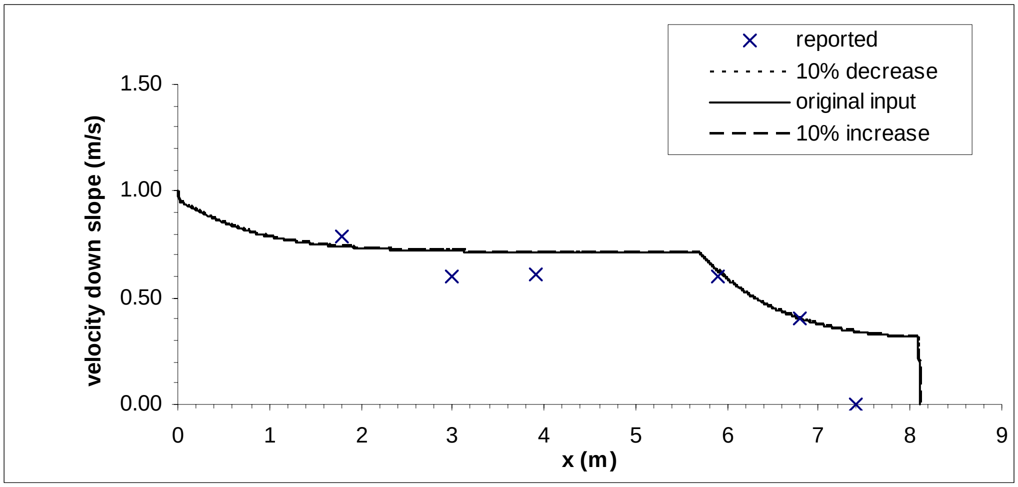

Figure 5.22: Velocity down slope versus run-out distance for three values of Poisson's ratios of underlying ground

5.5.8 Density of soil

For three values of the density of soil, the variations of velocity down slope with run-out distance are shown in Figures 5.23. It can be seen that the velocity down slope decreases about 15 percent and final run-out distance increases about 1 percent when the density of soil decreases 10 percent.

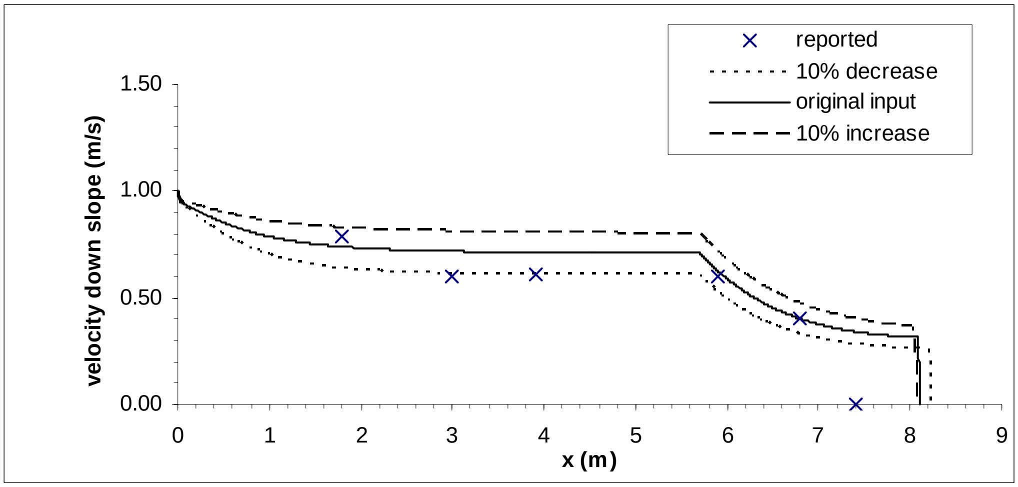

Figure 5.23: Velocity down slope versus run-out distance for three values of density of soil

5.5.9 Height of roughness

For three values of the height of roughness at the interface of block and underlying ground (2.88, 3.2 and 3.52 mm), the variations of velocity down slope with run-out distance are shown in Figures 5.24. It can be seen that final run-out distance of the block increases about 5 percent when the height of roughness decreases 10 percent. The change of velocity down slope of the block is negligible when the height of roughness changes 10 percent.

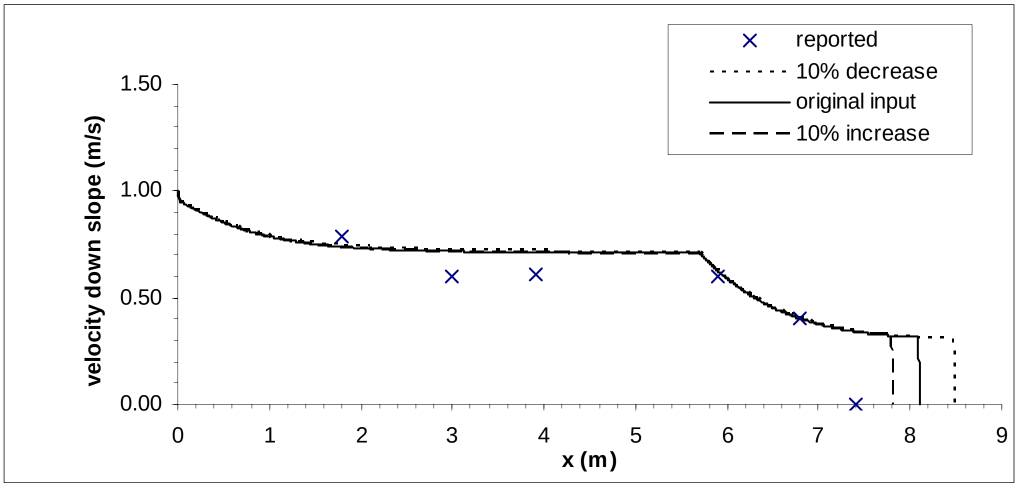

Figure 5.24: Velocity down slope versus run-out distance for three values of the height of roughness

5.5.10 Static shear strength

For three values of the static shear strength of soil (44.1, 49 and 53.9 Pa), the variations of velocity down slope with run-out distance are shown in Figures 5.25. It can be seen that a 10 percent change of static shear strength of soil has a negligible effect on numerical results.

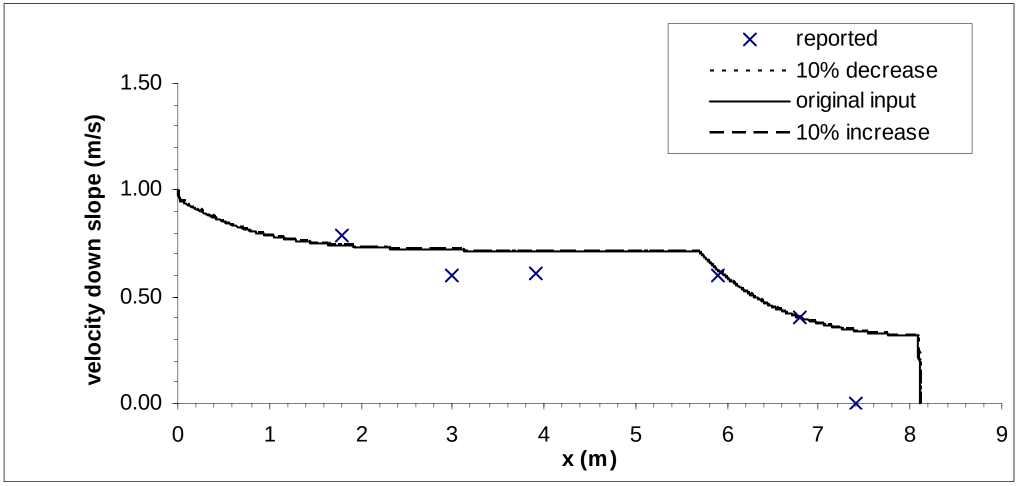

Figure 5.25: Velocity down slope versus run-out distance for three values of the static shear strength of soil

5.5.11 Strain rate factor

For three values of the strain rate factor for soil, the variations of velocity down slope with run-out distance are shown in Figures 5.26. It can be seen that the final run-out distance increases about 1 percent when the strain rate factor for the soil increases 10 percent. A 10 percent change of the strain rate factor has a negligible effect on the velocity down slope.

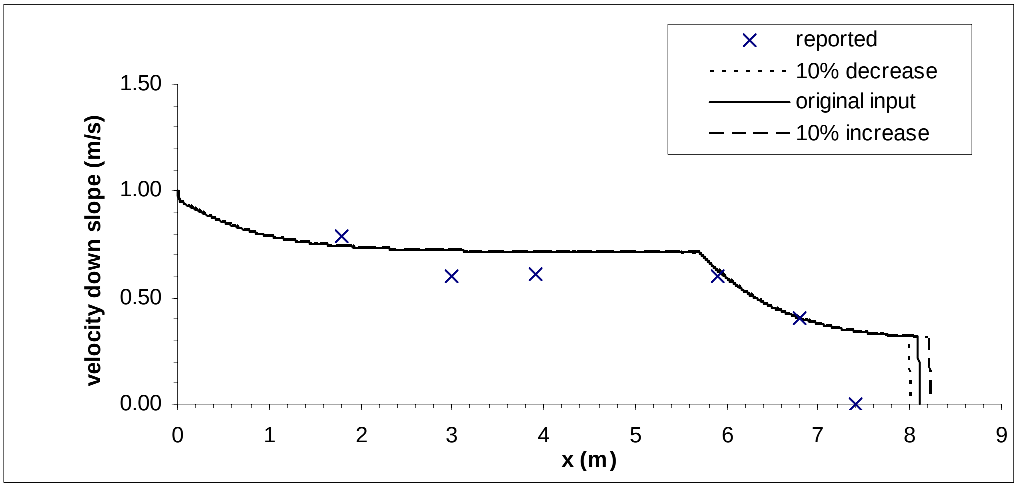

Figure 5.26: Velocity down slope versus run-out distance for three values of strain rate factor for soil

5.5.12 Height of block

For three values of the height of block (0.0162, 0.018 and 0.0198 m), the variations of velocity down slope with run-out distance are shown in Figures 5.27. It can be seen that the final run-out distance decreases about 2 percent when the height of block increases 10 percent. A 10 percent change in the height of the block has a negligible effect on the velocity down slope.

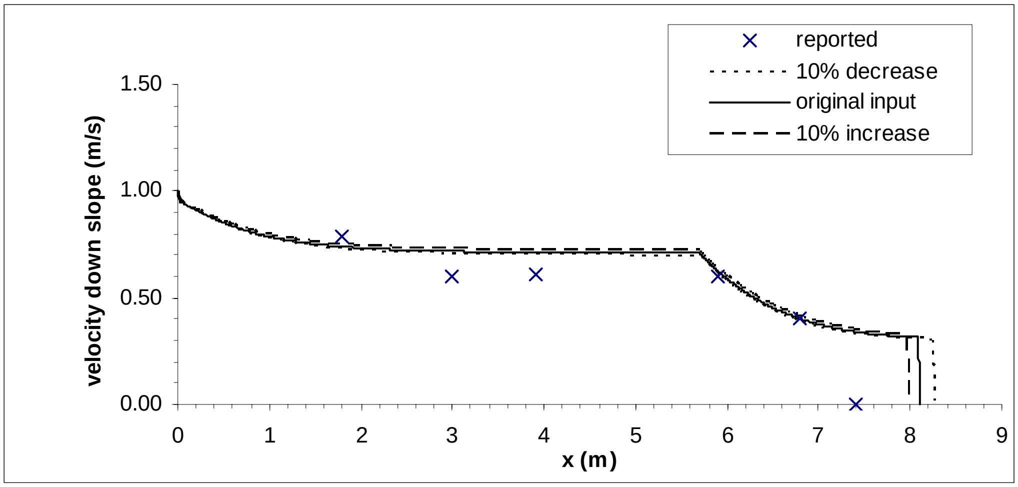

Figure 5.27: Velocity down slope versus run-out distance for three values of height of the block

5.5.13 Initial velocity

For three values of the initial velocity of the block (0.9, 1.0 and 1.1 m/s), the variations of velocity down slope with run-out distance are shown in Figures 5.28. It can be seen that a 10 percent change of initial velocity of the block has a negligible effect on numerical results.

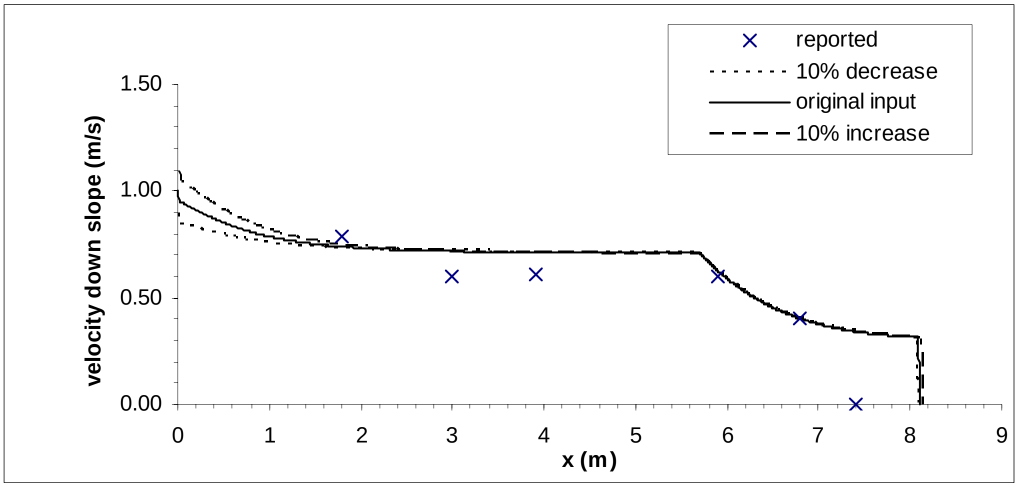

Figure 5.28: Velocity down slope versus run-out distance for three values of the initial velocity of the block

5.5.14 Length of block

For three values of the length of the block (0.47, 0.52 and 0.57 m), the variations of velocity down slope with run-out distance are shown in Figures 5.29. It can be seen that the velocity down slope increases about 4 percent and final run-out distance of the block increases about 7 percent when the length of block increases 10 percent.

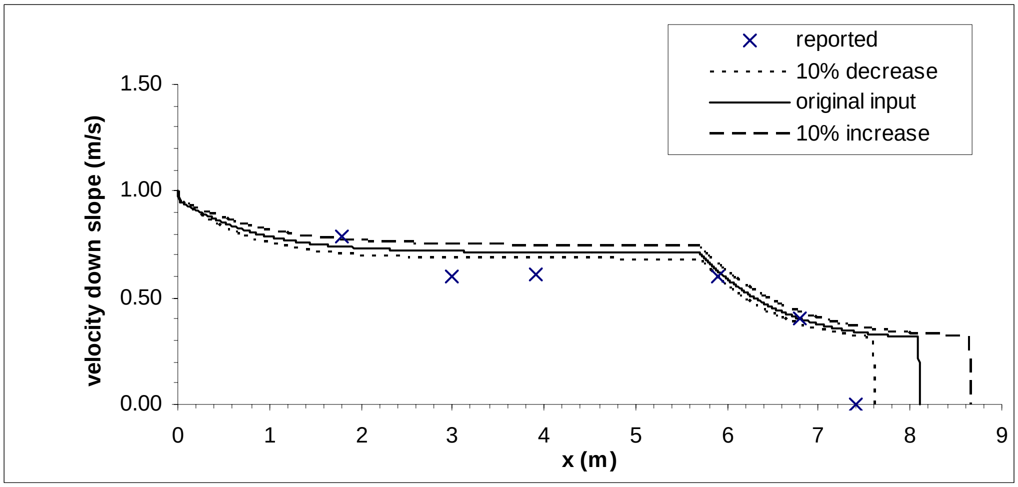

Figure 5.29: Velocity down slope versus run-out distance for three values of the length of the block

5.6 Summary and Conclusions

Numerical simulations have been conducted using the block model for the five laboratory experiments of subaqueous slides performed by Mohrig, et al. The numerical results have been compared to the experimental data reported by Mohrig, et al. A sensitivity analysis has also been conducted for every input parameter of the block model.

The analyses presented have shown that the block model predicts the motion of subaqueous slides including the occurrence of hydroplaning with acceptable accuracy. The changes in velocity down slope and final run-out distance with 10 percent change in each parameter of the block model are summarized in Table 5.8. It can be seen that a 10 percent change of every parameter does not result in any change of numerical results that is larger than 15 percent.

Table 5.8: Changes in numerical results with variations of input parameters for Run 1w

Parameter	Variation applied	Change in velocity down slope	Change in final run-out distance
Dynamic viscosity of surrounding fluid $\mu\,(kg \cdot m^{-1}s^{-1})$	-94 percent (-1.65E-02 $kg \cdot m^{-1}s^{-1}$)	Negligible	-20 percent
Slope angle δ (degree)	±10 percent	±4 percent	±4 percent
Head ratio α		∓4 percent	∓4 percent
Non-dimensional constant λ		Negligible	Negligible
Non-dimensional constant β		Negligible	Negligible
The modulus of elasticity for the underlying ground E (kpa)		Negligible	Negligible
Poisson's ratio for the underlying ground ν		Negligible	Negligible
Density of soil $\rho_s\,(kg/m^3)$		±15 percent	∓1 percent
Height of roughness h_r (mm)		Negligible	∓4 percent
Static shear strength τ_y (Pa)		Negligible	Negligible
Strain rate factor $\mu_s\,(kg \cdot m^{-1}s^{-1})$		Negligible	±1 percent
Height of the block H (m)		Negligible	∓2 percent
Initial velocity (m/s)		Negligible	Negligible
Block length L (m)		±4 percent	±7 percent

Chapter 6: Numerical Simulation for the Sediment Slab during the Storegga Slide Using the Block Model

The block model was applied to simulate the movement of a large sediment slab during the Storegga slide. In this chapter the general conditions of the Storegga slide and of the sediment slab studied are presented first. The input parameters for the block model are then discussed. Next numerical results from analyses with the block model are presented and compared with the findings of site investigations reported by Bugge, et al (1988). Finally the block model was modified to neglect hydroplaning of the slide mass. The effect of hydroplaning on the run-out distance of the slide mass was then evaluated by comparing the numerical results from the block model with and without hydroplaning.

6.1 Storegga Slide

The Storegga Slide is one of the largest submarine slides known. As shown in Figure 6.1, the headwall is approximately 290 km wide and located about 100 km from the coast of Norway. According to site investigations reported by Bugge, et al. (1988), the slide extends from the headwall for more than 800 km to the abyssal floor of the Norwegian Sea. The water depth is 150 – 400 m at the headwall and 3000 – 3500 m at the abyssal floor. The maximum thickness of the slide is 450 m and about 5600 km^3 of sediment was involved in the sliding.

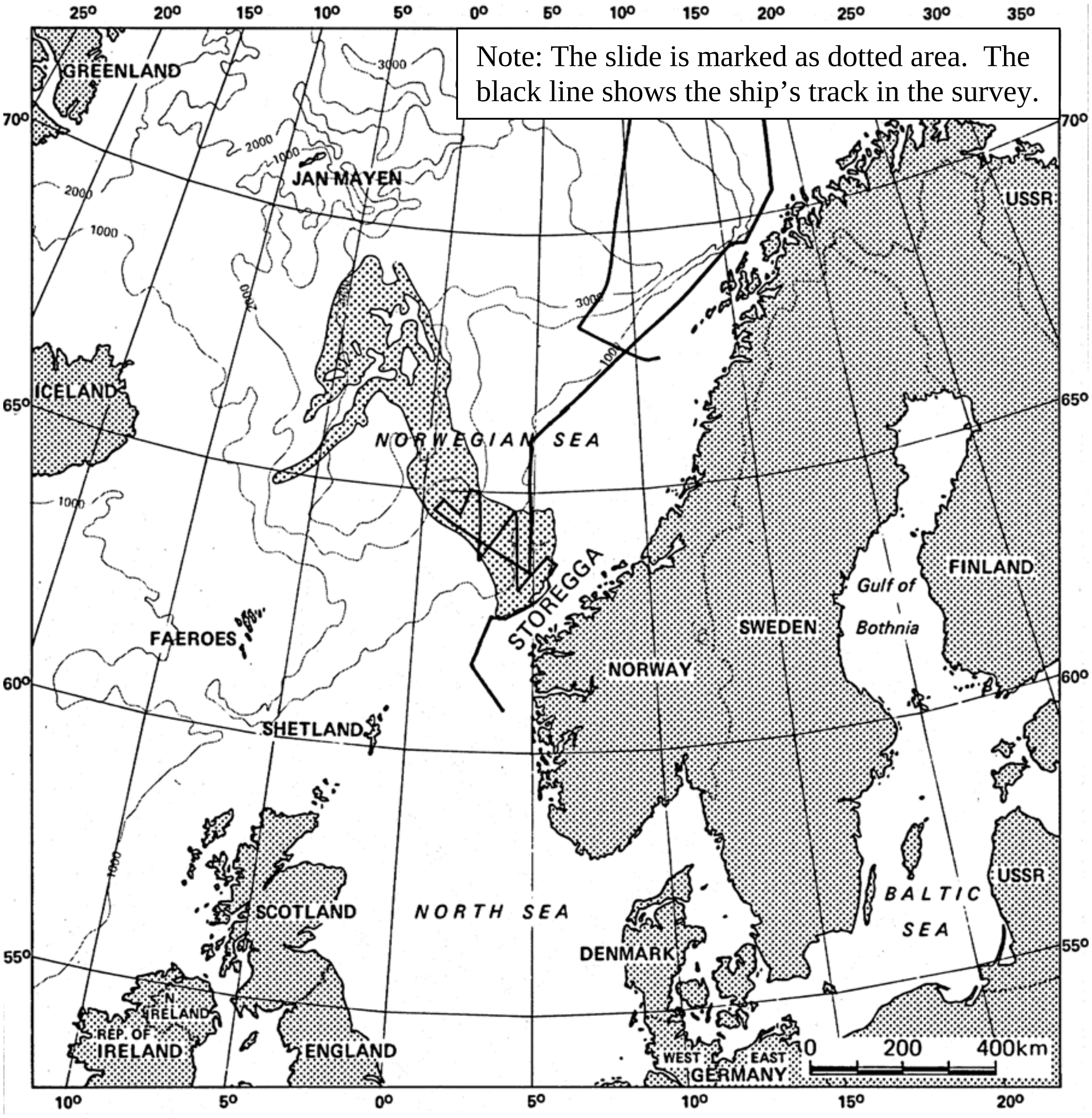
Note: The slide is marked as dotted area. The black line shows the ship's track in the survey.

Figure 6.1: Location of the Storegga slide (Modified from Bugge, et al. 1988)

Three major stages are distinguished in the history of the Storegga slide. The extents of the three stages are shown in Figure 6.2. About 30,000 – 50,000 years BP, the first stage (referred to as the First Storegga Slide) removed about 3880 km^3 of normally consolidated clayey Plio-Pleistocene sediments. After the uppermost sediments were removed by the first stage, the second stage (referred to as the Second Storegga Slide) cut an additional 100 – 200 m into over consolidated sediments about 6,000 – 8,000 years BP. The headwall retreated 6 - 8 km towards the continental shelf during the second event. Huge blocky deposits of the second stage produced hummocky seafloor topography with local relief of up to 100 m or more. The size of the sediment blocks varies from hundreds of meters at the depositional tongues to thousands of meters for two slabs at the upper part of the slide scar. More details of the slabs are discussed in the next section. The third event (referred to as the Third Storegga Slide) could be a final delayed stage of the Second slide and was limited to the upper part of the slide scar. At every stage of the Storegga slide, turbidity currents transported fine-grained deposits along the route of the slide. The estimated area, thickness and volumes of the three main slides are summarized in Table 6.1.

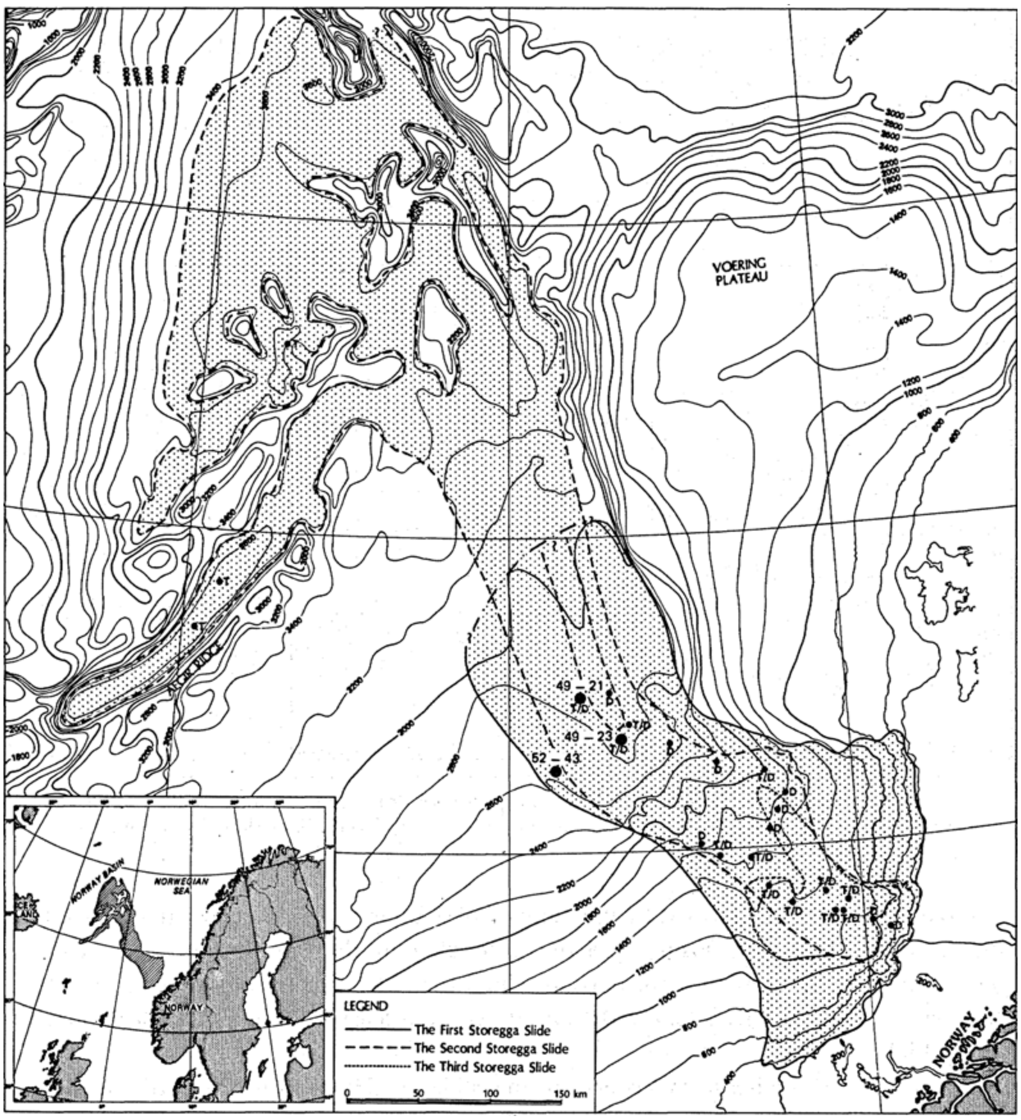

Figure 6.2: Extents of three stages of the Storegga slide (Bugge, et al. 1988)

Table 6.1: Dimension of Storegga slide

	First Storegga slide	Second Storegga slide	Third Storegga slide	Total
Run-out distance (km)	350 - 380	800 - 850	100 - 130	850
Area of slide scar (km^2)	34,000	19,200	6,000	34,000
Maximum thickness (m)	280	330		430
Average thickness (m)	114	88		160
Volume (km^3)	3,880	1,700		5,580

6.2 Sediment Slab

During the second stage of the Storegga slide, a large slab of intact sediments was transported from the upper part of the slide scar at 1,000 m water depth to the lower part of the slide scar at 2,000 – 2,500 m water depth. The pathway of the slab and its final resting position are shown in Figure 6.3. The slope gradients along the pathway are shown in Figure 6.4. The average slope angle for every segment of the pathway is listed in Table 6.2. The run-out distance of the slab is about 200 km. The slab is approximately 150 – 200 m thick, 10 km wide and 30 – 50 km long.

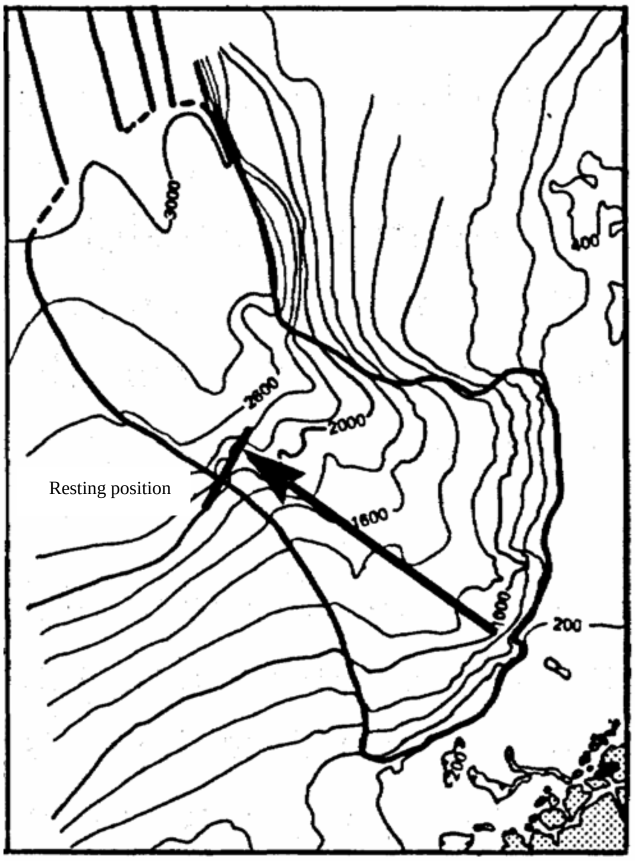

Figure 6.3: Pathway of the slab (Modified from Bugge, et al. 1988)

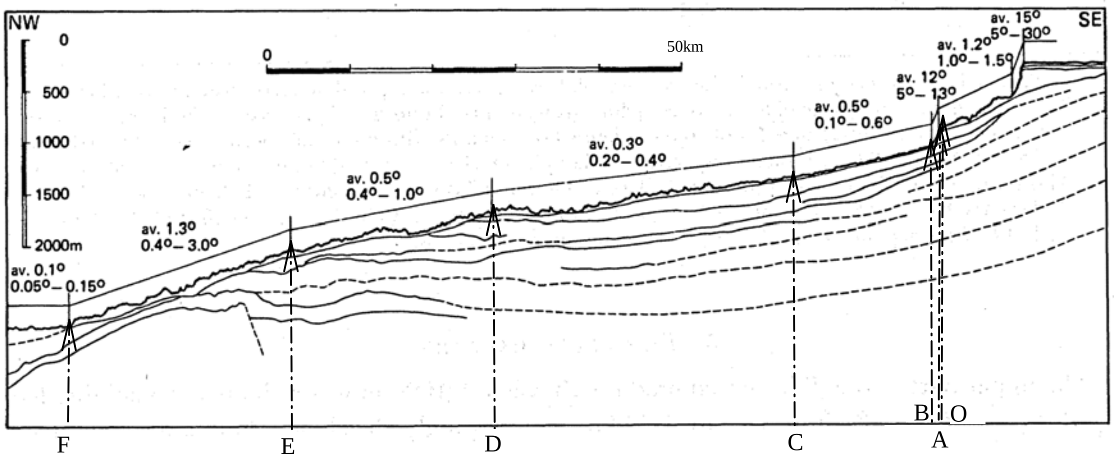

Figure 6.4: Slope gradients along the pathway (Modified from Bugge, et al. 1988)

Table 6.2: Slope angle for every segment of the pathway of sediment slab

Segment	Run-out distance (m)	Average slope angle (degree)
OA	0 - 500	1.2
AB	500 - 2172	12
BC	2172 - 21313	0.5
CD	21313 - 54489	0.3
DE	54489 - 73204	0.5
EF	73204 - 88520	1.3
After F	> 88520	0.1

6.3 Input Parameters

The slope angles for the underlying ground are listed in Table 6.2, while the values of the other parameters are listed in Table 6.3. The methods used to determine all the input parameters are elaborated in this section.

Table 6.3: Input parameters used for analyses with the block model

Input parameter	Value
Height of the block H (m)	175
Block length L (m)	40,000
Initial velocity (m/s)	0
Height of roughness h_r (mm)	70
Density of soil $\rho_s\ (kg/m^3)$	1,600
Static shear strength τ_y (Pa)	20500, 19400, or 18350
$\mu_s\ (kg \cdot m^{-1}s^{-1})$	500
Dynamic viscosity of surrounding fluid $\mu\ (kg \cdot m^{-1}s^{-1})$	0.001
Head ratio α	2
Non-dimensional constant λ	-5
Non-dimensional constant β	0.5
Modulus of elasticity for the underlying ground E (kPa)	8.0E9
Poisson's ratio for the underlying ground ν	0.4
Density of underlying ground $\rho_g\ (kg/m^3)$	2,000
Time increment Δt (s)	1.0E-5

6.3.1 Parameters determined directly

The height of the block H is assumed to be the average of the range (150 – 200 m) reported by Bugge, et al. (1988). The length of block L is also assumed to be the average of the reported range (30 – 50 km, according to Bugge, et al. 1988). The initial velocity of the block is assumed to be zero because the slide mass is assumed to be at rest initially. The height of roughness h_r is assumed to be 70 mm according to the reported range by De Blasio, et al. (2004). The total density of soil, ρ_s, in the slide mass is assumed to be 1600 kg/m^3.

In order to determine the static shear strength of soil, τ_y, the forces and stresses on the slide mass before it starts moving are studied. All the forces and stresses on the slide mass at rest are shown in Figure 6.5. The equation of equilibrium down slope can be expressed as:

$$G' \sin\delta = \tau \cdot L \tag{6.1}$$

where δ is the slope angle of the underlying ground, which is 1.2° as shown in Figure 6.4 for the segment OA, τ is the shear stress along the bottom surface of the slide mass and G' is the submerged weight of the slide mass which can be calculated as:

$$G' = (\rho_s - \rho_w) gHL \tag{6.2}$$

Where ρ_w is the density of surrounding water and g is the acceleration due to gravity. The shear stress, τ, is assumed to be equal to the peak shear strength of soil, $\tau_{y,peak}$, before the slide mass starts moving, i.e.

$$\tau = \tau_{y,peak} \tag{6.3}$$

Substitution of Equations 6.2 and 6.3 into Equation 6.1 yields:

$$(\rho_s - \rho_w) gHL \sin\delta = \tau_{y,peak} L \tag{6.4}$$

Solving Equation 6.4 for $\tau_{y,peak}$ gives:

$$\begin{aligned}\tau_{y,peak} &= (\rho_s - \rho_w) g H \sin\delta \\ &= (1600 - 1000) \times 9.82 \times 175 \times \sin(1.2^\circ) \\ &\approx 21 \;\; kPa\end{aligned} \tag{6.5}$$

Therefore the peak shear strength, $\tau_{y,peak}$, of soil in the slide mass is assumed to be 21 kPa. In order to initiate the movement of the slide mass, the static shear strength, τ_y, is assumed to be smaller than the peak shear strength $\tau_{y,peak}$. A reduction of 5%, 10% or 15% is applied to the peak shear strength $\tau_{y,peak}$ to estimate the static shear strength τ_y of the soil. The estimates of static shear strength are listed in Table 6.3.

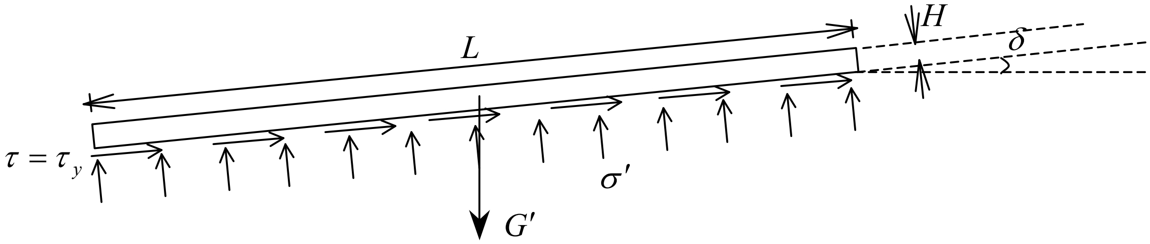

Figure 6.5: Forces and stresses on the slide mass at rest

The strain rate factor, μ_s, for soil in the slide mass is assumed to be 500 $kg \cdot m^{-1} s^{-1}$ which is the average value of the reported range (100 – 1000 $kg \cdot m^{-1} s^{-1}$) by De Blasio et al. (2004). Although there may have been some mixing of soil with the surrounding water, the viscosity of the surrounding water μ is taken as that of pure water, which is 0.001 $kg \cdot m^{-1} s^{-1}$. The head ratio α and non-dimensional constants λ and β are based on the frontal shape of the sliding mass from Mohrig, et al.'s (1999) experiments as shown in Figure 5.2. Consequently the input values of head ratio α and non-dimensional constants λ and β are the same as those used for the simulations of experiments in Chapter 5. The modulus of elasticity for the underlying ground E and the Poisson's ratio for the underlying ground ν are based on general properties for stiff clay (Das, B. 1999). The total density ρ_g of soil in the underlying ground is assumed to be

2000 kg/m^3. The slope angle, δ, of the underlying ground varies with location as shown in Figure 6.4 and is listed in Table 6.2.

6.3.2 Parameters determined by trial and error

The increment of time Δt used in the numerical simulation was determined by trial and error. Three trial values of 0.0001 s, 0.00001 s and 0.000001 s were used for the increment of time Δt. The numerical solutions failed to converge for Δt of 0.0001 s. However for Δt of 0.00001 s and 0.000001 s, the numerical solutions converged. The difference between the numerical results using Δt as 0.00001 s and as 0.000001 s was negligible. Therefore a Δt of 0.00001 s was chosen for the numerical simuation with the block model. The numerical results are discussed in the following sections.

6.4 Numerical Results

The run-out distance, velocity down slope and displacement in the y direction were calculated as functions of time. The calculated final run-out distance, velocity down slope and displacement normal to the underlying slope are discussed in the sections below.

6.4.1 Run-out distance

The calculated run-out distance of the slide mass versus time is shown in Figure 6.6 for 5%, 10% and 15% reductions of the peak static shear strength $\tau_{y,peak}$. The difference in numerical results using 5%, 10% or 15% reduction is negligible. Thus for the following discussion in this chapter, only the numerical results using a 10% reduction of peak static shear strength are presented.

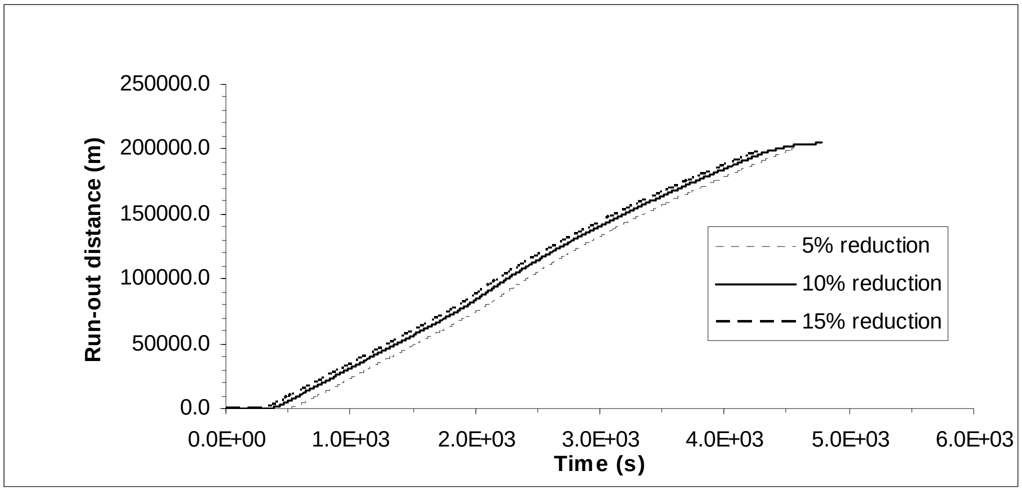

Figure 6.6: Run-out distance versus time

As shown in Figure 6.6, the final run-out distance of the slide mass is 204,000 m. This distance is close to the reported value of 200,000 m, by Bugge, et al, and, thus, the block model predicts the run-out distance of the slide mass relatively well.

6.4.2 Occurrence of hydroplaning

The calculated displacements in the y direction at the front and tail ends of the block h_f and h_t are plotted against the run-out distances in Figures 6.7 and 6.8 respectively. The height of roughness h_r is also plotted in Figures 6.7 and 6.8. As shown in Figure 6.7, the displacement, h_f, at the front end of the block is larger than the height of roughness h_r over the run-out distances between 2,100 and 195,300 m. Also shown in Figure 6.8, the displacement, h_t, at the tail end of the block is larger than the height of roughness h_r over a much smaller range of run-out distances from 77,900 to 84,800 m. The range of run-out distances over which the block hydroplanes is from 2,100 and 195,300 m.

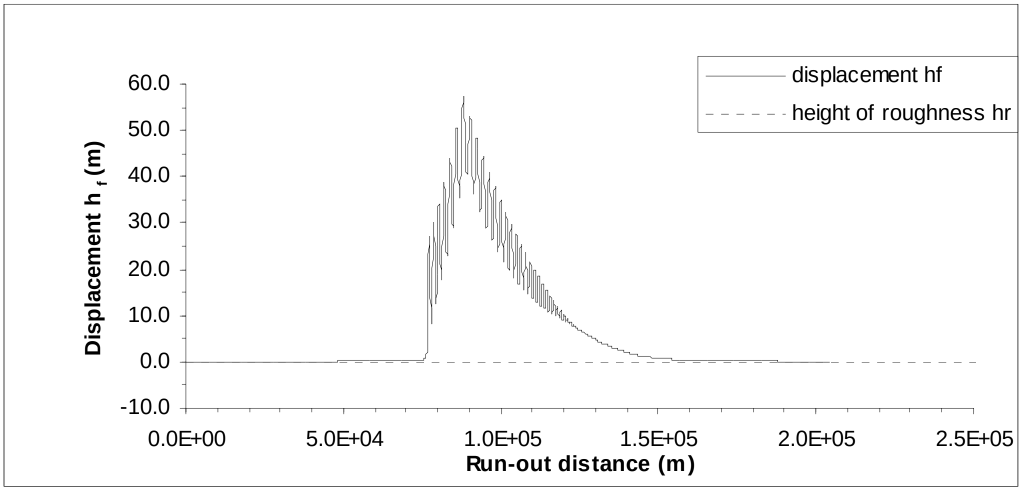

Figure 6.7: Variation of displacement, h_f, in the y direction at the front end of the block with run-out distance

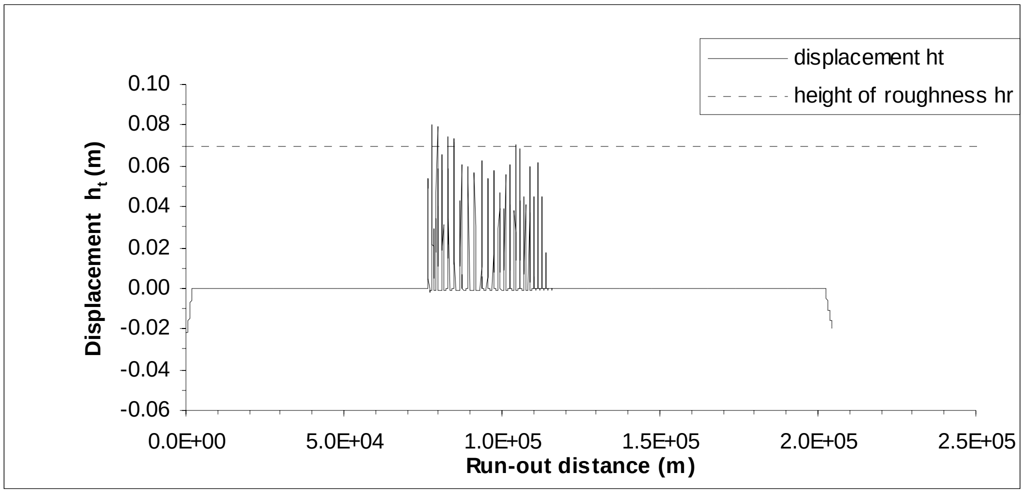

Figure 6.8: Variation of displacement, h_t, in the y direction at the tail end of the block with run-out distance

6.4.3 Velocity down slope

The variation of the velocity down slope with run-out distance of the block is shown in Figure 6.9 together with the slope angle of the underlying ground. For run-out distance from 0 to 500 m, the slope angle of the underlying ground is 1.2 degrees and the velocity down slope of the block increases from 0 to 3 m/s. For run-out distance from 500 to 2,172 m, the slope angle of the underlying ground is 12 degrees and the velocity down slope of the block increases rapidly from 3 to 48 m/s. For run-out distance from 2172 to 73,204 m, the slope angle of the underlying ground is between 0.3 to 0.5 degrees and the velocity down slope of the block is approximately 50 m/s. For run-out distance from 73,204 to 88,520 m, the slope angle increases to 1.3 degrees and the velocity down slope of the block increases from approximately 50 to 65 m/s. For run-out distance from 88,520 to 204,000 m, the slope angle of the underlying ground is 0.1 degrees and the velocity down slope of the block decreases from 65 to 0 m/s. At the run-out distance of 195,300 m, the decreasing rate of front velocity increases abruptly because the block stops hydroplaning at this run-out distance as discussed in Section 6.4.2.

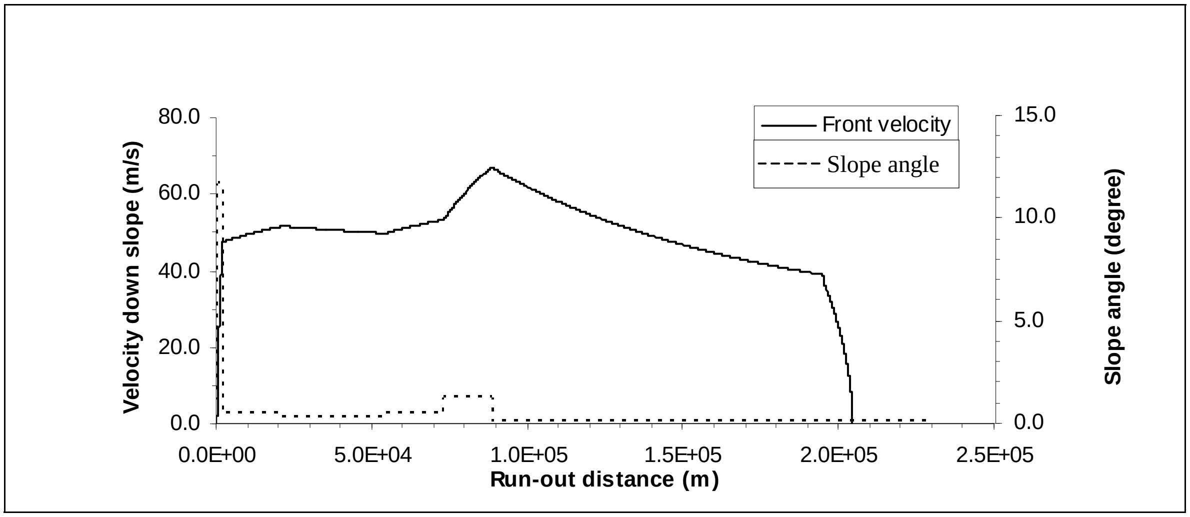

Figure 6.9: Front velocity versus run-out distance

As discussed in Section 6.4.2, the block starts to hydroplane at a run-out distance of approximately 2,100 m. At this point the velocity down slope of the block is 46.6 m/s and the slope of the underlying ground is 12 degrees. Using Equation 2.1, the densimetric Froude number Fr_d for the block to hydroplane is calculated as

$$
\begin{aligned}
Fr_d &= \frac{U}{\sqrt{\left(\frac{\rho_s}{\rho_w}-1\right) gH\cos\theta}} \qquad (6.6)\\
&= \frac{46.6}{\sqrt{\left(\frac{1600}{1000}-1\right)\times 9.82\times 175\times\cos 12^o}}\\
&= 1.47
\end{aligned}
$$

The densimetric Froude number Fr_d for the sediment slab to hydroplane is 1.47, which is close to the critical Froude number ($Fr_{d,crit} = \sqrt{2}$) as discussed in Section 2.5.2.

6.5 Effect of Hydroplaning

In order to study the effect of hydroplaning on the motion of the slide mass, the block model was modified by assuming that the block does not move normal to the underlying slope and, thus, hydroplaning can not occur. Using this modified block model, the motion of the sediment slab was simulated again.

In Figure 6.10, the variation of the velocity down slope with the run-out distance of the slide mass with no hydroplaning is plotted together with the previous results where hydroplaning was considered. It can be seen that when hydroplaning is not allowed, the final run-out distance of the slide mass is much smaller than that when hydroplaning is allowed.

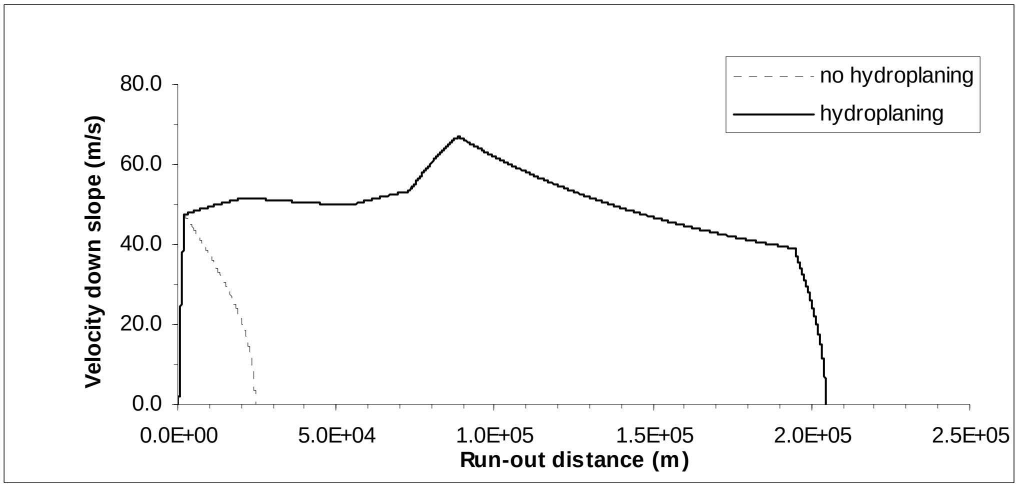

Figure 6.10: Front velocity versus run-out distance of the slide mass

6.6 Summary and Conclusions

The numerical analyses of the motion of the sediment slab during the Storegga Slide with the block model showed generally good agreement with findings reported by Bugge, et al (1988). Using input parameters based on the site investigation, the calculated final run-out distance of the slide mass is close to that reported by Bugge, et al. In contrast, the numerical analyses with hydroplaning neglected predicted a much smaller final run-out distance of the slide mass. Thus, hydroplaning appears to be the mechanism explaining why the sediment slab traveled a distance of approximately 200,000 m.

Chapter 7: Summary and Conclusions

Many submarine slides travel large distances that are much greater than those of comparable subaerial slides. One possible reason for the large travel distances is that hydroplaning occurs. The research presented in this dissertation was undertaken to understand better the mechanism of hydroplaning of submarine slides.

Previous studies on hydroplaning of submarine slides have two major limitations. One limitation is due to a lack of understanding of the hydrodynamic stresses applied on the slide mass by the surrounding fluid. The other limitation is that the onset of hydroplaning is based on arbitrary assumptions. The objective of this research was to develop a better understanding of the hydrodynamic stresses and incorporate this into a new model for hydroplaning of subaqueous slides.

7.1 Summary of Work

The hydrodynamic stresses, i.e. kinetic pressures and viscous shears, applied on the slide mass by the surrounding fluid were studied numerically. For the numerical modeling, the slide mass was assumed to be a streamline shaped rigid body with a constant velocity. Steady two-dimensional flow around the slide mass was simulated using commercial software known as, Fluent 6.1. A Reynolds-Stress turbulent model was applied to simulate the flow. The kinetic pressures and viscous shears along the surfaces of the slide mass were analyzed for slide masses with varying slide velocities, distances between the slide mass and underlying ground, and height-to-width ratios of the front portion of the slide mass. The study produced a better understanding of the interaction between the slide mass and surrounding fluid. The findings regarding the hydrodynamic stresses exerted on the slide mass are summarized in section 6.2.

Once the hydrodynamic stresses were understood better a “block model” was developed for subaqueous slides, with emphasis on possible hydroplaning. In the block model, the slide mass was represented as a rigid rectangular block which moves and rotates in a vertical plane. The occurrence of hydroplaning was determined by the contact condition between the bottom surface of the block and the underlying ground, i.e. by comparing the height of roughness at the interface between the block and underlying ground with the displacement of the block in the direction normal to the underlying ground along the bottom surface of the slide mass. Conclusions derived for the hydrodynamic stresses on the slide mass were applied as stress boundary conditions for the block model. The sliding process of the block was disretisized in a step-by-step manner using a Newmark scheme. A computer program was also written to implement the block model.

Once the block model was developed, laboratory experiments on subaqueous slides conducted by Mohrig, et al (1999) were simulated using the model. The numerical results from the block model were compared with data reported by Mohrig, et al, i.e. the variation in the computed velocities of the front of the slide mass with run-out distances of the slides were compared with measured values. The occurrence of hydroplaning was also analyzed by comparing the calculated displacements of the block normal to the underlying ground with the heights of roughness over the run-out distances. Conclusions drawn from the comparison between the block model and experiments are also summarized in Section 6.2.

After validation, the block model was applied to simulate the motion of the sediment slab during the second Storegga slide. The input parameters were determined based on the findings of site investigation reported by Bugge, et al. (1988). The occurrence of hydroplaning and its effect on the motion of the slide mass were discussed.

The calculated final run-out distance of the slide mass was compared to the reported data by Bugge, et al. Conclusions drawn from the discussion and comparison are summarized in Section 6.2.

7.2 Conclusions

The research reported herein provides a better understanding of subaqueous slides by considering the interactions between the slide mass and the surrounding fluid and between the slide mass and the underlying ground. Unlike previous models for subaqueous slides, the block model involves no arbitrary assumptions for the hydrodynamic stresses on the slide mass or the on-set condition of hydroplaning.

The numerical study of the interaction between the slide mass and surrounding fluid has produced the following conclusions regarding the hydrodynamic stresses on the surfaces of the slide mass:

1. When normalized by the stagnation pressure p_{stag}, the non-dimensional kinetic pressures on the surfaces of the slide mass are not influenced by the magnitude of the free field velocity;
2. Along the top surface of the slide mass, hydrodynamic stresses are not influenced by the onset of hydroplaning or the distance between the underlying ground and the bottom surface of the slide mass that hydroplanes;
3. The kinetic pressures on the middle portion of the top surface is essentially zero for slides in deep water;

4. The non-dimensional kinetic pressures on the tail portion of the top surface of the slide mass increases linearly from zero at the intersection of the middle and tail portions to 0.3 at the tail end of the slide mass;
5. The kinetic pressure is negative along the frontal part of the top surface. This kinetic pressure provides a lift on the slide mass. The magnitude of this negative pressure increases as the height-to-width ratio of the slide mass increases;
6. Along the bottom surface of slide mass that hydroplane, the non-dimensional kinetic pressures vary linearly beginning a short distance behind the front nose of the slide mass to the tail end. The pressures at a short distance behind the front nose and at the tail end of the slide mass can be estimated using Equation 3.3;
7. The shear stress along the top and bottom surfaces of the slide mass can be estimated using Equation 3.4;

Incorporating the above conclusions about hydrodynamic stresses, the block model also adjusts the forces applied on the slide mass by the underlying ground according to the contact condition between the slide mass and underlying ground. Using the block model, the mechanism of hydroplaning has been successfully simulated by analyzing the dynamic response of the slide mass under proper stresses applied by the surrounding fluid and underlying ground. The simulations using the block model have also yielded numerical results that agree well with the experimental data reported by Mohrig, et al and with the field observations reported by Bugge, et al. The block model has successfully predicted the occurrence of hydroplaning and explained the greater run-out distances of submarine slides than those of comparable subaerial slides.

7.3 Suggestions on Future Research

To continue the research reported herein, the block model can be improved by considering the deformation of the slide mass and the influence of the acceleration of the slide mass on hydrodynamic stresses. The dynamic response and deformation of the slide mass can be simulated using the finite element method. The hydrodynamic stresses on the surfaces of the slide mass can be studied by modeling the unsteady flow around the slide mass.

The new numerical model can then be used to simulate subaqueous slides and predict the deformation and movement of the slide mass in time and space based on the initial geometry of the slope when failure occurs, the geomorgraphy of the nearby seafloor, and the mechanical properties of the slide material (including shear strength, stress-deformation properties and unit weight).

Appendix A: Details of Program Nopressure.cpp

In order to examine Harbitz et al.'s solution, the computer program nopressure.cpp was written to solve Equations 2.24 to 2.27 for the block length L, block height H, velocity U and flow rate Q. The program nopressure.cpp was written in the C programming language and compiled by microsoft visual studio.net (2003). The input and output data, flow chart and source code of the program are discussed as follows.

A.1 Input Data

The program nopressure.cpp reads from a file named gld.in. An example input file is shown in Figure A.1. The input data are described line by line in Tables A. 1 and A.2.

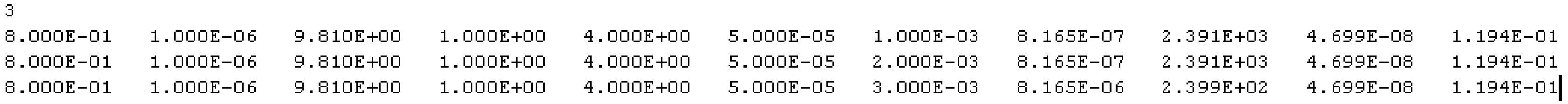

```
3
8.000E-01   1.000E-06   9.810E+00   1.000E+00   4.000E+00   5.000E-05   1.000E-03   8.165E-07   2.391E+03   4.699E-08   1.194E-01
8.000E-01   1.000E-06   9.810E+00   1.000E+00   4.000E+00   5.000E-05   2.000E-03   8.165E-07   2.391E+03   4.699E-08   1.194E-01
8.000E-01   1.000E-06   9.810E+00   1.000E+00   4.000E+00   5.000E-05   3.000E-03   8.165E-06   2.399E+02   4.699E-08   1.194E-01
```

Figure A.1: Example input file gld.in for nopressure.cpp

Table A.1: Input data for line 1 of gld.in

Field	Parameter	Physical Meaning
1	*Numcond*	Number of cases

Table A.2: Input data for line 2 of gld.in

Field	Parameter	Physical Meaning
1	R_s	The effective specific gravity of the sliding block, i.e. $R_s = \frac{\rho_s - \rho_w}{\rho_w}$, where ρ_s is the density of the block, and ρ_w is the density of the surrounding fluid.
2	υ_w	The kinematic viscosity of pure water (m^2/s)
3	g	The acceleration due to gravity (m/s^2)
4	s	The ratio of the viscosity of the fluid between the block and underlying ground to that of pure water, i.e. $s = \frac{\upsilon}{\upsilon_w}$, where υ is the viscosity of the fluid between the block and underlying ground.
5	r	The ratio of the distance between the lower corner of the block and underlying ground at the front h_f to that at the tail h_t, i.e. $r = \frac{h_f}{h_t}$
6	k	The ratio of the distance between the lower corner of the block and underlying ground at the tail h_t to the length of the block L, i.e. $k = \frac{h_t}{L}$
7	ϕ	Slope angle of the underlying ground (degree)
8	H	The initial value for the height of the block (m)
9	L	The initial value for the length of the block (m)
10	Q	The initial value for the flow rate (m^2/s)
11	U	The initial value for the velocity of the block (m/s)

Line 2 is repeated for additional cases.

A.2 Output Information

The program nopressure.cpp writes the numerical results to a file named gld.out. An example of the output file is shown in Figure A.2. The output information is described line by line in Table A.3.

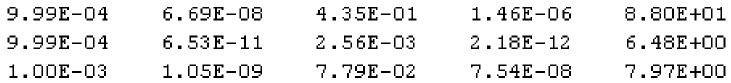

```
9.99E-04    6.69E-08    4.35E-01    1.46E-06    8.80E+01
9.99E-04    6.53E-11    2.56E-03    2.18E-12    6.48E+00
1.00E-03    1.05E-09    7.79E-02    7.54E-08    7.97E+00
```

Figure A.2: Example output file gld.out for nopressure.cpp

Table A.3: Output information for line 1 of gld.out

Field	Parameter	Physical Meaning
1	*error*	The numerical error in the last iteration
2	L	Calculated value for the length of the block (m)
3	H	Calculated value for the height of the block (m)
4	U	Calculated value for the velocity of the block (m/s)
5	Q	Calculated value for the flow rate (m^2/s)

Line 1 is repeated for additional cases.

A.3 Flow Chart

A flow chart for the computer program nopressure.cpp is shown in Figure A.3.

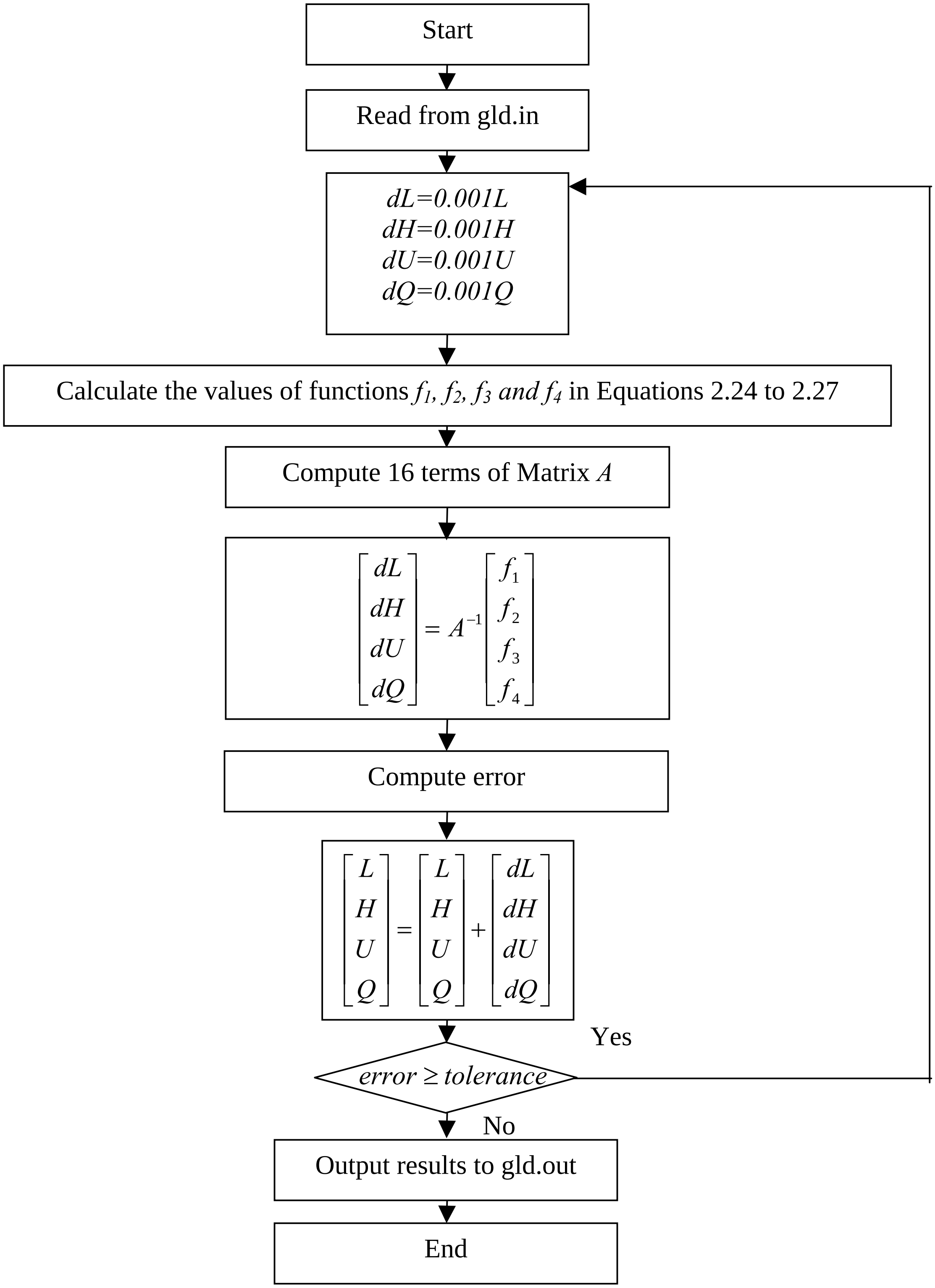

Figure A.3: Flow chart of program nopressure.cpp

A.4 Computer Code

The computer code for program nopressure.cpp is listed as follows.

```
//  solve H L q U

#include <stdio.h>
#include <iomanip.h>
#include <string.h>
#include <iostream.h>
#include <stdlib.h>
#include <malloc.h>
#include <fstream.h>
#include "stdafx.h"
#include "math.h"


// function to calculate the equation value

void eqns(double vari[5],double funs[5],
              double &gama,double &beta,double &Rs,double &nu,double &g,double &s,double &r,double
&k,double &theta)

{
//    calculation parameters
      double hl,ht,alpha,w,kesi;

//    b13(a)
      double b13a1,b13a2,b13a3,b13a4;
      ht=vari[2]*k;
      hl=ht*r;
      alpha=(hl-ht)/vari[2];
      w=alpha*vari[4]*ht/nu;
```

```
      b13a1=(3.0/5*w*(r*r-1)/(r*r))*vari[3]*vari[3];
      b13a2=6*(r*r-1)/(r*r)*vari[3];
      b13a3=-1*w*(0.5+2.0/15*log(r));
      b13a4=-6*(r-1)/r;
//    change function

      funs[1]=(b13a1+b13a2+b13a3)/(-b13a4)-1.0;

//    b25(a)
      double IF1,IF2,IF3,FP;
      IF1=-2.0/15*(r*(log(r)-1)+1);
      IF2=6*(log(r)-r+1);
      IF3=-6*(-1/r+2-r);
      FP=IF1*w+IF2+IF3*vari[3]*(1+0.1*w*vari[3]);
      kesi=nu*vari[4]/alpha/Rs/g/vari[1]/vari[2];
      funs[2]=kesi/(r-1)/k*FP-1;

//    b25(b)
      double IM1,IM2,IM3,MP;
      IM1=-2.0/15*((r*r/2.0-r)*log(r)-r*r/4.0+r-3.0/4.0);
      IM2=6*(-1*log(r)-r*r/2+2*r-3.0/2);
      IM3=-6*(log(r)-r*r/2+r-3.0/2+1/r);
      MP=IM1*w+IM2+IM3*vari[3]*(1+0.1*w*vari[3]);
      funs[3]=kesi/(r-1)/(r-1)/k*MP-0.5;
//    b25(c)
      double Fbd,ReL,Ftd,Pi=3.1415926;
      Fbd=-2.0*log(r)+6*vari[3]*(r-1)/r;
      ReL=s*w/(r-1)/k/k;
      Ftd=w/k*gama*exp(-1*beta*log(ReL));
      // change function
      funs[4]=((kesi*(Fbd+Ftd)))/theta-1.0;
      // add front pressure
//    funs[4]=((kesi*(Fbd+Ftd))+0.0*vari[4]*vari[4]/2.0/Rs/g/vari[2]/1.0)/theta-1.0;
}


//    Create the differential coefficient matrix
```

```
void diff(double dx[5],double A[5][5], double x[5],double &gama, double &beta,double &Rs, double &nu,
double &g, double &s, double &r, double &k, double &theta)
{
      int i,j,t;
      double west[5],east[5], y1[5], y2[5];

      for (j=1;j<=4;j++)
      {
            for (t=1; t<=4; t++)
            {
                  y1[t]=x[t];
                  y2[t]=x[t];

            }
            y1[j]=x[j]+dx[j];
            y2[j]=x[j]-dx[j];

      //    calculate the two function values needed for differential CDS

            eqns(y1, east,gama, beta,Rs, nu, g, s, r, k, theta);
            eqns(y2,west, gama, beta, Rs, nu, g, s,r, k, theta);

            for (i=1;i<=4;i++)
            {
                  A[i][j]=(east[i]-west[i])/2.0/dx[j];
            }


      }

}



//    solve the linear equations
```

```
void solv(double A[5][5],double dx[5],double middle[5])

{
      int i,j,kk,ip1,pivot;
      double big,mult,temp;
      for (i=1; i<4; i++)
      {
            // pivot if needed
            pivot=i;
            big=fabs(A[i][i]);
            for (j=(i+1); j<5; j++)
            {
                  if(fabs(A[j][i])>big)
                  {
                        big=fabs(A[j][i]);
                        pivot=j;
                  }
            }

            if(pivot !=i)
            {
                  for (j=i; j<5; j++)
                  {
                        temp=A[pivot][j];
                        A[pivot][j]=A[i][j];
                        A[i][j]=temp;
                  }
                  temp=middle[pivot];
                  middle[pivot]=middle[i];
                  middle[i]=temp;
            }

//          Gauss Reduction
            ip1=i+1;
            for (j=ip1; j<5; j++)
            {
```

```
                  mult=-A[j][i]/A[i][i];
                  for (kk=1; kk<5; kk++)
                        A[j][kk]=A[j][kk]+mult*A[i][kk];
                  middle[j]=middle[j]+mult*middle[i];

            }

      }

//          Gauss back-substitution
      int jcol,n;
      double sum;

      dx[4]=middle[4]/A[4][4];
      for (i=1; i<4; i++)
      {
            n=5-i-1;
            jcol=n+1;
            sum=0.0;
            for (j=jcol; j<5; j++)
                  sum=sum+A[n][j]*dx[j];
            dx[n]=(middle[n]-sum)/A[n][n];
      }

}

void main()


{
//    4 unknowns H block height(m); L block length (m);q (dimensionless),U; 4 function values at x;
dx;
      double x[5],middle[5],dx[5];

//    knowns:gama and beta in top shear resistance coefficient CF (B21b); Relative desity of buoyant
density (roud/rouw-1); kinematic viscosity of water(m*m/s);
```

```
//    gravity (m/s/s); relative viscosity of debris; ratio of water film thickness head/tail; ratio
of tail thickness over block length; slope angle (deg)
      double gama=0.644,beta=0.5,Rs,nu,g,s,r,k,theta,pi;
      pi=acos(-1.0);
//    null variable
      char names[81],name;
// dx definition and control limit
      double m=0.001, constr=0.01;
      double limit=1e-2;
// read the values of variables

      FILE *stream;
      stream=fopen("gld.in","r");
// output file "gld.out"
      FILE *output;
      output=fopen("gld.out","w");
      fprintf(output,"%s\n","Numcond");

//    null variable
      long i, j;

//  Necessary initialization of variables needed to be input

      Rs=0.1;
      nu=0.1;
      g=0.1;
      s=0.1;
      r=2.0;
      k=0.0001;
      theta=0.1;
      for (i=1; i<=4; i++)
            x[i]=0.1;

//    calculation for different input conditions
int   Numcond, Num;
      fscanf(stream, "%d",&Numcond);
```

```
      for (Num=1; Num<=Numcond; Num++)
      {
      // input


              fscanf(stream,"%lf %lf %lf %lf %lf %lf %lf %lf %lf %lf %lf",
                    &Rs, &nu, &g, &s, &r, &k, &theta,&x[1],&x[2],&x[3],&x[4] );
              theta=theta*pi/180.0;
              for (i=1;i<=4;i++)
                    dx[i]=x[i]*m;



// main loop

double error;
int hu=0;
double A[5][5];

//
              do
          {
                    // calculate eqns

                        eqns(x,middle,gama,beta,Rs,nu,g,s,r,k,theta);

                    //  calculate coefficient matrix

                        diff(dx,A,x,gama, beta,Rs, nu, g, s, r, k, theta);



//    solve the linear equations
                        solv(A,dx,middle);
                        for (i=1; i<=4; i++)
                              dx[i]=-1.0*dx[i];
```

```
//    check dx
//    calculate error

                        error=fabs(dx[1]/x[1]);
                        for (i=2; i<=4; i++)
                              if (error<=fabs(dx[i]/x[i]))
                                    error=fabs(dx[i]/x[i]);


                        if (error>constr)
                        {
                              for (i=1;i<=4;i++)
                              dx[i]=dx[i]/error*constr;
                        }

// output hu,x[i],error

//                      fprintf(output,"%d      %e    %e    %e    %e    %lf\n", hu, x[1], x[2], x[3],
x[4], error);
                        printf("%d  %d    %.8e  %.8e\n", Num,hu,theta/pi*180, error);


//    update x[i]
                        for (i=1; i<=4; i++)
                              x[i]=x[i]+dx[i];

//    constraints on H L q U
                        if (x[1]<=0||x[2]<=0 || x[3]<=0|| x[4]<=0)
                        {
                              fprintf(output,"%s", "unreasonable variables");
                              fprintf(output,"%e      %e    %e    %e    %lf\n", error, x[1], x[2],
x[3], x[4]);
                        }
```

```
//    update dx[i]
                        for (i=1; i<=4; i++)
                              dx[i]=m*x[i];

//    calculate the twelve function values of four equations

                        eqns(x,middle,gama,beta,Rs,nu,g,s,r,k,theta);


//    record the loop

                        hu=hu+1;

              }while (error>=limit && hu<=100000000);

//    calculate Fr, Re, Pressure

double Fr, Reh, Rel, h;

            Fr=x[4]/sqrt(Rs*g*x[1]);
            Reh=0.5*x[4]/nu*(x[2]*k+x[2]*k*r);
            Rel=x[4]*x[2]/nu;
            h=0.5*x[2]*k*(1+r);

            fprintf(output,"%.8e    %.8e  %.8e  %.8e  %.8e\n", error, x[3]*x[4]*k*x[2], x[4], x[1],
x[2]);
//          fprintf(output,"%.8e    %.8e  %.8e  %.8e  %.8e  %.8e  %.8e  %.8e  %.8e  %.8e  %.8e  %.8e
      %.8e\n", r,k,theta/pi*180,x[3],x[4],x[1],x[2], Fr, Re, Cf,Rs,nu,s);

            //  output A matrix
//    fprintf (output, "A matrix \n");
//          for (i=1; i<=4; i++)
//          {

//                for (j=1; j<=4; j++)
//                {
```

```
//                      fprintf(output,"%.8e    ", A[i][j]);
//                }
//
//                fprintf(output, "\n");
//          }

//    output final function values

//    fprintf (output, "final function values\n");
//          fprintf (output, "%.8e  %.8e  %.8e  %.8e\n", middle[1],middle[2],middle[3],middle[4]);

      }
    fclose( stream );

      fclose(output);
}
```

Appendix B: Details of Program Rect.cpp

In order to implement the block model, the program rect.cpp was written in the C programming language and compiled by microsoft visual studio.net (2003). The input and output data, flow chart and source code of the program are discussed as follows.

B.1 Input Data

The program rect.cpp reads from an input file named rect.in. An example input file is shown in Figure B.1. The input data is described line by line in Tables B.1 and B.2.

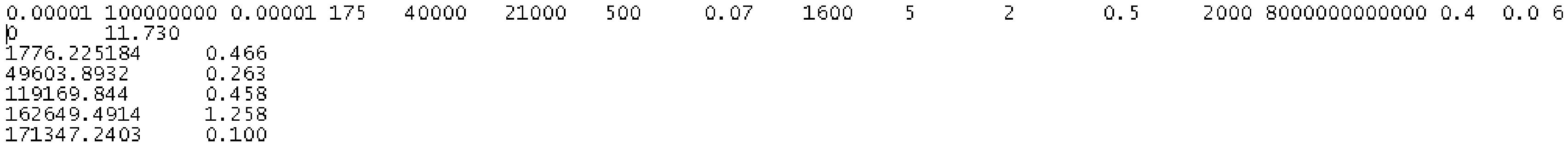

```
0.00001 100000000 0.00001 175   40000   21000   500     0.07    1600    5       2       0.5     2000 8000000000000 0.4  0.0 6
0       11.730
1776.225184     0.466
49603.8932      0.263
119169.844      0.458
162649.4914     1.258
171347.2403     0.100
```

Figure B.1: Example input file rect.in for rect.cpp

Table B.1: Input data for line 1 of rect.in

Field	Parameter	Physical Meaning
1	dt	Time increment for the time integration scheme Δt (second)
2	timelimit	Time limit on the sliding process (second)
3	errorlimit	The allowance of errors when iterative methods are involved
4	H	Height of block H (meter)
5	L	Length of block L (meter)
6	cohesion	The static shear strength of soil at the interface of block and underlying ground τ_y (pa)
7	viscosity	Non-dimensional constant related to the strain rate effect of shear strength μ_s
8	roughness	The height of roughness at the interface of block and underling ground h_r (m)
9	pou	Total density of soil in the block ρ_s ($\mathrm{kg/m^3}$)
10	lamida	The absolute value of the ratio of the lowest pressure along the top surface to the stagnation pressure $\lvert\lambda\rvert$
11	headratio	The ratio of block's height at the leading edge to its average height (This ratio only influences the area where the kinetic pressure along the leading edge is applied.)
12	toppressurerange	The ratio of the length where negative kinetic pressure is applied to the height of the block β
13	totaldensityofground	The total density of soil in the underlying ground ρ_g ($\mathrm{kg/m^3}$)
14	E	The effective young' modulus of soil in the underlying ground (pa)
15	poisson	The effective poisson's ratio of soil in the underlying ground
16	velox	The initial velocity of the block in the x direction $\dot{x}(0)$ (m/s)
17	step	The total number of segments of the underlying ground

Table B.2: Input data for line 2 of rect.in

Field	Parameter	Physical Meaning
1	posi(1)	The x coordinate of the starting position for segment 1 (m)
2	fei(1)	The slope angle of segment 1 of the underlying ground (degree)

Line 2 is repeated for additional segments of underlying ground.

B.2 Output Information

The program rect.cpp writes the numerical results to a file named rect.out. An example of the output file is shown in Figure B.2. The output information is described line by line in Table B.3.

```
0.0E+0    6.7E-1  -5.7E-13   8.9E-14   0.0E+0    0.0E+0    0.0E+0    0.0E+0    8.7E+1  -9.6E-11   -2.1E-2   -2.1E-2
1.0E+0    6.7E-1    5.1E-6   1.4E-12    6.7E-1    2.8E-6   7.7E-13    3.4E-1    8.7E+1  -9.6E-11   -2.1E-2   -2.1E-2
2.0E+0    6.7E-1    7.5E-6   2.0E-12    1.3E+0    9.3E-6   2.5E-12    1.3E+0    8.7E+1  -9.5E-11   -2.1E-2   -2.1E-2
3.0E+0    6.7E-1    8.6E-6   2.3E-12    2.0E+0    1.7E-5   4.7E-12    3.0E+0    8.7E+1  -9.1E-11   -2.1E-2   -2.1E-2
4.0E+0    6.7E-1    9.1E-6   2.5E-12    2.7E+0    2.6E-5   7.1E-12    5.4E+0    8.7E+1  -8.5E-11   -2.1E-2   -2.1E-2
```

Figure B.2: Example output file rect.out for rect.cpp

Table B.3: Output data in line 1 of file rect.out

Field	Parameter	Physical Meaning
1	*time*	Time t (s)
2	*accx0*	The acceleration in the x direction $\ddot{x}$ (m/s^2)
3	*accy0*	The acceleration in the y direction $\ddot{y}$ (m/s^2)
4	*acctheta0*	The angular acceleration in the $x-o-y$ plane $\ddot{\theta}$ (rad/s^2)
5	*velox*	The velocity in the x direction $\dot{x}$ (m/s)
6	*veloy*	The velocity in the y direction $\dot{y}$ (m/s)
7	*velotheta*	The angular velocity in the $x-o-y$ plane $\dot{\theta}$ (rad/s)
8	*x*	The x coordinate of the center of the block (m)
9	*y*	The y coordinate of the center of the block (m)
10	*theta*	The rotation of the block θ
11	*hfront*	The displacement of the lower corner at the front end of the block (m)
12	*htail*	The displacement of the lower corner at the tail end of the block (m)

Line 1 is repeated for additional time for the sliding process of the block.

B.3 Flow Chart

A flow chart for the program rect.cpp is shown in Figure B.3. The subroutine “force” computes all the forces and moments applied on the block. The major variables involved in this subroutine are listed in Table B.3 and the flow chart for the subroutine is shown in Figure B.4.

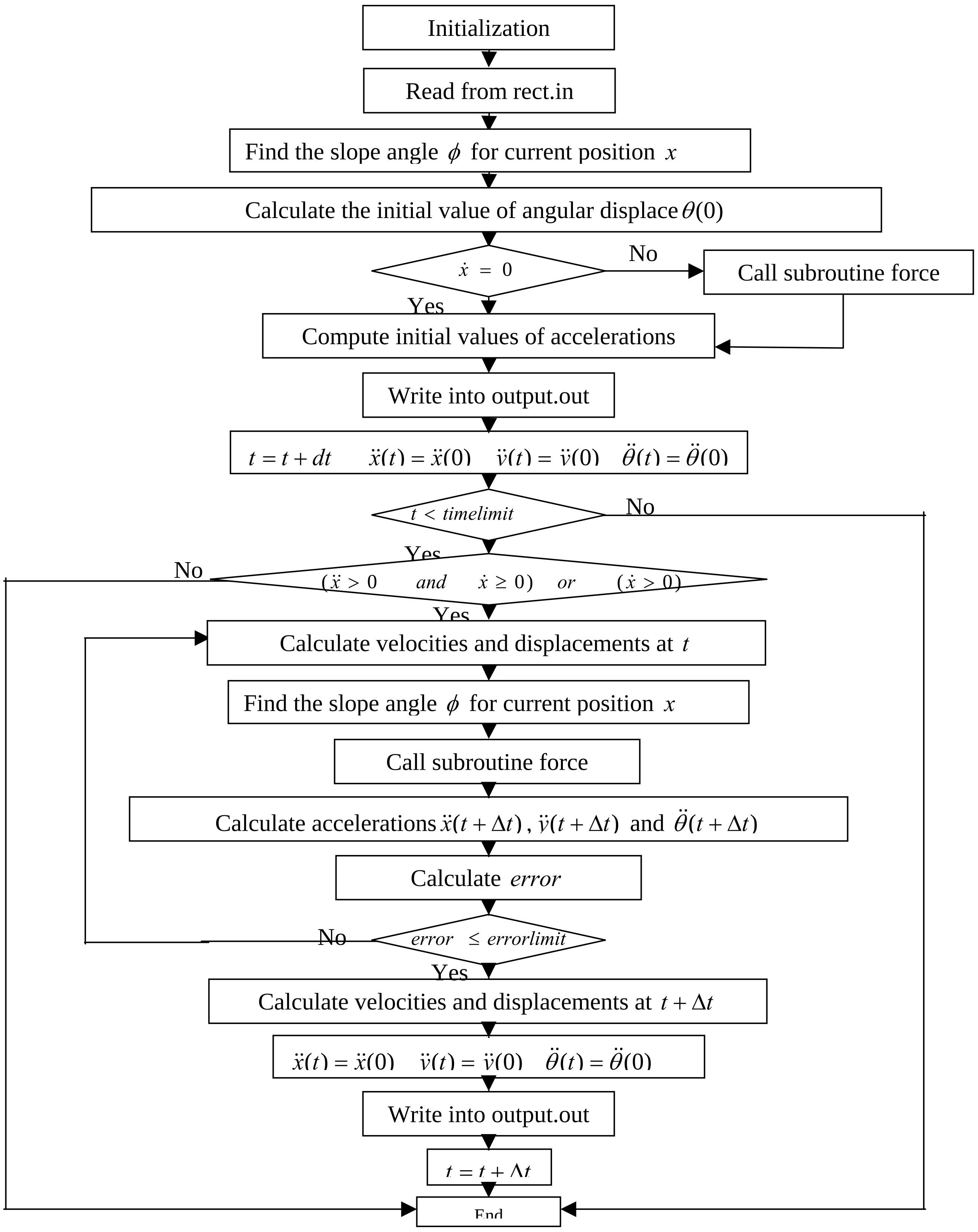

Figure B.3: Flow chart of program rect.cpp

Table B.3: Parameters in subroutine force and their physical meanings

Variable	Physical meaning
cohesion	The static shear strength of soil at the interface of block and underlying ground τ_y (pa)
viscosity	Non-dimensional constant related to the strain rate effect of shear strength μ_s
E	The effective young' modulus of soil in the underlying ground (pa)
poisson	The effective poisson's ratio of soil in the underlying ground
toppressurerange	The ratio of the length where negative kinetic pressure is applied to the height of the block β
totaldensityofground	The total density of soil in the underlying ground ρ_g ($\mathrm{kg/m^3}$)
roughness	The height of roughness at the interface of block and underling ground h_r (m)
pou	Total density of soil in the block ρ_s ($\mathrm{kg/m^3}$)
lamida	The absolute value of the ratio of the lowest pressure along the top surface to the stagnation pressure $\lvert\lambda\rvert$
headratio	The ratio of block's height at the leading edge to its average height (This ratio only influences the area where the kinetic pressure along the leading edge is applied.)
H	Height of block H (meter)
L	Length of block L (meter)
currentfei	The slope angle the underlying ground for current position (rad)
hydroplaning	The variable marks the onset of hydroplaning. This variable is 0 before hydroplaning occurs and 1 after hydroplaning occurs.
velox	The velocity in the x direction $\dot{x}$ (m/s)
veloy	The velocity in the y direction $\dot{y}$ (m/s)
velotheta	The angular velocity in the $x-o-y$ plane $\dot{\theta}$ (rad/s)
x	The x coordinate of the center of the block(m)
y	The y coordinate of the center of the block(m)
theta	The rotation of the block θ
front	The force on the leading edge of the block due to kinetic pressure (N/m)
tail	The force on the trailing edge of the block due to kinetic pressure (N/m)
top	The force on the top surface of the block due to viscous shear (N/m)
bottomf	The force on the bottom surface of the block due to viscous shear (N/m)
bottomp	The force on the bottom surface of the block due to kinetic pressure (N/m)
toppressure	The force on the top surface of the block due to kinetic pressure(N/m)
Nf	The support by underlying ground at the front end (N/m)
Nt	The support by underlying ground at the tail end (N/m)
totalcohesion	The resistance on the block by underlying ground (N/m)
M	The total moment on the block ($N\cdot m/m$)
soildampingfront	The damping force applied by underlying ground at the front end (N/m)
soildampingtail	The damping force applied by underlying ground at the tail end (N/m)
waterdampingforce	The damping force applied by surrounding fluid (N/m)
waterdampingmoment	The damping moment applied by surrounding fluid ($N\cdot m/m$)

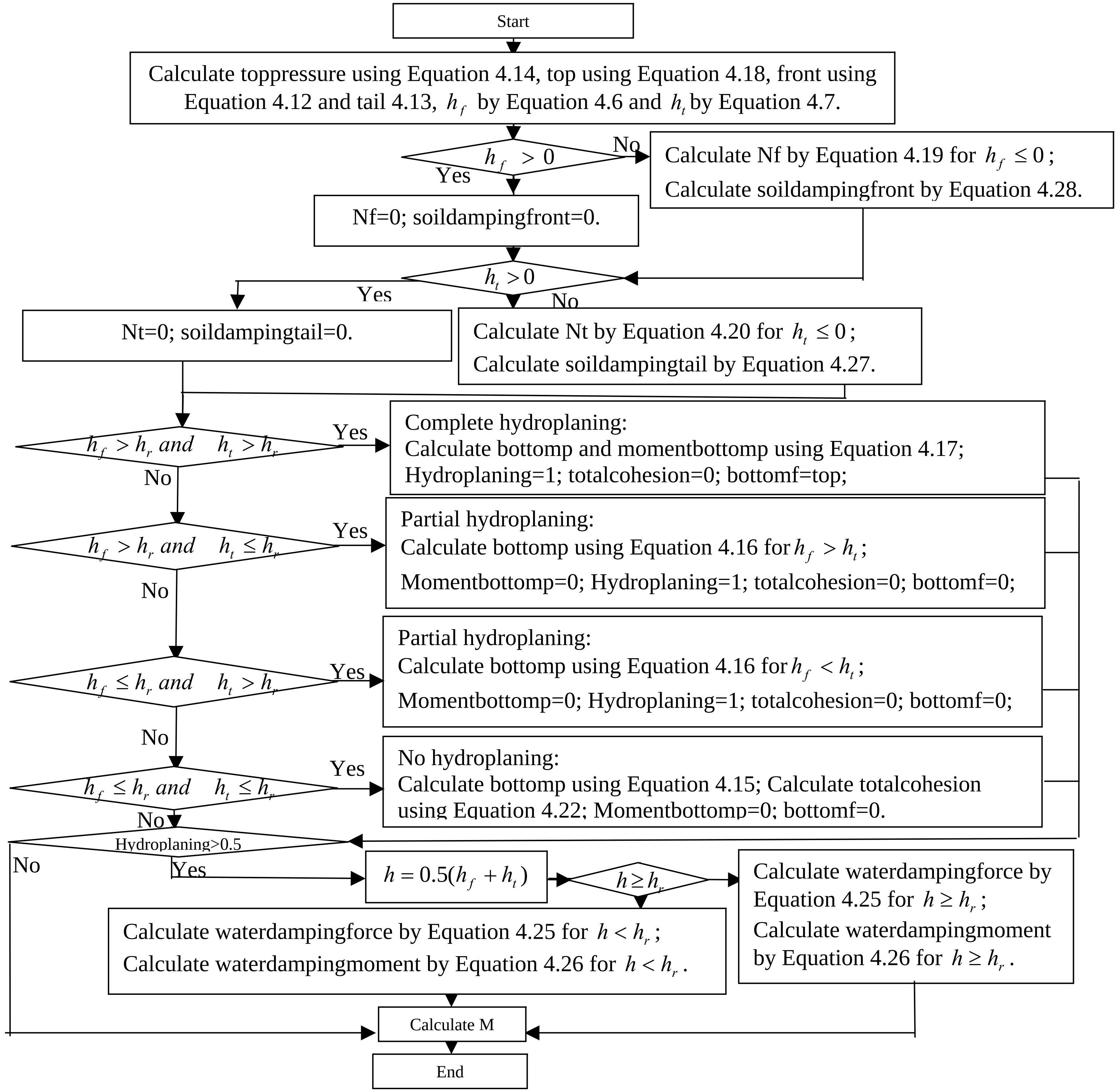

Figure B.4: Flow chart of subroutine force

B.4 Computer Code

The computer code for program rect.cpp is listed as follows.

```
////////////////////////////////////////////////////////////////////////////////
#include <stdio.h>
#include <iomanip.h>
#include <string.h>
#include <iostream.h>
#include <stdlib.h>
#include <malloc.h>
#include <fstream.h>
#include "stdafx.h"
#include "math.h"
//



void force(double cohesion, double viscosity, double E, double poisson,
               double totaldensityofground, double toppressurerange,
               double roughness, double pou, double lamida, double headratio, double H,
               double L, long &hydroplaning, double currentfei,double thetatrial,
               double ytrial, double xtrial, double veloxtrial,double veloytrial,
               double velothetatrial, double &front,double &tail, double &top,
               double &bottomf,double &bottomp,double &toppressure,double &Nf,
               double &Nt,double &totalcohesion, double &M, double &soildampingfront,
               double &soildampingtail, double &waterdampingforce,
               double &waterdampingmoment)
{

      double G, stiffness, effgama;
      double pouwater=1000.0, gravity=9.82;
```

```
      //water density (kg/m^3)
      double u=0.001,h, htail, hfront;
      //water dynamic viscosity(pa.s),gap thickness average, tail, front
      double nu;
      //kinetic viscosity (m^2/s)
      int m,n;
      double ArmNf, ArmNt, ArmFf, ArmFt;
      double Vx=0, momentbottomp=0;
      double      pi=acos(-1.0);

      effgama=(pou-pouwater)*gravity;
      G=E/2.0/(1+poisson);
      stiffness=E/10.0/(1-poisson*poisson);

      front=0;
      tail=0;
      top=0;
      bottomf=0;
      bottomp=0;
      toppressure=0;
      Nf=0;
      Nt=0;
      totalcohesion=0;
      M=0;
      soildampingfront=0;
      soildampingtail=0;
      waterdampingforce=0;
      waterdampingmoment=0;

      Vx=veloxtrial;
//    u=viscosity/10;
//    water viscosity is 10% of that of soil in the block
      nu=u/pouwater;

///   toppressure: linear negative stagnation pressure, from s=0 to
//    s=-H*toppressurerange, lowest=stagnationpressure*lamida
      toppressure=lamida*0.5*pouwater*Vx*Vx*H*0.5*toppressurerange;
```

```
      n=1000;
      top=0.0;
      if (Vx>0)
      {
            for (m=1;m<=n;m++)
            {
                  top=top+L/n*(pouwater/2.0*Vx*Vx*0.027)/(pow((Vx*m*L/n/nu),(1.0/7.0)));
            }

      }

      front=0.5*0.5*pouwater*Vx*Vx*H*headratio;
      //linear from 0 to stagnation, height of head = height H * headratio

      tail=0.5*H*0.5*pouwater*Vx*Vx*0.3;
      //linear from 0 to 0.3 stagnation pressure

      h=ytrial-0.5*H;
      hfront=h+0.5*L*sin(thetatrial);
      htail=h-0.5*L*sin(thetatrial);


//    ground support and soil damping force=-area of contact(L/4)
//    * velocity at contact*((totaldensity of ground * G)^0.5/(1-poisson))

      if (hfront>=0)
      {
            Nf=0;

      }
      else
      {
            Nf=-stiffness*hfront;
            soildampingfront=-pow((totaldensityofground*G),0.5)/(1-poisson)*0.25*L*
                  (veloytrial+velothetatrial*0.5*L*cos(thetatrial));
```

```
      }

      if (htail>=0)
      {
            Nt=0;
      }
      else
      {
            Nt=-stiffness*htail;
            soildampingtail=-pow((totaldensityofground*G),0.5)/(1-poisson)*0.25*L*
                  (veloytrial-velothetatrial*0.5*L*cos(thetatrial));

      }


//    bottom forces

//    complete hydroplaning
      if (hfront>roughness && htail>roughness)
      {
            bottomp=(1.0/2.0*(pouwater*Vx*Vx)*L*0.5*((0.3/(1+0.15*pow((htail/H),0.4)))
                  +(1.0/(1.0+2.57*(pow((hfront/H),0.58))))));
            //linear bottomp
            //calculate the moment due to bottomp only valid when bottom pressure
            //is positive everywhere
            momentbottomp=(1.0/2.0*(pouwater*Vx*Vx)*L*0.5*(-(0.3/(1+0.15*pow((htail/H),0.4)))
            +(1.0/(1.0+2.57*(pow((hfront/H),0.58))))))*L/6.0;

            hydroplaning=1;

            totalcohesion=0;
            bottomf=top;
      }

//    partial hydroplaning
      if (hfront>roughness && htail<=roughness)
      {
```

```
            bottomp=1.0/2.0*(pouwater*Vx*Vx)*L*(1.0/(1.0+2.57*(pow((hfront/H),0.58))));
            //    uniform bottomp
            momentbottomp=0;

            hydroplaning=1;

            totalcohesion=0;
            bottomf=0;
      }
      if (hfront<=roughness && htail>roughness)
      {

            bottomp=1.0/2.0*(pouwater*Vx*Vx)*L*(0.3/(1+0.15*pow((htail/H),0.4)));
            //    uniform bottomp
            momentbottomp=0;

            hydroplaning=1;

            totalcohesion=0;
            bottomf=0;
      }

//    no hydroplaning
      if (hfront<=roughness && htail<=roughness)
      {
            bottomp=1.0/2.0*(pouwater*Vx*Vx)*L;
            //    uniform bottomp
            momentbottomp=0;

            totalcohesion=(cohesion+2*Vx*viscosity/(H))*L;
            bottomf=0;
      }

//    water damping
      if (hydroplaning>0.5)
      {
            if (h>=roughness)
```

```
            {
                  waterdampingforce=-(u/(h*h*h))*veloytrial*(L*L*L);
                  waterdampingmoment=-u/(h*h*h)*velothetatrial*L*L*L*L*L*sin(thetatrial);

            }
            if (h<roughness)
            {
                  waterdampingforce=-(u/(roughness*roughness*roughness))*veloytrial*(L*L*L);
                  waterdampingmoment=-u/(roughness*roughness*roughness)*
                        velothetatrial*L*L*L*L*L*sin(thetatrial);


            }
      }

//    calculate arms of forces
      ArmNf=0.5*L*cos(thetatrial)+0.5*H*sin(thetatrial);
      ArmNt=-0.5*L*cos(thetatrial)+0.5*H*sin(thetatrial);
      ArmFf=0.5*L*sin(thetatrial)-0.5*H*cos(thetatrial);
      ArmFt=-0.5*L*sin(thetatrial)-0.5*H*cos(thetatrial);

      M=waterdampingmoment+toppressure*(0.5*L-H*0.5*toppressurerange)
            +top*0.5*H-front*(0.5*H-H*headratio/3.0)
            +tail/6.0*H+momentbottomp-bottomf*0.5*H+Nf*ArmNf+Nt*ArmNt
            +totalcohesion*0.5*(ArmFf+ArmFt)
            +soildampingfront*ArmNf+soildampingtail*ArmNt;
      //anticlockwise is positive

}

void initialangle(double &thetatrial, double totalcohesion, double L,
                          double stiffness, double y,
                          double H, double &errortrial, double &M)
{
            double Nf, Nt, ArmNf, ArmNt, ArmFf, ArmFt;
            Nf=-stiffness*((y-0.5*H)+0.5*L*sin(thetatrial));
            if (Nf<0)
```

```
            {
                  Nf=0;
                  totalcohesion=0;
            }
            Nt=-stiffness*((y-0.5*H)-0.5*L*sin(thetatrial));
            if (Nt<0)
            {
                  Nt=0;
                  totalcohesion=0;
            }
            ArmNf=0.5*L*cos(thetatrial)+0.5*H*sin(thetatrial);
            ArmNt=-0.5*L*cos(thetatrial)+0.5*H*sin(thetatrial);
            ArmFf=0.5*L*sin(thetatrial)-0.5*H*cos(thetatrial);
            ArmFt=-0.5*L*sin(thetatrial)-0.5*H*cos(thetatrial);
            M=Nf*ArmNf+Nt*ArmNt+totalcohesion*0.5*(ArmFf+ArmFt);
            errortrial=(Nf*ArmNf+Nt*ArmNt
                  +totalcohesion*0.5*(ArmFf+ArmFt))/abs(totalcohesion*0.5*(ArmFf+ArmFt));


}


void main()
// march through time

{
      long i=0,j=0;
//    null variable

      double pi=0,effgama=0,cohesion=0, viscosity=0,pouwater=0.0, gravity=0;
//    effgama effective unit weight (N/mmm), cohesion viscosity
//    between slope bottom and block
//    when contact, water density(kg/m^3), g(m/s^2);
      double pou=0, roughness=0, lamida=0, headratio=0;
//    total density of soil (kg/m^3) in the block, height of roughness,
//    top pressure/stagnation pressure,
//    height of head/average height, only influence front pressure force
```

```
        double toppressurerange=0;
//      length of top pressure/ height of the block


//      null variable for reading input
        char names[81];

//      define variables
        double time=0,timelimit=0,dt=0,x=0,y=0,theta=0, velox=0,veloy=0,velotheta=0;
        double accx0=0,accy0=0,acctheta0=0,accx1=0,accy1=0,acctheta1=0,accx2=0,accy2=0,
              acctheta2=0;
//      time and limit(second), time step (second), coor along slope (m),
//      coor normal to slope (m) and zero at the surface of the slope,
//      initially y is negative so there will be support applied
//      on the block, also output y including it,
//      inclination angle between slope and block (arc),velocities,
//      accelerations at t, t+dt for two trials next to each other;

        double xtrial=0, ytrial=0, thetatrial=0, veloxtrial=0,
              veloytrial=0, velothetatrial=0;
//      positions and velocities within a trial in Newmark scheme

        double errorx=0, errory=0, errortheta=0, error=0, errorlimit=0;
//      errors within a trial and error limit, "error" used only to get initial theta

        double H=0, L=0;
//      block height (m), length(m);

        double fei[10],posi[10],currentfei=0;
//      slope angle (degree), starting position x of an angle;current
//      angle(rad),less than 9 angles
        for (i=1; i<=9; i++)
        {fei[i]=0.0;
         posi[i]=0.0;
        }
```

```
      int step;
//    steps of the slope;

      double thetatrial1=0, thetatrial2=0, thetatrial3=0, errortrial1=0,
            errortrial2=0, errortrial3=0;
//    variables to find initial theta

      long hydroplaning=0;
//    0 never hydroplaned, 1 hydroplaning has happened

      double      E=0, poisson=0, totaldensityofground=0, G=0, stiffness=0;
//  Young's modulus, poisson' ratio, density, shear modulus of ground soil,
//    stiffness of the ground springs

      double front=0, tail=0,top=0, bottomf=0,bottomp=0,toppressure=0,M=0;
//    total front and tail forces due to kinetic pressure,top force due to
//    kinetic resistance and bottom force due to kinetic resistance
      // total bottom force due to kinetic bottom pressure
      // total top force due to kinetic pressure
      //totoal moment
      double totalcohesion=0,Nf=0, Nt=0;
      //resistance by ground parallel to ground surface, ground support
      //at front corner, tail corner, normal to ground surface
      double soildampingfront=0.0, soildampingtail=0.0;
      //damping force due to 1)energy dissipation in ground soil 2)
      //squeeze film lubrication, normal to ground surface
      double waterdampingforce=0, waterdampingmoment=0;
      //water damping force and moment, normal to ground surface, anticlock

      //    finish define variables

//    define files
      int numflushed;
//    input
      FILE *stream;
      stream=fopen("rect.in","r");
//  output file "rect.out"
```

```
      FILE *output, *output1;
      output=fopen("rect.out","w");
      output1=fopen("output1.out","w");
//    finish define files

//    read from rect.in
      fscanf(stream, "%lf %lf %lf %lf %lf %lf %lf     %lf   %lf   %lf   %lf   %lf
                  %lf %lf %lf %lf %d",&dt, &timelimit, &errorlimit, &H, &L,
                  &cohesion, &viscosity,&roughness, &pou, &lamida,
                  &headratio, &toppressurerange, &totaldensityofground,
                  &E, &poisson,&velox, &step);
      for (i=1; i<=step; i++)
            fscanf(stream, "%lf %lf", &posi[i], &fei[i]);
//    finish reading

      G=E/2.0/(1+poisson);
      stiffness=E/10.0/(1-poisson*poisson);
//    stiffness coming from settlement of strip footing at the center and surface
//    of ground surface, stiffness=modulus of soil/(1-poisson's ratio^2)/10
//    where 10 is related to L/B for rectangular footing and use L/B = 10e7,
//    possion's ratio=0.4 modulus = 8000kpa

      pi=acos(-1.0);
      pouwater=1000.0;
      gravity=9.82;

      effgama=(pou-pouwater)*gravity;
      currentfei=pi*fei[1]/180.0;
      totalcohesion=(cohesion+2*velox*viscosity/H)*L;

      // initial y and theta should be solved together
      // the following is not perfect
      //    calculate initial y and theta to maintain initial equilibrium
      //in y and theta direction
      y=0.5*H-effgama*H*L*cos(currentfei)/2.0/stiffness;

      //plot error vs thetatrial
```

```
//    for experiments, -0.00001 for real slides, -0.0000001,depends on L/H
      thetatrial1=-0.00001;
      thetatrial1=-0.00000001;
      while (thetatrial1<=0.0)
      {
            initialangle(thetatrial1, totalcohesion, L, stiffness, y, H, errortrial1,M);
            thetatrial1=thetatrial1+1.0e-10;
            fprintf(output1, "%E    %E\n", thetatrial1, errortrial1);
            numflushed = _flushall();
      }
      //find right initial theta
      thetatrial1=-0.0000001;
      initialangle(thetatrial1, totalcohesion, L, stiffness, y, H, errortrial1,M);
      if(errortrial1<=0)
            printf("%s\n", "errortrial1<=0");
      error=errortrial1;
      thetatrial2=0.0;
      initialangle(thetatrial2, totalcohesion, L, stiffness, y, H, errortrial2,M);
      if(errortrial2>=0)
            printf("%s\n", "errortrial2>=0");
      if(abs(error)>abs(errortrial2))
            error=errortrial2;

      while (abs(error)>=(errorlimit))
      {
            printf("%e  %e    %e\n", thetatrial1, thetatrial2, error);
            thetatrial3=0.5*(thetatrial1+thetatrial2);
            initialangle(thetatrial3, totalcohesion, L, stiffness, y, H, errortrial3,M);
            if (errortrial3>=0)
                  thetatrial1=thetatrial3;
            else
                  thetatrial2=thetatrial3;
            if (abs(error)>abs(errortrial3))
            {
                  theta=thetatrial3;
                  error=errortrial3;
            }
```

```
      }

      ////////////////////////////////////////////////////////
            if (velox<=0)
            {
//          //check initial Nf and Nt
            Nf=-stiffness*((y-0.5*H)+0.5*L*sin(theta));
            Nt=-stiffness*((y-0.5*H)-0.5*L*sin(theta));
            if(Nf<=0)
                  printf("%s\n", "Nf smaller than 0");
            if(Nt<=0)
                  printf("%s\n", "Nt smaller than 0");

            accx0=(effgama*sin(currentfei)*H*L-totalcohesion)/(pou*H*L);
            if (accx0<0)
                  fprintf(output1,"%s\n", "going up the slope at t=0");

            //calculate initial accy and acctheta
            accy0=(Nf+Nt-effgama*H*L*cos(currentfei))/(pou*H*L);
            acctheta0=M/((pou*H*L/12.0)*(L*L+H*H));

            }
            else
            {
                  force(cohesion, viscosity, E, poisson,totaldensityofground,
                        toppressurerange,roughness, pou, lamida,
                        headratio,H,L,hydroplaning, currentfei,theta,y,x,
                        velox,veloy, velotheta,front,tail,top,bottomf,
                        bottomp,toppressure,Nf,Nt,totalcohesion,M, soildampingfront,
                        soildampingtail, waterdampingforce, waterdampingmoment);
                        //calculate acceleration
                  accx0=(effgama*H*L*sin(currentfei)-totalcohesion-(front-tail)*cos(theta)
                        -top*cos(theta)-bottomf*cos(theta)
                        -bottomp*sin(theta)-toppressure*sin(theta))/(pou)/H/L;
                  accy0=(waterdampingforce+Nf+Nt+soildampingfront+soildampingtail
                        +bottomp*cos(theta)+toppressure*cos(theta)
                        -(front-tail)*sin(theta)-top*sin(theta)-bottomf*sin(theta)
```

```
                        -effgama*H*L*cos(currentfei))/(pou)/H/L;
                  acctheta0=(M)/((pou*H*L/12.0)*(L*L+H*H));

            }

//    //    output initial condition
      fprintf(output,"%E      %E    %E    %E    %E    %E    %E    %E    %E    %E    %E    %E    ",
            time, accx0, accy0, acctheta0,velox,veloy,
            velotheta,x,y,theta,(y-0.5*H+0.5*L*sin(theta)), (y-0.5*H-0.5*L*sin(theta)) );
      numflushed = _flushall();


//   NO hydroplaning
      accy0=0;
      acctheta0=0;
//    No hydroplaning

      time=dt;
      accx1=accx0;
      accy1=accy0;
      acctheta1=acctheta0;

      // main loop
      while (time<=timelimit)
      {
            if ((accx0>0.0 && velox>=0 && theta<=pi/2.0 && theta>=-pi/2.0)||
                  (velox>0.0 && theta<=pi/2.0 && theta>=-pi/2.0))
            {
                  do
                  {

                        //calculate trial velocities
                        veloxtrial=velox+dt*(accx0+accx1)*0.5;
                        veloytrial=veloy+dt*(accy0+accy1)*0.5;
                        velothetatrial=velotheta+dt*(acctheta0+acctheta1)*0.5;

                        //calculate trial position
```

```
                        xtrial=x+velox*dt+0.5*(0.5*(accx0+accx1))*dt*dt;
                        ytrial=y+veloy*dt+0.5*(0.5*(accy0+accy1))*dt*dt;
                        thetatrial=theta+velotheta*dt+0.5*(0.5*(acctheta0+acctheta1))*dt*dt;


                        //find current fei
                        for (i=1;i<=step;i++)
                        {
                              if (xtrial>=posi[i])
                              {
                                    currentfei=pi*fei[i]/180.0;
                              }
                        }

                        //calculate forces
                        force(cohesion, viscosity, E, poisson,totaldensityofground,
                              toppressurerange,roughness, pou, lamida,
                              headratio,H, L, hydroplaning, currentfei,thetatrial,
                              ytrial,xtrial, veloxtrial,veloytrial,
                              velothetatrial,   front,tail,top,bottomf,bottomp,toppressure,
                              Nf,Nt,totalcohesion,M,
                              soildampingfront, soildampingtail, waterdampingforce,
                              waterdampingmoment);

                        //calculate acceleration
                        accx2=(effgama*H*L*sin(currentfei)-totalcohesion
                              -(front-tail)*cos(thetatrial)-top*cos(thetatrial)
                              -bottomf*cos(thetatrial)-bottomp*sin(thetatrial)
                              -toppressure*sin(thetatrial))/(pou)/H/L;
                        accy2=(waterdampingforce+Nf+Nt+soildampingfront+soildampingtail
                              +bottomp*cos(thetatrial)+toppressure*cos(thetatrial)
                              -(front-tail)*sin(thetatrial)-top*sin(thetatrial)
                              -bottomf*sin(thetatrial)-effgama*H*L*cos(currentfei))/(pou)/H/L;
                        acctheta2=(M)/((pou*H*L/12.0)*(L*L+H*H));

//    No hydroplaning
                        accy2=0;
```

```
                        acctheta2=0;
//    No hydroplaning
                        if(accx1==0 && accx2==0)
                        {
                              errorx=0;
                        }
                        else
                        {
                              if ((accx1+accx2)==0)
                              {
                                    errorx=2.0;
                              }
                              else
                              {
                                    errorx=abs(accx2-accx1)/(0.5*abs(accx2+accx1));

                              }

                        }

                        if(accy1==0 && accy2==0)
                        {
                              errory=0;
                        }
                        else
                        {
                              if ((accy1+accy2)==0)
                              {
                                    errory=2.0;
                              }
                              else
                              {
                                    errory=abs(accy2-accy1)/(0.5*abs(accy2+accy1));

                              }

                        }
```

```
        if(acctheta1==0 && acctheta2==0)
        {
              errortheta=0;
        }
        else
        {
              if ((acctheta1+acctheta2)==0)
              {
                    errortheta=2.0;
              }
              else
              {
                    errortheta=abs(acctheta2-acctheta1)
                          /(0.5*abs(acctheta2+acctheta1));

              }

        }


        //update trial accelerations
        accx1=accx2;
        accy1=accy2;
        acctheta1=acctheta2;

        //output to screen
        printf("%E  \n",time);
        printf("    %E    %E    \n    %E    %E    %d\n", xtrial, veloxtrial,
              (ytrial-0.5*H-0.5*L*sin(thetatrial)),
              thetatrial, hydroplaning);

  }
  while (((abs(accx1-accx2)>1.0e-11) & (errorx > errorlimit))
        || ((abs(accy1-accy2)>1.0e-11)&
        (errory > errorlimit)) || ((abs(acctheta1-acctheta2)>1.0e-11)
        & (errortheta > errorlimit)));
```

```
                //    update
                x=x+velox*dt+0.5*(0.5*(accx0+accx2))*dt*dt;
                y=y+veloy*dt+0.5*(0.5*(accy0+accy2))*dt*dt;
                theta=theta+velotheta*dt+0.5*(0.5*(acctheta0+acctheta2))*dt*dt;
                velox=velox+dt*0.5*(accx0+accx2);
                veloy=veloy+dt*0.5*(accy0+accy2);
                velotheta=velotheta+dt*0.5*(acctheta0+acctheta2);
                accx0=accx2;
                accy0=accy2;
                acctheta0=acctheta2;


            }
            else
            {
                fprintf(output1,"%s\n","moving to -x direction or theta is not reasonable");
                fprintf(output1,"%lf    %E    %E    %E    %E    %E    %E    %E    %E    %E    %E
        %E    ",
                    time, accx0, accy0, acctheta0,velox,veloy,velotheta,x,y,theta,
                    (y-0.5*H+0.5*L*sin(theta)), (y-0.5*H-0.5*L*sin(theta)));
//              fprintf(output1,"%E     %E    %E    %E    %E    %E    %E    %E    %E    %E    %E
        %E    %E    %E\n",
//              front,tail,top, bottomf, bottomp,
//              toppressure,Nf,Nt,totalcohesion,M,soildampingfront,soildampingtail,
//              waterdampingforce, waterdampingmoment);
                time=timelimit+dt;
                numflushed = _flushall();

            }
            //output
            if((floor(1*time)>(1*(time-dt)))&& (time<=timelimit))
                {
                    //printf("%lf     %E    %E    %E    \n",time,   accx1,      accy1,
        acctheta1);
                    //fprintf(output,"%lf   %E    %E    %E    %E    %E    %E    %E    %E
        %E\n",
```

```
                        //time,     accx0, accy0, acctheta0,
                        //velox,veloy,velotheta,x,y,theta/pi*180.0);
                        fprintf(output,"%E      %E     %E     %E     %E     %E     %E     %E     %E     %E
      %E     %E     ",
                              time, accx0, accy0, acctheta0,
                              velox,veloy,velotheta,x,y,theta,(y-0.5*H+0.5*L*sin(theta)),
                              (y-0.5*H-0.5*L*sin(theta)));

                        numflushed = _flushall();

                  }

            time=time+dt;
      }

//    fprintf(output,"%s\n","reach time limit");
    fclose( stream );
      fclose( output );
}
```

References

Blight, G. E. (1997). "Destructive Mudflows as a Consequence of Tailings Dyke Failures". Proceedings Institution of Civil Engineers, Geotechnical Engineering. Vol. 125, pp. 9-18.

Blight, G. E. and Fourie, A. B. (2005). "Catastrophe Revisited – Disastrous Flow Failures of Mine and Municipal Solid Waste". Geotechnical and Geological Engineering. Vol 23, pp 219-248.

Bondevik, S., Svendsen, J. I., Johnsen, G., Mangerud, J., and Kaland, P. E. (1997). The Storegga tsunami along the Norwegian coast, its age and runup. Boreas, Vol. 26, pp. 29 – 53.

Browne, A. L. and Whicker, D. (1983). An Interactive Tire-Fluid Model for Dynamic Hydroplaning. Frictional Interaction of Tire and Pavement. ASTM STP 793.

Bugge, T., Belderson, R. H., and Kenyon. N. H. (1988). "The Storegga Slide". Philosophical Transactions of the Royal Society of London. Series A, Mathematical and Physical Sciences. Vol. 325, No. 1586. pp. 357-388.

Crowe, C. T., Roberson, J. A.,and Elger, D. F. (2000). Engineering Fluid Mechanics. John Wiley and Sons, Inc. New York.

Dafalias, Y. F. (1986). "Bounding Surface Plasticity I: Mathematical Foundation and Hypoplasticity." Journal of Engineering Mechanics. ASCE. Vol. 112, No. 9, pp. 966-987.

Dafalias, Y. F. and Hermann, L. R. (1982). Bounding Surface Formulation in Soil Plasticity, Chapter 10 in Soil Mechanics – Transient and Cyclic Loads. Edited by G.N. Pande and O.C. Zienkiewicz. John Wiley & Sons Ltd. New York.

Dafalias, Y. F. and Hermann, L. R. (1986). "Bounding Surface Plasticity II: Application to Isotropic Cohesive Soils." Journal of Engineering Mechanics. ASCE. Vol. 112, No. 12, pp. 1236-1291.

Dawson, A. G., Long, D., and Smith, D. E. (1988). The Storegga slides: Evidence from eastern Scotland for a possible tsunami. Marine Geology, Vol. 82, pp. 271 – 276.

De Blasio, F. V., Engvik, L., Harbitz, C. B. and Elverhøi, A., (2004),"Hydroplaning and submarine debris flows," Journal of geophysical research, Vol. 109, C01002, doi: 10.1029/2002JC001714.

Dobry, R. and Alvares, L. (1967). Seismic Failures in Chilean Tailings Dams. Journal of Soil Mechanics and Foundation Engineering. Div. ASCE. Vol. 93, SM6, pp. 237-260.

Egolf, P.W. and Weiss, D. A. (1995). "Model for Plane Turbulent Couette Flow." Physical Review Letters. 75. pp2956-2959.

Evans, D., King, E. L., Kenyon, N. H., Brett, C., and Wallis, D. (1996). Evidence for long-term instability in the Storegga Slide region off western Norway. Marine Geology, Vol. 130,p p. 281-292.

Ewart, W. D. (1962). Hydroplanes and Hovercraft. Frederick Muller Limited. London.

Ferziger, J. H., Peric, M. (2002). Computational Methods for Fluid Dynamics. Springer-Verlag Berlin Heidelberg, New York.

Fluent 6.2 User's Guide. (2005). Fluent Inc.

Fourie, A. B., Blight, G. E. and Papageorgiou, G. (2001). Static Liquefaction as a Possible Explanation for the Merriespruit Tailings Dam Failure. Canadian Geotechnical Journal. Vol. 38, pp. 707-719.

Fread, D.L. (1984). "A breach erosion model for earthen dams". Proceedings of the Speciality. Conference on Delineation of Landslide, Flash Flood, and Debris Flow Hazards in Utah. Utah State University, Logan, Utah, 30 pp.

Gambit 2.2 Modeling Guide. (2004). Fluent Inc.

Hampton M. A. (1972). The Role of Subaqueous Debris Flows in Generating Tvubidity Currents. Journal of Sedimentary Petrology. Vol. 42, pp. 775-793.

Hampton, M. A. and Locat, J. (1996). Submarine Landslides. Reviews of Geophysics. Vol. 34, pp.33-59.

Hance, J. J., (2002), Development of a database and assessment of seafloor slope stability based on published literature, M.S. thesis, the university of Texas at Austin.

Harbitz, C.B., Parker, G., ElverhΦi, A., Marr, J.G., Mohrig, D., and Harff, P.A (2003). "Hydroplaning of subaqueous debris flows and glide blocks: Analytical solutions and discussion," J. Geophys. Res., 108(B7), 2349, doi:10. 1029/2001 JB001454.

Harrin, E. N. (1958). Low Tire Friction and Cornering Forces on a Wet Surface. NACA TN 4406.

Heim, A. (1882). Der Bergsturz von Elm: Zeitschrift der deutschen geologischen Gesellschaft. Vol 34. pp 74-115.

Horne, W. B. and Dreher, R. C. (1963). Phenomena of Pneumatic Tire Hydroplaning. NASA TN D-2056.

Hsü, K. J. (1975). Catastrophic Devris Streams (Sturdy Storms) Generated by Rockfalls. Geological Society of America Bulletin. Vol. 86, pp. 129-140.

Hutchinson, J.N. 1986. A sliding-consolidation model for flow slides. Canadian Geotechnical Journal, 23: 115–126.

Imran, J, and Parker, G (2001). "A Numerical Model of Muddy Subaqueous and Subaerial Debris Flows," Journal of hydrodynamic engineering, Vol 127, Issue 11, pp. 959-968.

Iverson, R. M. and LaHusen, R. G. (1993). Friction in Debris Flows: Inferences from Large-scale Flume Experiments. In Shen, H. W., Su, S. T. and Wen F., eds. Hydraulic Engineering 1993. Proceedings of the 1993 Conference: New York. ASCE. pp. 1604-1609.

Johnson, A. M. (1970). Physical Processes in Geology; A Method for Interpretation of Natural Phenomena; Intrusions in Igneous Rocks, Fractures, and Folds, Flow of Debris and Ice. San Fransisco, California, Freeman, Cooper and Co., p. 577.

Kaliakin, V. N. and Hermann, L. R. (1991). Guidelines for Implementing the Elastoplastic-viscoplastic Bounding Surface Model. Technical Report, Department of Civil Engineering, University of California, Davis.

Kokusho, T., Watanabe, K. and Sawano, T. (1998). Effect of Water Film on Lateral Flow Failure of Liquefied Sand. Proceedings of the 11th European Conference on Earthquake Engineering, A. A. Balkema, Rotterdam, The Netherlands, pp. 1-8.

Körner HJ (1976) Reichweite und Geschwindigkeit von Bergsturzen und Fleisschneelawinen. Rock Mech 8:225–256.

Laval, A., Cremer, M., Beghin, P. and Ravenne, C. (1988). Density Surges: Two-dimensional Experiments. Sedimentology. (1988) Vol. 35, pp 73-84.

Long, D., and Holmes, R. (2001). Submarine landslides and tsunami threat to Scotland. ITS 2001 Proceedings, Session 1, Number 1-12,p p. 355-365.

Major, J. J. and Pierson, T. C. (1992). Debris Flow Rheology: Experimental Analysis of Fine-grained Slurries. Water Resources Research. Vol. 28, pp. 841-857.

Maniar, D. R. (2004). A Computational Procedure for Simulation of Suction Caisson Behavior under Axial and Inclined Loads. PhD dissertation. The University of Texas at Austin.

Marr, JG, Harff, PA, Shanmugam, G. and Parker, G (2001). "Experiments on Subaqueous Sandy Gravity Flows: The Role of Clay and Water Content in Flow Dynamics and Depositional Structures," Geological Society of America Bulletin, Vol 113, No. 11, pp1377-1386.

Miao, T., Liu, Z. and Niu, Y. (2001). A Sliding Block Model for Run-out Prediction of High-speed Landslides. Canadian Geotechnical Journal. Vol. 38 (2), pp. 217-226.

Mohrig, D., Ehipple, K. X., Hondzo, M. Ellis, C. and Parker, G (1998). Hydroplaning of subaqueous debris flows, Geol. Soc. Am.Bull., 110, pp 387-394.

Mohrig, D, Elverhøi, A and Parker, G (1999). "Experiments on the Relative Mobility of Muddy Subaqueous and Subaerial Debris Flows, and Their Capacity to Remobilize Antecedent Deposits," Marine Geology, Vol 154, pp 117-129.

Moriwaki, H., inokuchi, T., Hattanji, T., Sassa, K., Ochiai, H. and Wang, G. (2004). Failure Processes in a Full-scale Landslide Experiment Using a Rainfall Simulator. Landslides. Vol. 1, pp. 277-288.

Moriwaki, H., Yazaki, S. and Oyagi, N (1985). A gigantic debris avalanche and its dynamics at Mount Ontake caused by the Naganoken-seibu earthquake, 1984. Proc. 4th Int. Conf. Field Workshop on Landslides, Tokyo, pp. 359-364.

Newman, JN (1977). Marine Hydrodynamics, MIT Press, Cambridge, Mass.

Newmark,N.M. (1959) "A method for computation of structural dynamics", Proc. American Society of Civil Engineers, 85. EM3. pp. 67-94.

Panton, R. L. (1984). Incompressible Flow. John Wiley and Sons, Inc. New York.

Perla R, Cheng TT, McClung D (1980) A two-parameter model of snow-avalanche motion. J Glaciol 26(94):197–207.

Schlichting, H (1979). Boundary-layer theory, 7th ed. McGraw-Hill, New York, pp 598-641.

Shreve, R. L. (1968a). The Blackhawk landslide: Geological Society of America Special Paper 108.

Shreve, R. L. (1968b). Leakage and Fluidization in air-layer lubricated avalanches: Geological Society of America Bulletin. Vol. 79, pp 653-658.

Tacher, L. , Bonnard, C., Laloui, L. and Parriaux, A. (2005). "Modeling the behavior of a large landslide with respect to hydrogeological and geomechanical parameter heterogeneity". Landslides. 2:3-14.

Tzabaris, G. (2000). Calculation of Complex Turbulent Flows. Southampton, Boston, WIT.

Terzaghi, K. (1950). Mechanism of landslides. Application of Geology to Engineering Practice (Berkey volume). New York. Geol. Soc. America. Pp. 83-123.

Voight, B. and Sousa, J. (1994). Lessons from Ontake-san: A comparative analysis of debris avalanche dynamics. Engineering Geology. Vol 38. pp 261-297.

Wagener, F. (1997). The Merriespruit Slimes Dam Failure: Overview and Lessons Learned. Journal of the South African Institution of Civil Engineering. Vol. 39(3), pp. 11-15.

Vita

Hongrui Hu was born in Tianjin, China on September 2nd 1977. She is the second child born to Zhongying Guo and Zhiming Hu. Hongrui graduated from Nankai High School, Tianjin in 1996. She received her Bachelor's and Master's degrees in 2000 and 2002 respectively, from the Department of Hydraulic Engineering at Tsinghua University, Beijing, China. From August 2002 to August 2003, Hongrui studied at the Department of Civil Engineering at Texas A&M University. In August 2003, she enrolled at the University of Texas at Austin to pursue a PhD in Civil Engineering.

Permanent address: Dagang, Gangmingli, 2-103, Tianjin, China, 300276

This dissertation was typed by Hongrui Hu.